UNIVERSITY OF OKLAHOMA

GRADUATE COLLEGE

LIGHT MATTER INTERACTION

IN

A RYDBERG BLOCKADED ENSEMBLE

A DISSERTATION

SUBMITTED TO THE GRADUATE FACULTY

in partial fullfillment of the requirements for the

Degree of

DOCTOR OF PHILOSOPHY

By

AKBAR JAHANGIRI JOZANI
Norman, Oklahoma
2022

LIGHT MATTER INTERACTION
IN
A RYDBERG BLOCKADED ENSEMBLE

A DISSERTATION APPROVED FOR THE
HOMER L. DODGE DEPARTMENT OF PHYSICS AND ASTRONOMY

BY THE COMMITTEE CONSISTING OF

Dr. James P. Shaffer, Chair

Dr. Alberto Marino

Dr. Arne Schwettmann

Dr. Bruno Uchoa

Dr. Jessica Ruyle

© Copyright AKBAR JAHANGIRI JOZANI 2022
All Rights Reserved.

To the memory of my father

Table of Contents

List of Tables **vi**

List of Figures **xiv**

Abstract **xv**

1 Introduction **1**

2 Theoretical Background **16**
2.1 Properties of Rydberg atoms 16
2.1.1 Energies of the Rydberg state 16
2.1.2 Wavefunctions 20
2.2 Rydberg pair interactions 23
2.2.1 Stark effect 25
2.2.2 Potential curve calculation 27
2.3 Atom light interaction 29
2.3.1 Two-level atom in laser field 29
2.3.2 Three-level atom in a laser field 33
2.3.3 Density matrix 35
2.3.4 Adiabatic elimination of the intermediate state 38
2.4 N two-level atom system 40

3 Pair potential calculations **43**
3.1 Introduction 43
3.1.1 1D blockade experiment 45
3.1.2 Classical hard sphere model 47
3.1.3 Theory work 51

4 Many body Rydberg interaction **65**
4.1 Rydberg blockade, super atom and collective effect 66
4.1.1 Blockade and hard sphere model 67
4.2 Complex susceptibility 72
4.3 Pair correlation function, $g^{(2)}(\mathbf{R})$ 79
4.4 Rydberg excitation statistics, Mandel Q parameter 84
4.5 Phase transition in interacting Rydberg ensembles 89
4.5.1 First and continuous phase transition 90
4.5.2 Classical and quantum phase transitions 91
4.5.3 Phase transition and universality in interacting Rydberg systems 92
4.6 Off-resonant excitation 104

5 Cavity-QED calculations **118**
5.1 Cavity-QED 118
5.2 Experimental setup 124
5.2.1 Absorbates on mirrors and electric field 127

6 Conclusion and future direction **134**

References **139**

List of Tables

2.1 Quantum defect parameters δ_0 and δ_2, used in this thesis for Rb. The effective principal quantum number n^*, for Rb in the $50S_{1/2}$ states is $n^* = 46.8687$. For higher angular momentum states $l > 3$, the quantum defect is acceptably negligible. 20
2.2 Constants used for calculating the Rydberg atom wavefunctions. . . . 23

List of Figures

1.1 Energy level diagram of a Rubidium atom. 2

1.2 Energy level diagram of interacting Rydberg pairs $|rr\rangle$. This diagram shows the mechanism for the formation of the blockade volume. When the atoms are far away, the interaction between them is minimal, and both atoms can be excited to the Rydberg state simultaneously. However, as they get closer to each other, the energy required to excite the second atom goes out of the reach of the laser linewidth, and the blockade volume around them is formed. In the blockade volume, only one atom can be excited to the Rydberg state $|r\rangle$. 7

1.3 Excitation of an ensemble of two-level atoms. (a) Shows an ensemble of N non-interacting atoms. Ω is the coupling strength. All atoms can be excited simultaneously to the Rydberg state. (b) Shows an ensemble of N interacting atoms in a blockaded volume in which only one excitation is possible and atoms are collectively excited to the Rydberg state with $|r\rangle = \frac{1}{\sqrt{N}} \sum_i |g_1 + g_2 + ... + r_i + g_{N-1}, g_N\rangle$. The collective Rabi frequency excites atoms to the Rydberg state $\sqrt{N}$ faster than the non-interacting system. 8

1.4 Rydberg atomic ensemble. The blue spheres are the ground-state atoms. The red spheres are the Rydberg atoms, and the volume around them, indicated with green color, is the blockade volume. In each blockaded volume, only one Rydberg atom can exist. 9

2.1 Size of a typical Rydberg atom in comparison to a Hydrogen atom. . . 17

2.2 Excitation of the second Rydberg atom is blockaded due to the interaction between atoms. 17

2.3 Radial wavefunctions of Rb Rydberg atoms generated using the RADIAL program [91]. The blue line is the l-dependent potential, and the red lines are the radial wavefunctions of the 30s, 40s, 50s, and 60s in the Rb atom. 23

2.4 Penetration of the low angular momentum state electrons into the Rydberg atom ionic core. 24

2.5 Two atoms with nuclei of A and B and two electrons 1 and 2. 29

2.6 Schematic of a two-level system in monochromatic laser light. Γ is the decay rate of the excited state. The ground state $|g\rangle$ with energy $\hbar\omega_g$ is coupled to the excited state $|e\rangle$ with $\hbar\omega_e$ by laser radiation of frequency ω, Rabi frequency Ω, and detuning Δ. 31

2.7 Energy level diagram of the three-level system in the presense of two laser fields. This system is used in three-level density matrix and cavity-assisted EIT calculations presented in chapter 5. The energies of the ground state $|g\rangle$, excited state $|e\rangle$, and Rydberg state $|r\rangle$ are $\hbar\omega_g$, $\hbar\omega_e$, and $\hbar\omega_r$, respectively. Δ_p and Δ_c are the detunings of the lasers from the atomic transitions. Decay of the Rydberg state is presented by Γ_r. 35

2.8 Adiabatic elimination of the intermediate level 39

2.9 (a) Shows the many-body system, which consists of ground-state atoms (blue spheres) and three excited atoms to the Rydberg state (red spheres). (b) The interaction between the Rydberg state prevents other ground state atoms in the blockaded volume (green circle) from being excited to the Rydberg state. The blockaded volume is $4/3\pi R_{bl}^3$. (c) The pairwise interaction potential between atoms 1 and 2 is $V_{12} = V_{21}$ and between atoms 2 and 3 is $V_{23} = V_{32}$. State $|e\rangle$ is adiabatically eliminated in the calculations. 41
(a) Many-body ensemble 41
(b) Blockade volume 41
(c) Pairwise interaction between three Rydberg atoms 41

3.1 One dimensional trapped atomic sample in an electric field. The figure illustrates the one dimensional distribution of super atoms excited due to the Rydberg atom blockade along the dipole trap axis. The figure defines the tilt angle of the electric field relative to the trap axis θ. . 47

3.2 The Rydberg atomic ensemble. The blue spheres are the ground-state atoms. The red spheres are the Rydberg atoms, and the volume around them indicated with green color is the blockade volume. The available fractional number for the third Rydberg blockade sphere is $0 < \mathcal{V} < 1$. 48

3.3 Interaction potential curve of the $50S_{1/2} + 50S_{1/2}$ in zero electric field. Here the source of interactions is mainly of the van der Waals type. The population of $50S_{1/2} + 50S_{1/2}$ is large for distances larger than 1.5 μm. The magnitude of the $50S_{1/2}$ component is shown for comparison with the potentials at 2370 mV cm^{-1}. The color indicates the fraction of $50S_{1/2} + 50S_{1/2}$ in the state. As can be observed in the plot, the state is almost entirely $50S_{1/2} + 50S_{1/2}$. (a) shows the potential on a scale where the curvature is evident. (b) shows the potential on the same scale as Fig. 3.4 illustrating the fact that in small electric fields the curve is energetically isolated. Consequently, the curve is predominantly $50S_{1/2} + 50S_{1/2}$ character, corresponding to the red color in the plot. 55

3.4 Pair potential for $50S_{1/2} + 50S_{1/2}$ in an electric field of 2370 mV cm^{-1} for $\theta = 0$ degrees. The darker red color shows higher $50S_{1/2} + 50S_{1/2}$ population for different internuclear distances for a constant electric field. The potential energy curves shown in the figure are very different from those with 0 applied electric field because the Stark effect causes some of the n=47 (n is the principal quantum number) Stark manifold states to intersect the $50S_{1/2} + 50S_{1/2}$ curves. This is essentially why the electric field induced dipole-dipole interaction is stronger than first calculated. The interplay between the electric field and the Rydberg atom interactions is complicated because it is highly multilevel in nature for this particular case. The zero of the energy scale is set at the field free $50S_{1/2} + 50S_{1/2}$ asymptote. 56

3.5 Tilting the electric field direction changes the potential energy surface of the interacting Rydberg atoms each in the $50S_{1/2}$ state at an electric field of 2380 mV cm^{-1}. By changing the direction of the electric field, the magnitude of the cos(θ) term in V_{eff} changes. Both the van der Waals and dipole-dipole parts of the potential energy surface are shown. Zero energy is chosen to correspond to the zero electric field $50S_{1/2} + 50S_{1/2}$ asymptote. 58
3.6 The magnitude of the dipole-dipole interaction part of the potential energy at 4.2 μm for an electric field of 2380 mV cm^{-1}. The diagram shows that the angular dependence of the potential energy surface is well-represented by a dipole-dipole interaction. The potential is attractive along $\theta = 0$ degrees and repulsive along $\theta = 90$ degrees. . . 60
3.7 This figure shows the number of Rydberg atoms per ground state atom that are excited at different electric field angles θ. The points are the data from Ref. [54]. The red dot-dashed line shows the fit from which C_3 and C_6 were obtained from the experimental data using a nonlinear least squares fit. The blue dashed line shows the results of the calculation presented in the paper. There are no fitting parameters used to plot the blue dashed line, only the experimental measured density is used for the plot. The black dot-dot-dashed line is the estimated theoretical result presented originally in Ref. [54]. The agreement between the experimental results and the full atom-pair calculation is similar to the nonlinear least squares fit of the experimental data. The right hand y-axis labels shows how the blockade radius changes as a function of θ based on the assumption that the peak ground state density is 10^{12} cm^{-3}. It is a straightforward nonlinear scaling based on how many ground state atoms fit into a blockade sphere at uniform density. . . . 64

4.1 Energy level diagram of repulsive interacting Rydberg pairs $|rr\rangle$. The blue detuned ($\Delta > 0$) excitation establishes the pair of Rydberg atoms at an internuclear distance of R_0. 67
4.2 The hard spheres that are exclusion volume created by the Rydberg blockade V_b. The V_u is the unblockaded volume. 69
4.3 Superatom picture. There is only one Rydberg atom present in the volume $4/3\pi R_{bl}^2$. R_{bl} is the blockade radius. 70
4.4 (a) Probability of Rydberg excitation. The collective Rabi frequency $\Omega_c = \sqrt{N_b}\Omega$, for one and four two-level atoms in the interaction volume. The comparison between one and four atom systems shows a collective relation, $\Omega_c = \sqrt{4}\Omega$. (b) Probability of Rydberg excitation in a superatom for a system with Rydberg state decay of $\Gamma_r = 50$ KHz. . 73
(a) $\Gamma_r = 0$ 73
(b) $\Gamma_r = 50$ KHz 73
4.5 The interaction (experimental volume) with length L. The blockade volume is shown as a green sphere at the center of the box. Blue circles are ground state atoms, and the red circle shows the excited Rydberg state. 78

4.6 Imaginary part of susceptibility for interacting many-body Rydberg gas on resonance, $\Delta = 0$. The suppression of the imaginary part of the susceptibility appears after the size of the interaction volume is reduced and reaches $L \sim 5$ μm ($V = L \times L \times L$). The system entered into the strongly interacting regime, which is the blockaded regime. 79
4.7 Imaginary part of susceptibility for interacting many-body Rydberg gas. After the length size of the interaction volume reaches $L \sim 5$ μm, there is a suppression of the imaginary part of susceptibility. The distortion of the plots at $10 \lesssim L \lesssim 4$ μm, particularly for the four atoms case, is due to the increased interaction between the atoms. In this region, some atoms are excited on different detuning (not on resonance). The imaginary part of susceptibility is proportional to the absorption signal in the experiment. Increasing the number density does not change the system response to the monochromatic laser light, and the system is in a blockaded regime. For larger interaction volumes, however, adding the number of atoms from 2 to 4 atoms in the interaction volume enhances the absorption of the monochromatic light in the system as the susceptibility increases. 80
4.8 Fluctuations in the imaginary part of susceptibility for interacting many-body Rydberg gas. Around system sizes of $L \sim 10$ μm, fluctuations in the susceptibility are increased at resonance $\Delta = 0$ MHz. This system size ($L \sim 10$ μm) is the starting point for suppressing the imaginary part of susceptibility. The fluctuations are maximum at $L \sim 5$ μm. They decrease for smaller system sizes and become close to zero for $L \sim 3$ μm, where all systems with different atom numbers show the same susceptibility. This indicates the transition between the weakly interacting regime to the strong interaction regime where the blockade volume is formed. 81
4.9 Pair correlation function $g^2(R)$, at resonance $\Delta = 0$ for different atom numbers after $t_{max} = 250\,\Omega$ evolution time, in the stationary regime. $g^2(R) = 0$ for system sizes ≤ 3 μm which corresponds to densities $\gtrsim 10^{11}$ cm^{-3}. The dashed line represents the position of the blockade radius. When the size of the system is of the order of the blockade radius, the correlation between atoms for various atom numbers gives the same correlations. 83
(a) $\Omega = 0.1$ MHz 83
(b) $\Omega = 0.2$ MHz 83
(c) $\Omega = 0.4$ MHz 83
(d) $\Omega = 1$ MHz 83
4.10 Mandel Q factor at resonance excitation $\Delta = 0$ for different system sizes and $\Omega = 0.1$ MHz. 85
4.11 The number of excited atoms for different system sizes at resonance $\Delta = 0$ MHz. At $L \approx 5$ μm, the number of Rydberg excitations for 3 and 4 atoms systems collapse to the same value. The highest fluctuation in the number of excitation (highest Q value) appears at this system size. 87

4.12 Average number of excited atoms in different volumes (densities). When the interaction volume is deceased, the suppression of the number of excited atoms appears. After interaction volume reaches $\sim 4^3\mu$m adding more atoms into the interaction volume will not change the number of excited atoms in the system. 88
4.13 Phase diagram of the system for different densities ($L = 4, 5, 10$ and 30) in Ω and Δ parameter space. f_R is the Rydberg fraction number as defined in the text. Increasing the density from $n = 1.4 \times 10^8$ cm^{-3} corresponding to system size of $L = 30$ μm to $n = 6.25 \times 10^{10}$ cm^{-3} corresponding to system size of $L = 4$ μm, The Rydberg fraction f_R, is reduced from 1 to 0.57 at maximum excitation (Red color). 95
(a) $L = 4$ μm 95
(b) $L = 5$ μm 95
(c) $L = 10$ μm 95
(d) $L = 30$ μm 95
4.14 (a) The phase diagram of the dissipative interacting Rydberg system for system size of $L = 3$ μm ($n = 10^{11}$ cm^{-3}). The phase diagram is plotted as a function of the Rabi frequency and the detuning. It shows the order parameter, the Rydberg excitation fraction f_R. The dashed line separates the phases from no excitations to when there are excitations in the system. (b) Shows the Mandel Q factor for the same system presented in (a). The super-Poissonian ($Q > 0$) region is separated from Poissonian ($Q = 0$) and sub-Poissonian ($Q < 0$) regions via the red dash line. 96
(a) $L = 3$ μm 96
(b) Mandel Q factor 96
4.15 Pair correlation funtion for different system densities in paramter Δ and Ω space. The crosshatched region shows values larger than 1.05. For smaller system sizes, higher densities, the correlated (blue color) region covers a larger portion of the Δ and Ω space. As the system size grows larger (e.g., $L = 30$), the uncorrelated region dominates. 99
(a) $L = 4$ μm 99
(b) $L = 5$ μm 99
(c) $L = 10$ μm 99
(d) $L = 30$ μm 99
4.16 Result of calculation along with linear fit to the data (red line) for Rydberg fraction f_R. The Rydberg fraction is plotted as a function of the dimensionless parameter α at resonance ($\Delta = 0$). The exponent extracted from fitting to the data is $\mathcal{V} = 0.446 \pm 0.02533$. 101
4.17 Rydberg excitation fraction as a function of dimensionless parameters α and δ. The parameter α is close to critical point $\alpha \to 0$. This region has a higher Rydberg excitation probability for $\delta > 0$. Below 0 ($\delta < 0$), the excitation of the Rydberg state goes to zero for $\alpha \to 0$. 103

4.18 Pair correlation function for α and δ space. The correlation between Rydberg excitations in the ensemble separates the parameter space into two regions for $\delta < 0$ and $\delta > 0$. Where for $\delta < 0$, $g^{(2)}(R)$ is smaller than 1 and for $\delta > 0$ it grows to values larger than 1. As we sweep the parameter space closer to the critical point $\delta = 0$ and $\alpha \to 0$, $g^{(2)}(R)$ is closer to 0, which shows correlated Rydberg excitations. 104
4.19 Mandel Q parameter showing the fluctuation in the parameter space for dimensionless parameters δ and α. For $\delta > 0$ close to the critical point $\alpha \to 0$, the system experiences super-Poissonian Rydberg excitation statistics. For $\alpha > 0$ and on resonance $\delta = 0$ the Rydberg excitation fraction shows sub-Poissonian statistics. 105
4.20 Result of density matrix calculations for Rydberg excitation fraction in parameter (δ and α) space close to the second-order phase transition. 106
4.21 Mandel Q factor for $-20 < \Delta < 20$ MHz. The fluctuation in the number of Rydberg excitation increases at off-resonant detuning for system sizes < 10 μm and is visible with the super-Poissonian nature of the curves ($Q > 0$). The Rabi frequency for this figure is $\Omega = 0.1$ MHz. 108
4.22 Pair correlation function $g^2(R)$ for different density and system sizes at $\Omega = 0.1$ MHz. $g^2(R) = 1$ for system sizes $\gtrsim 5$ μm which corresponds to densities $\approx 10^{10}$ cm^{-3}. The off-resonance (blue detuned) value for the pair correlation function in a strongly interacting regime (system sizes $3 \lesssim L \lesssim 10$ μm) is the indication of highly uncorrelated excitation. . . 109
4.23 Number of excitation for $\langle N_{Ryd} \rangle$ for different densities and system sizes at $\Omega = 0.1$ MHz. $\langle N_{Ryd} \rangle$ depicted here is for when the system is reached to the stationary state. For $\Omega = 0.1$ MHz the off-resonant excitation in the strong interaction regime for system sizes $10 \lesssim L \lesssim 3$ μm (corresponds to densities $\approx 10^{10}$ cm^{-3}) is not comparable to the excitation regime. However, the excitation shows a super-Poissonian feature. This indicates large fluctuations of Rydberg excitation in an off-resonance regime which corresponds to the fact that many atoms are collectively excited in the resonant channel. 110
4.24 Mandel Q factor for $-20 < \Delta < 20$ MHz for driving Rabi frequency of $\Omega = 0.4$ MHz. The fluctuation in the number of Rydberg excitation increases at off-resonant detuning for system sizes < 10 μm. The super-Poissonian nature of the curves ($Q > 0$) can be seen for system sizes $L \lesssim 10$ μm. 111
4.25 Pair correlation function $g^2(R)$ for different densities and system sizes for $\Omega = 0.4$ MHz laser Rabi frequency. $g^2(R) = 1$ for system sizes $\gtrsim 10$ μm which corresponds to densities $\approx 10^{10}$ cm^{-3}. The off-resonance (blue detuned) value for the correlation function in a strongly interacting regime (system sizes $3 \lesssim L \lesssim 10$ μm) is the indication of highly uncorrelated excitation. The pair correlation values for strong driving $\Omega = 0.4$ MHz is smaller compared to the $\Omega = 0.1$ case in Fig. 4.22. . . 112

4.26 Number of excitation for $\langle N_{Ryd} \rangle$ for different densities and system sizes at $\Omega = 0.4$ MHz. The system is in a stationary state. For $\Omega = 0.4$ MHz, the off-resonant excitation in the strong interaction regime, system sizes $10 \lesssim L \lesssim 3$ μm, which corresponds to densities $\approx 10^9 - 10^{11}$ cm^{-3}, is comparable to the excitation regime. However, the excitation shows super-Poissonian characteristics. This indicates large fluctuations of Rydberg excitation in the off-resonance regime, which corresponds to the fact that many atoms are collectively excited in the resonant channel. 113
4.27 The Q paramters for $\Omega = 0.1$ and $\Omega = 0.4$ MHz at 7 MHz detuning. (a) The super-Poissonian nature of the off-resonance excitation in the 0.1 graph shows higher Rydberg excitations fluctuations than the sub-Poissonian excitations in (b) at 7 MHz detuning. 115
(a) 0.1 MHz 115
(b) 0.4 MHz 115
4.28 The pair correlation function for $\Omega = 0.1$ and $\Omega = 0.4$ MHz at 7 MHz detuning. (a) shows the $g^{(2)}(R)$ for 0.1 MHz. In (a), the excitations are more likely to happen at distance R between the atoms where the sharp peaks appear and $g^2(R) > 1$. The Rydberg states at 7 MHz detuning are excited for small systems sizes $L \lesssim 5$ μm, which is the signature of the formation of Rydberg aggregates. 116
(a) 0.1 MHz 116
(b) 0.4 MHz 116
4.29 The population of Rydberg state for $\Omega = 0.1$ and $\Omega = 0.4$ MHz at resonance and off-resonance (a)$\Delta = 0$ and (b)$\Delta = 7$ MHz. The strong driving laser causes more excitation at off-resonance when $\Delta = 7$ MHz. Higher densities result in a higher population of the Rydberg state. The distance-dependent resonance of the off-resonant excitation in $\Delta = 7$ MHz detuning is visible with the sharp peaks in (b) and (d) graphs. . 117
(a) $\Omega = 0.1$ MHz $\Delta = 0$ MHz 117
(b) $\Omega = 0.1$ MHz $\Delta = 7$ MHz 117
(c) $\Omega = 0.4$ MHz $\Delta = 0$ MHz 117
(d) $\Omega = 0.4$ MHz $\Delta = 0$ MHz 117

5.1 (a) Energy levels of the ^{87}Rb that is used for the three-level density matrix calculations and also for the Rydberg EIT experiment. State $|1\rangle$ is $|5S_{1/2}\rangle$, the intermediate state is $|2\rangle = |5P_{3/2}\rangle$, and the Rydberg state $|3\rangle$ is level nS or nD. (b) Schematic of the experimental setup. . 120

5.2 (a) Real and imaginary part of the susceptibility. The absorption (imaginary) $\omega_p(l/2L)\chi^{"}$, is shown in a blue dashed line. The dispersion (real) $\omega_p(l/2L)\chi^{'}$ is shown in red. χ is found through density matrix calculation for two three-level atoms with the atomic density of $\sim 10^9$ cm^{-3} inside the cavity. The crossing between the detuning curve, $-\Delta$, and the dispersion curve shows the position of the transmission peaks. There are five points where the two curves intersect. (b) Shows the cavity transmission spectrum versus probe detuning. This cavity transmission spectrum is plotted substituting calculated χ into the Eq. 5.4. 125
5.3 The position of the cavity transmission peaks for both theory and experiment data for the $35S_{1/2}$ Rydberg state. The position of the peaks is plotted as a function of cavity detuning $\Delta_{cav}/2\pi$ when the coupling detuning, $\Delta_c/2\pi$ is 0. For the theory calculations, the experimental parameters are used. Probe Rabi frequency $\Omega_p/2\pi = 9.1$ MHz, coupling Rabi frequency $\Omega_c/2\pi = 4.1$ MHz. In the experiment, there are 25 atoms in the interaction region, while in theory, there are two atoms in a smaller volume to account for the same experimental density of $\sim 8\times10^8$ cm^{-3}. The decay rate of the Rydberg state (including blackbody) is $\Gamma_3 = 53$ KHz. The decay rate of the intermediate state $|5P_{3/2}\rangle$ is $\Gamma_2 = 6$ MHz. 128
5.4 Density matrix calculations for the cavity transmission spectrum versus probe detuning as a function of cavity detuning $\Delta_{cav}/2\pi$, when the coupling detuning, $\Delta_c/2\pi$ is 0. This cavity transmission spectrum is plotted substituting calculated χ into the Eq. 5.4. 129
5.5 The position of the cavity transmission peaks for both theory and experiment data. These positions of the peaks are plotted as a function of coupling laser detuning $\Delta_c/2\pi$ when the cavity detuning, $\Delta_{cav}/2\pi$ is 0 MHz. 130
5.6 Density matrix calculations for the cavity transmission spectrum versus probe detuning as a function of coupling laser detuning $\Delta_c/2\pi$, when the cavity detuning, $\Delta_{cav}/2\pi$ is 0. This cavity transmission spectrum is plotted by substituting calculated χ into the Eq. 5.4. 131
5.7 Pair potential calculations of the (a) $35S_{1/2}$+$35S_{1/2}$, (b) $45S_{1/2}$+$45S_{1/2}$, (c) $55S_{1/2}$+$55S_{1/2}$, and (d) $65S_{1/2}$+$65S_{1/2}$ states. The background electric field is 1.6 Vcm^{-1}, and the angle of the electric field with respect to the internuclear axis is 0 degrees ($\theta = 0^o$). The black curve shows the population of the pair state. The darker black color shows higher population of (a) $35S_{1/2}$+$35S_{1/2}$, (b) $45S_{1/2}$+$45S_{1/2}$, (c) $55S_{1/2}$+$55S_{1/2}$, and (d) $65S_{1/2}$+$65S_{1/2}$ state. 133
(a) $35S_{1/2}$+$35S_{1/2}$ 133
(b) $45S_{1/2}$+$45S_{1/2}$ 133
(c) $55S_{1/2}$+$55S_{1/2}$ 133
(d) $65S_{1/2}$+$65S_{1/2}$ 133

Abstract

This thesis presents a study of the interactions between two Rydberg atoms and Rydberg atomic ensemble with a monochromatic light field. The first part of the thesis covers the interaction between two Rydberg atoms. The result of this calculation for two Rydberg atoms is compared to an experiment and single atom Stark shift calculations. The pair-potential curves for interacting Rydberg atoms in a constant electric field are calculated. We use the pair-potentials to determine the effective dipole-dipole coefficient C_3, and van der Waals coefficients C_6. We compared the C_3 and C_6 coefficients to the experimental results. The experiment is performed for a quasi one dimensional trap at ultracold temperatures. In the experiment the angle of a polarizing electric field is varied with respect to the trap axis. The dipoles produced via polarization of the atoms have an angular dependent dipole-dipole interaction. We focused on two Rubidium Rydberg atoms in $50S_{1/2}$ states interacting in the blockade regime. For internuclear distances close to the blockade radius $R_{bl} \approx 4$–6 μm, molecular calculations are in much better agreement with experimental results compared to those based on the properties of single atoms. The calculation based on single and independent atoms for C_3 and C_6 was used to analyze the original experiment. Our result shows that the calculated C_6 coefficient is within 8% of the experimental value while the C_3 coefficient is within 20% of the experimental value.

The second part of the thesis is a theoretical study of the interaction between

a few atoms in a Rydberg ensemble in a monochromatic light field. We presented the solution of the full many-body master equation for an ensemble of two-level atoms. For a few atoms, through a full many-body master equation, it is possible to capture the main features of the physics of the problem. Our results demonstrate the capability of a full many-body master equation with a few atoms to investigate the novel quantum phases in long-range interacting quantum systems. The system's response to the driving laser field was studied by calculating the susceptibility, the correlation between Rydberg excitations, and excitation statistics. We studied the time evolution and the medium's response to the applied optical field. We calculated the linear dispersive and absorptive parts (χ_R and χ_I) of the susceptibility of the medium for various densities of the atomic ensemble. The nature of interactions between the atoms follows the van der Waals behavior and is inversely proportional to the sixth power of the internuclear distance, R, between two atoms $\propto 1/R^6$. In our calculations, we randomly generate the atoms' positions in a three-dimensional experimental box. This results in shot-to-shot fluctuations of the observables, such as susceptibility, which depends on atoms' positions relative to each other. The fluctuation of the observables (susceptibility and Rydberg excitations) happens around the transition boundary between two phases of the system. These fluctuations are quantum fluctuations since the temperature is set to be zero in the calculations. The critical parameters at which the transition of the system happens, such as critical density n_{crit}, are presented. We found that the system of interacting

Rydberg atoms experiences a phase transition (at resonance, $\Delta = 0$) from a classical individual interacting atoms in the weakly interacting regime into a many-body quantum interacting regime in the strongly interacting regime at critical density $1.6 \times 10^{10} \lesssim n_{crit} \lesssim 6.25 \times 10^{10}$ cm^{-3}. We found the Rydberg blockade radius R_{bl}, through the pair correlation function by sweeping the parameter space (Ω and Δ). Defining the reduced control parameter α and δ, we investigated the features of the second-order phase transition close to the transition critical point ($\alpha \to 0$ and $\delta = 0$). We define the order parameter to be the Rydberg excitation fraction f_R. The phases are separated by analyzing the behavior of this order parameter. f_R shows a power-law behavior close to the critical point with critical exponent $\mathcal{V} \sim 0.446$.

In the last part, the full many-body master equation for an ensemble of three-level atoms inside a cavity is presented. We investigated the result of the cavity quantum electrodynamics (CQED) experiment in our group. We calculated the susceptibility through a full many-body density matrix calculations and used its result to study the transmitted light from the cavity. In the experimental analysis, the effect of the interaction between atoms is not considered. However, this can affect the result obtained through the many-body master equation calculations where these effects are considered. The future goal for the CQED experiment is to observe single-photon source by means of Rydberg blockade in the cavity. For this reason, the interactions between atoms need to be considered in the

calculation and experimental analysis. To examine the effect of adsorbates on the surfaces of the mirrors of the cavity, we performed a pair-potential calculation in the background electric field of 1.6 V/cm created by the absorbates.

Chapter 1

Introduction

Atoms that are excited to a high principal quantum number (e.g., $n = 50$), where n is the principal quantum number, are called Rydberg atoms. Rydberg states can be created in different systems such as atoms [1], molecules [2, 3], or solids [4]. In 1890, Swedish physicist Johannes Robert Rydberg (1854–1919) described the spectral lines emitted by atoms that have a single valence electron and discovered a simple formula describing the frequencies of the emitted lines [5]. According to Rydberg's formula, the energy of the n^{th} level is given by

$$E_n = \frac{-R_H}{n^2}, \tag{1.1}$$

where R_H is the Rydberg constant for Hydrogen, and n is the principal quantum number. Energy levels of any system similar to Hydrogen can be described by a modified form of a Rydberg formula. In 1965, after many technological advancements, the first high quantum number Rydberg state was observed [6]. The detected microwave radiation belonged to the Hydrogen emission Line ($\mathrm{n}_{110} \rightarrow \mathrm{n}_{109}$), which was easily explained with the Rydberg formula (Eq. 1.1). Looking at an alkali Rydberg atom energy diagram, one can find transitions covering almost all of the electromagnetic spectrum Fig. 1.1 [7]. That means there is a possibility of coupling any regions in the frequency domain of the electromagnetic spectrum to one another, for instance, from the optical region to the microwave region. This provides a large coupling tuneability to the

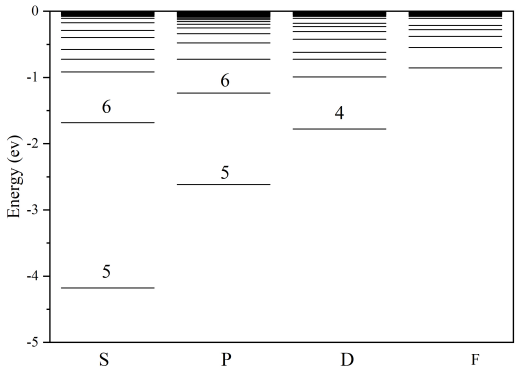

Figure 1.1: Energy level diagram of a Rubidium atom.

electromagnetic field and establishes a broad area of applicability for Rydberg atom systems [8, 9].

With the advancement of technology and especially lasers around 1970, many groups achieved the highly excited Rydberg atomic ensembles in the laboratory. Around the 1990s, the development of laser cooling and trapping of atoms provided a great coherent control over external and internal degrees of freedom of an atomic cloud. Such developments make it possible to create Rydberg atom ensembles with very high densities ($\sim 10^{12}$ cm^{-3}) and in the micro-kelvin temperature regime [10]. One of the remarkable consequences of such a control is the frozen Rydberg gas in which the atoms are considered to be frozen in the time scale of the experiment in which one can neglect the blackbody radiation and movement of the atoms [11, 12]. In such atomic samples, the long-range van der Waals interactions become important, and usually, the thermal motion of atoms

can be neglected [12]. The interaction energies between Rydberg atoms exceed any other energy scale in micro-kelvin temperature and can be up to several GHz. The long-range interaction in excited Rydberg atoms is different from what can be found between atoms with high magnetic moments [13] or polar molecules [14]. Excited ultra-cold atoms in Rydberg states provide an enormous level of control in the interaction potential and a great degree of tunability in their atomic properties [1]. Considering both control over internal and external degrees of freedom for atomic clouds and tunable long-range interactions makes the Rydberg system an ideal case to study fundamental quantum physics and many applications such as quantum simulation, quantum computation, and quantum optics [15].

Before the year 2000, many studies of Rydberg systems were focused on their spectroscopic aspects. After 2000, several studies on Rydberg systems [16, 17, 18] revealed the application aspect of Rydberg atoms in quantum information science which became a basis for interdisciplinary Rydberg physics that offer a broad range of applications in other areas of physics. The vast application of Rydberg atoms in the field of physics is due to their exotic properties. Because of the highly excited electron of the Rydberg atom, their wavefunctions are expanded from the size of their ground-state of 0.1 nm to several hundred nanometers or even μm. The size of a Rydberg atom is scaled with the principal quantum number n [1]. Therefore, Rydberg atoms possess an enormous electric dipole

where the excited electron is loosely bound to its ionic core. This makes Rydberg atoms very sensitive to their environment. As a result, the non-interacting ground state atoms, when excited to the Rydberg state, strongly interact with other Rydberg atoms or with the surrounding electromagnetic fields. The interaction between Rydberg atoms is typically more than ten orders of magnitude stronger than the interaction between ground state atoms [19]. The choice of the excited state sets the magnitude of the interactions between Rydberg atoms, which can exceed all other relevant energy scales on distances of several microns. This leads to an ensemble in which the interactions between its components (Rydberg atoms) are dominated by long-range interactions [20]. The main source of motivation behind many experiments in Rydberg physics is to take advantage of the strong interaction mechanism among Rydberg atoms and their surrounding fields. The strong interaction becomes most visible at large atomic densities that can be found in ultracold gases [15]. Based on phenomena that embedded in the interaction between Rydberg atoms, the vast, dynamical, and interdisciplinary applications of the Rydberg field showed itself in interacting Rydberg lattice gas [21], dipolar quantum gases [22], formation of molecules [23, 24], effects of electric fields on ultracold Rydberg atom interactions [25], collisions between Rydberg atoms [26, 27, 28], dipole-dipole and van der Waals interactions [29, 30], the Rydberg atom blockade effect for creating collective excitations [31, 32], generating qubits [19], microwave sensor [8, 9, 33, 34], quantum optics and nonlinear optics with Rydberg atoms [35, 36, 37, 38], photonic gates [39],

quantum internet or computers [40, 41] and quantum repeaters [42, 43]. The two important concepts in Rydberg atom systems which are based on the interaction between Rydberg atoms are Rydberg blockade and collective Rabi oscillations presented in the year 2000-2001 [16, 17, 44, 45]. The subject of this thesis is mainly focused on a study of such systems and the interaction mechanisms between its components and surrounding fields. The prominent result of the strong interaction between Rydberg atoms is an excitation blockade. When two Rydberg atoms are placed close to each other, the presence of the second Rydberg atom will change the energy required for a ground state atom in the vicinity to be excited to the Rydberg state. This energy change creates a density limitation for the Rydberg atomic population due to the strong interaction between two nearby Rydberg atoms and is referred to as the Rydberg blockade effect. The schematic in Fig. 1.2 shows that as the atoms are brought closer to each other, the excitation energy for the second atom to the Rydberg state is changed and becomes larger than the line width of the excitation laser. The excitation of the second atom to the Rydberg state is blockaded, and two Rydberg excited atoms can never appear at a distance smaller than the blockade radius R_{bl} from each other. One consequence of the Rydberg blockade phenomena in a perfectly blockaded ensemble is that only one atom can be excited to the Rydberg state. It means that for a perfectly coherent excitation process, it is not possible to distinguish between Rydberg excited states. The entire system is in a symmetric

superposition of all possible singly excited states. Quantum mechanically this results in a collective enhancement of excitation coupling to the incident light, which is shown in Fig 1.3 [17, 44, 45].

In a typical cold atom experiment with high density, many atoms are present in the interaction volume. For instance, in a blockaded Rydberg ensemble with a density of 10^{10} cm^{-3}, the average distance between atoms is about $2.5\,\mu$m. This means if the blockade radius is about $R_{bl} = 2.5\,\mu$m, on average, we can excite one atom to the Rydberg state in the blockade volume. A schematic of a Rydberg blockaded ensemble is shown in Fig. 1.4.

In this thesis, we first start by studying the interaction between a pair of Rydberg atoms in the presence of a background electric field. In 1997, the perturbative study of the interaction potentials for the np–np asymptotes of states for low principal quantum numbers (n) was performed [46]. The perturbative study was based on previous work (in 1966) on the analysis of asymptotic van-der-Waals interaction terms [47]. Later this approach was applied to a high quantum Rydberg state [48]. Direct diagonalization (non-perturbative) of the Hamiltonian approach is also used to study the Rydberg pair interactions quantitatively [49, 50, 51]. By diagonalization of the Hamiltonian of a Rydberg atom pair system, we compared our results to an experiment [52] and found a better agreement with the experimental values [52, 53]. We calculate the pair-potentials of ^{87}Rb atoms excited to the highest quantum state $|50S\rangle$. In the presence of the external electric field, the interaction potentials between

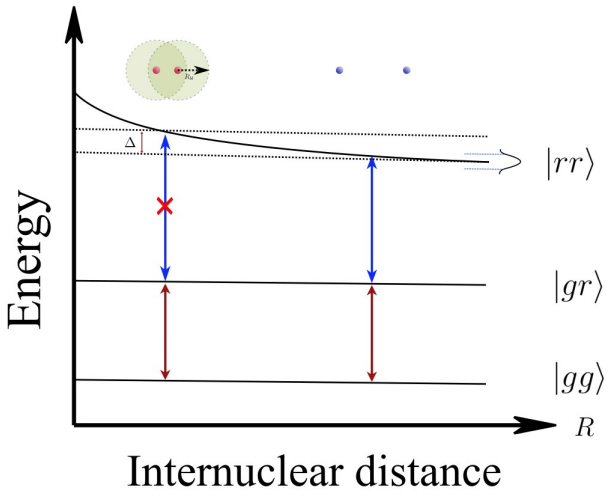

Figure 1.2: Energy level diagram of interacting Rydberg pairs $|rr\rangle$. This diagram shows the mechanism for the formation of the blockade volume. When the atoms are far away, the interaction between them is minimal, and both atoms can be excited to the Rydberg state simultaneously. However, as they get closer to each other, the energy required to excite the second atom goes out of the reach of the laser linewidth, and the blockade volume around them is formed. In the blockade volume, only one atom can be excited to the Rydberg state $|r\rangle$.

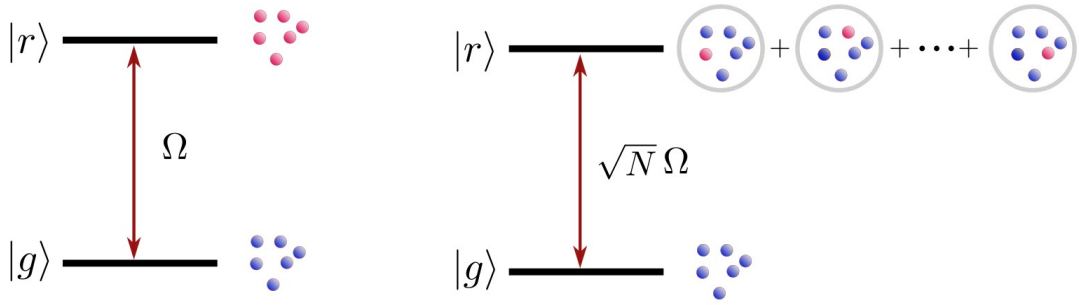

Figure 1.3: Excitation of an ensemble of two-level atoms. (a) Shows an ensemble of N non-interacting atoms. Ω is the coupling strength. All atoms can be excited simultaneously to the Rydberg state. (b) Shows an ensemble of N interacting atoms in a blockaded volume in which only one excitation is possible and atoms are collectively excited to the Rydberg state with $|r\rangle = \frac{1}{\sqrt{N}} \sum_i |g_1 + g_2 + ... + r_i + g_{N-1}, g_N\rangle$. The collective Rabi frequency excites atoms to the Rydberg state $\sqrt{N}$ faster than the non-interacting system.

Rydberg atoms depend on the magnitude and direction of an applied electric field. For example, one can change the strength of the interaction by changing the orientation of an applied electric field and engineering the interaction between the Rydberg atoms [52]. Applying a background electric field to the system polarizes the Rydberg atoms and creates permanent dipole moments in each atom. The background electric field causes the atomic state energies of the Rydberg atoms to be shifted and mixes the field-free states. Although neglecting electric fields in the calculations is quite common, many experiments have a

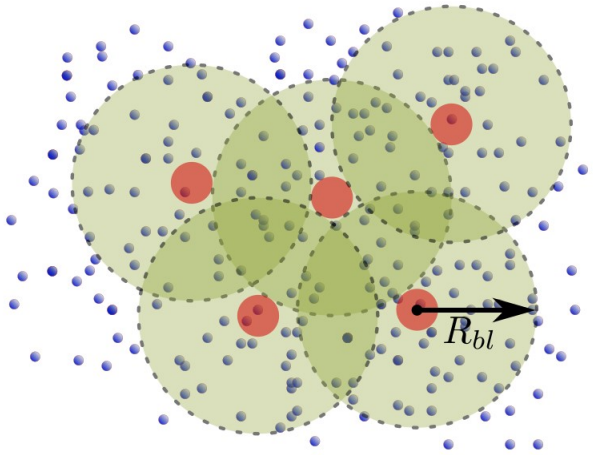

Figure 1.4: Rydberg atomic ensemble. The blue spheres are the ground-state atoms. The red spheres are the Rydberg atoms, and the volume around them, indicated with green color, is the blockade volume. In each blockaded volume, only one Rydberg atom can exist.

small background electric field, and studying such effects is of prime importance. In the experiment, it was shown that one could enhance or suppress the blockade effect in a quasi one dimensional sample of Rubidium atoms by tilting the applied electric field by an angle, θ, with respect to the axis of the sample [54].

In the second part of the thesis, we focus on the many-body characteristic of the ensemble of Rydberg atoms and their collective behavior. Dicke was first to mention that we can not always treat the atomic sample coupled to an electric field as a collection of independent atoms [55]. The critical point of Dicke's theory is when comparing the behavior of the many atom systems to a single atom. Compared to a single atom system, the atom–field coupling of a many-atom

system is magnified by a factor of $\sqrt{N}$, where N is the number of atoms. The collective behavior of the ensemble of atoms is a demonstration of quantum mechanics at mesoscopic scales. The unique properties of Rydberg atoms are the key to realizing and investigating the quantum many-body Hamiltonians and their phases. The blockade phenomena, which is rooted in strong interaction between Rydberg atoms, allows for the creation of such a many-body systems [20]. However, the long-range interactions which lead to the emergence of strong many-body correlations create a tremendous theoretical challenge on the calculations of observable values of interacting Rydberg systems in the presence of an incident light (e.g. laser light). At the macroscopic level, Maxwell's equations in a medium describe the light-matter interaction. The Maxwell theory is a mean-field theory of electromagnetism. The representation of the electric susceptibility, conductivity, and permittivity in Maxwell's theory at the microscopic level does not provide a complete physical picture [56]. On the other hand, theoretically studying the light-matter interaction at the sub-atomic level like a simple interacting electric dipole system becomes intractable as the number of dipoles, N, increases from few to many. Thus studying and understanding the behavior of such systems with simple models at the sub-atomic level is crucial. The atomic medium's response to exposed light is the basis of many interesting phenomena such as electromagnetically induced transparency (EIT), slow light [57, 58], fast light [59, 60, 61], large refractive index [62], stored light [63], nonlinear

optics [64], and many other remarkable phenomena [65]. When light is exposed on a medium, the medium's index of refraction and its susceptibility characterize the medium's response to the exposed light. If the light passes through the medium, the transmitted light can be attenuated and phase-shifted depending on the medium susceptibility. In chapter 4 we study these effects and calculate the susceptibility of a Rydberg ensemble in the presence of the incident light. Having control over the medium's susceptibility will result in controlled manipulating of the light properties that pass through a medium.

It was in 2004 that for the first time, the excitation suppression due to interaction effects was reported [66, 31]. From 2005 to 2013, many groups performed counting statistics of the Rydberg excitation and showed that the blockade mechanism in Rydberg atoms systems could lead to a dense packing of blockade spheres [67, 68, 69]. From 2009 to 2012, the collective Rabi oscillations of two and many atoms were observed [44, 45]. Also, distance selective off-resonance excitation due to the interaction between Rydberg atoms and formation of aggregates was shown in [45, 70, 71, 72, 73, 74]. Many groups also worked on techniques for measuring spatially resolved observables in Rydberg excited ensembles [75]. In 2002 the study on phases of Hamiltonian of interacting Rydberg system was done [76]. This study showed that the interacting Rydberg system undergoes a phase transition from a superfluid to a Mott insulator. In 2008-09 the critical behavior and universal scaling of the interacting Rydberg

system were studied [77, 78]. These studies showed that interacting Rydberg systems, in analogy to condensed matter systems (magnetic systems), experience second-order phase transition. The power-law behavior of the order parameter near the critical point was observed [77, 78].

To study the interacting Rydberg system, many theoretical methods have been presented over the past years. One of the most studied methods is the mean-field model, which simplifies the simulation of the interacting Rydberg systems greatly [31, 77]. That makes it possible for many interacting components of the system to be considered in the calculations; however, its drawback is in calculating the correlations between those components. Another method that made it possible to calculate the observables of the system for the systems with many atoms is the rate equations method presented in 2007 [79]. However, with the rate equation, one cannot calculate the exact two-body correlations. In 2010 the cluster expansion method was used to study the interacting Rydberg systems [80]. The cluster expansion method can be considered as an improved mean-field model in which one can include the exact two-body correlations.

In this thesis, the study of the many-body interacting Rydberg ensemble in the presence of incident laser light is done by considering an ensemble of ultracold atoms with different densities exposed to a different driving field. The interaction between atoms is a pair-wise interaction. Our system consists of a few atoms that can be excited to Rydberg state by interacting with incident light and

spontaneously decay to the ground state. In our calculation, we use the Lindblad master equation with a density matrix to explore the dynamics of the excitations and study the behavior of the system when the control parameters of the system, such as density of the atomic cloud or the strength of the coupling light, are changed. The excitation dynamics of such systems based on the microscopic description and their transition from weak to strongly correlated quantum systems where the excitation to the Rydberg state is suppressed are explored. This thesis aims to bridge the theoretical investigation of the interacting Rydberg system and their experimental counterpart with only a few atoms in different system sizes and densities.

The structure of this thesis is as follows. Chapter 2 explains the important properties of Rydberg atoms and the Rydberg atomic systems. Then it presents the theoretical background of our pair-potential calculations. The mechanism of the many-body two-level atom system interacting with incident light is explained. Accordingly, the basis of how the study is performed on the dynamics of excitations of dissipative Rydberg systems where one can use the Lindblad master equation and extract the observables from its solution is presented in this chapter. The Hamiltonian of the two and three-level system in the presence of incident light, density matrix calculations, and different observables such as the pair correlation function of the Rydberg ensemble are introduced in this chapter.

Chapter 3 presents the result of pair-potential calculation of two Rydberg

atoms excited into $|50S\rangle$ quantum state. The pair-potential calculations are done in the presence of various background electric fields with different orientations with respect to the internuclear axis. Then a comparison between the Rydberg pair- potential results to the single atom Stark shift calculations and Rydberg blockaded experimental results is done. This chapter expresses why the single atom Stark shift calculation does not provide a reliable result compared to the experiment.

In chapter 4, the light-matter interaction of several Rydberg atomic ensembles is studied. We drive the response of an atomic cloud of Rydberg atoms to the incident light. In this chapter, we then study the collective behavior of the system and drive pair correlations and Rydberg excitation statistics for different system dimensions and densities. The concept of quantum phase transition in the Rydberg atomic ensemble is explained. It is shown that even in a system with a few atoms, one can see the signature of a phase transition from weakly interacting isolated atom excitation to the strongly interacting collective excitation regime. In this chapter, the ensemble of atoms consists of a few (up to four) with different system sizes and consequently different densities. The analogy between condensed matter systems of magnetic systems and Rydberg atomic ensemble is made in this chapter with the means of the Ising model. We show that density matrix calculations in the Lindblad master equation for a few atoms can extract important observables of the system and reveal the significance of a

phase transition in the Rydberg ensemble of atoms.

In chapter 5 the result of light-matter interaction for a three-level system of Rydberg ensemble for a few atoms inside an optical cavity is presented. The calculation result is compared to the experimental results obtained in our group. The calculated susceptibility from the Lindblad equation for a three-level ensemble of Rydberg atoms is used in a classical equation for the light transmitted through an optical cavity.

Chapter 6 presents the conclusion and suggests possible future directions of this work.

Chapter 2

Theoretical Background

This chapter describes the properties of Rydberg atoms. These properties are used in our theoretical calculations. The nature of the interaction between Rydberg atoms is explained. This part serves as a basis for our pair interaction calculations and later in the density matrix calculations. In the Rydberg atomic ensemble, the interaction between Rydberg atoms can result in many phenomena, such as Rydberg blockade [53, 35], Rydberg antiblockade [81], single-photon generation [82], and bunching and antibunching of photons [83, 84]. The Rydberg blockade mechanism is discussed in this chapter. In addition, the interaction between a Rydberg atomic ensemble and monochromatic laser light is explained. The density matrix calculations are used to study these types of interactions.

2.1 Properties of Rydberg atoms

2.1.1 Energies of the Rydberg state

The energy state of the Rydberg atom is very similar to the Hydrogen atom. The excited electron of a Rydberg atom usually orbits far from the ionic core, where inner electrons stay close to the nucleus and construct an ionic core. When the excited electron is outside of the ionic core, the ionic core consists of the nucleus and the surrounding cloud of inner core electrons. The cloud of the

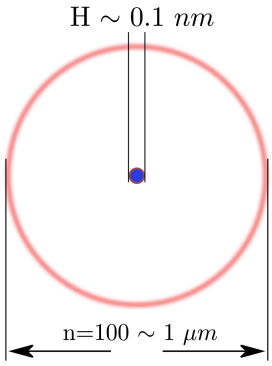

Figure 2.1: Size of a typical Rydberg atom in comparison to a Hydrogen atom.

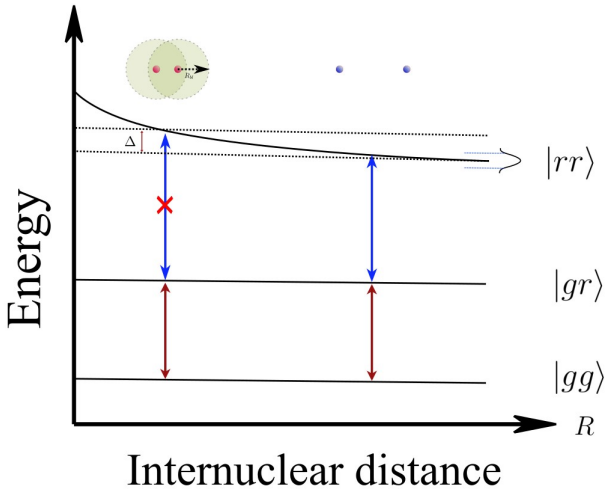

Figure 2.2: Excitation of the second Rydberg atom is blockaded due to the interaction between atoms.

inner electrons screens the nucleus charge making a $+e$ net charge for the core. If the ionic core of the Rydberg atom is considered as a point positive charge, the Coulombic interaction between the core and the excited electron is similar to the Hydrogen atom. In this case, the state energies of the Rydberg atoms are

similar to the Hydrogen atom. However, the Rydberg atom ionic core has a finite size and charge distribution. This causes Rydberg atoms to be different from Hydrogen atoms as the outer excited electron can penetrate into the ionic core and interact with ionic core electrons. When the excited electron is inside the ionic core, the screening effect of the nuclear charge caused by the inner electrons does not apply anymore, and the potential is not a pure Coulombic potential. The screening of the nuclear charge varies depending on the state of the excited electron and is dependent on principal quantum number n, the orbital angular momentum l, and the total angular momentum j. The interactions between the ionic core and the excited electron should be considered for calculating the Rydberg state energies, which make the energies of the Rydberg atom different compared to the Hydrogen atom. These interactions are most important for the lower angular momentum states ($l < 3$) because the electron has a higher probability of penetrating into the ionic core. Higher angular momentum states ($l \geq 3$) can be well approximated as Hydrogenic states because the centrifugal barrier pushes the electron away from the core. As an example, the ng ($l = 4$) wavefunction is pushed out from the core and essentially sees the core as a positive charge which is not the case for the s electron. Electrons in the s state can penetrate further inside the core and interact with the core electrons. Therefore, the nuclear charge screening by other electrons in the atom is less effective for ns configurations than ng. Thus, the s electrons have lower energy than g electrons for the same principal quantum number. The difference between

Hydrogen and the alkali Rydberg atoms state energies are accounted for by introducing the quantum defect δ_{nlj}. A modification of Bohr's formula Eq. 1.1 considers the reduced screening of nuclear charge for electrons with lower l. Subtracting the quantum defect δ_{nlj} from the principal quantum number n gives the energy E_{nlj} [1],

$$E_{nlj} = -\frac{R_y}{n^{*2}}. \tag{2.1}$$

Here the R_y is the Rydberg constant, and $n^* = n - \delta_{nlj}$ is the effective principal quantum number. The quantum defect can be directly related to the phase shift relative to Hydrogen that occurs in the electronic wavefunction because of the interaction with the ionic core [85, 86]. The quantum defect dependence on the total angular momentum, j, and the principal quantum number, n, is small. The quantum defect, δ_{nlj} , can be written as an expansion in powers of $(n - \delta_0(l, j))$,

$$\delta_{nlj} = \delta_0(l, j) + \sum_{k=0}^{\infty} \frac{\delta_{2k}(l, j)}{(n - \delta_0(l, j))^{2k}}, \tag{2.2}$$

where $\delta_0(l, j)$ is the zeroth-order term of the expansion. The expansion coefficients $\delta_{2k}(l, j)$ are found experimentally by fitting energy levels of Rb to the energy equation 2.1 [87, 88, 89]. The values of the δ_0 and δ_2 for Rb in this thesis are given in Table 2.1.

State	Parameters	Values
$ns_{\frac{1}{2}}$	δ_0	3.1311804
	δ_2	0.1784
$np_{\frac{1}{2}}$	δ_0	2.6548849
	δ_2	0.2900
$np_{\frac{3}{2}}$	δ_0	2.6416737
	δ_2	0.2950
$nd_{\frac{3}{2}}$	δ_0	1.3480948
	δ_2	-0.6054
$nd_{\frac{5}{2}}$	δ_0	1.3464622
	δ_2	-0.5940
$nf_{\frac{5}{2}}$	δ_0	0.016591
	δ_2	-0.085
$nf_{\frac{7}{2}}$	δ_0	0.0165437
	δ_2	-0.086
$ng_{\frac{7}{2}}$	δ_0	0.00405
	δ_2	0
$ng_{\frac{9}{2}}$	δ_0	0.00405
	δ_2	0

Table 2.1: Quantum defect parameters δ_0 and δ_2, used in this thesis for Rb. The effective principal quantum number n^*, for Rb in the $50S_{1/2}$ states is $n^* = 46.8687$. For higher angular momentum states $l > 3$, the quantum defect is acceptably negligible.

2.1.2 Wavefunctions

In our calculations, the wavefunctions of Rydberg atoms are needed to calculate the behavior of the Rydberg state interacting with the laser light or with other atoms in the system. Because of the similarities between alkali Rydberg atoms and Hydrogen atoms, the wavefunction of the Rydberg atom can be calculated

by solving the Schrödinger equation in a similar way as for a Hydrogen atom.

$$\left(\frac{1}{2}\bigtriangledown^2 + V(r)\right)\psi(\mathbf{r}) = -E\psi(\mathbf{r}). \tag{2.3}$$

In this equation, $\psi(\mathbf{r})$ is the wavefunction. Separating the radial and angular variables and solving the Schrödinger equation Eq. 2.3, results in radial $R_{n,l}(r)$, and angular $Y_{l,m}(\theta,\phi)$, parts of the total wavefunction $\psi(\mathbf{r}) = R_{n,l}(r)Y_{l,m}(\theta,\phi)$. For the Hydrogen atom, the potential $V(r)$ in Eq. 2.3 is a Coulomb potential. However, for the reasons discussed in section 2.1.1 and because of the penetration of the excited electron into the ionic core, the potential in the Schrödinger equation is not a pure Coulomb potential anymore. Instead, we use a modified l-dependent potential V_l, which is defined as [90],

$$V_l(r) = -\frac{Z_l(r)}{r} - \frac{\alpha_c}{2r^4}[1 - e^{-(r/r_c)^6}]. \tag{2.4}$$

In this model, α_c is the static dipole polarizability of the ionic core, and r_c is the cutoff radius of the ionic core. The first term in the Eq. 2.4 is the Coulomb potential. The second term accounts for the polarization interaction between the excited Rydberg electron and the ionic core. In Eq. 2.4, $Z_l(r)$ is the radial charge parameter which is given by [90],

$$Z_l(r) = 1 + (z-1)e^{-a_1 r} - r(a_3 + a_4 r)e^{-a_2 r}. \tag{2.5}$$

Here, z is the nuclear charge of the atom. $a_1 - a_4$ are fitting parameters found by a nonlinear fit of Eq. 2.4 to the Rydberg atom energies for a series of quantum states where for each value of angular momentum l (i.e. $l = 0, 1, 2, 3$) α_c is kept

fixed. A minimum of five measured energies is used in the fitting procedure [90]. A list of constants for calculating the Rydberg atom wavefunction is presented in Table 2.2. The radial part of the Schrödinger equation can be solved numerically by using a Fortran program called RADIAL [91]. An example of the output of the program is shown in Fig 2.3. The potential expressed in Eq. 2.4 is shown in blue. The radial wavefunctions corresponding to the $30s$, $40s$, $50s$, and $60s$ Rydberg states for Rb are shown in red. For the angular part of the wavefunction $Y_{l,m}(\theta, \phi)$, since all the interaction between the excited electron and the ionic core is expressed in the radial part of the Schrödinger equation, the spherical harmonics calculated for the Hydrogen atom are used in our calculations. Depending on the angular state of the excited electron in the Rydberg atom, in this thesis, wavefunctions for Rydberg atoms are calculated for two different ranges of l. For high l quantum numbers $l > 3$, and for low l quantum numbers $l \leq 3$. For $l > 3$ states, since the inner core electrons screen the nuclear charge in the ionic core and the excited electron does not penetrate into the ionic core, the V_l becomes a Coulomb potential. Thus, Hydrogenic wavefunctions are used in our calculations for the high l values. For low l quantum numbers $l \leq 3$, we use the l-dependent model potential V_l in the Schrödinger equation. An illustration of the electron penetration into the ionic core for the low angular quantum numbers $l \leq 3$ is shown in Fig 2.4.

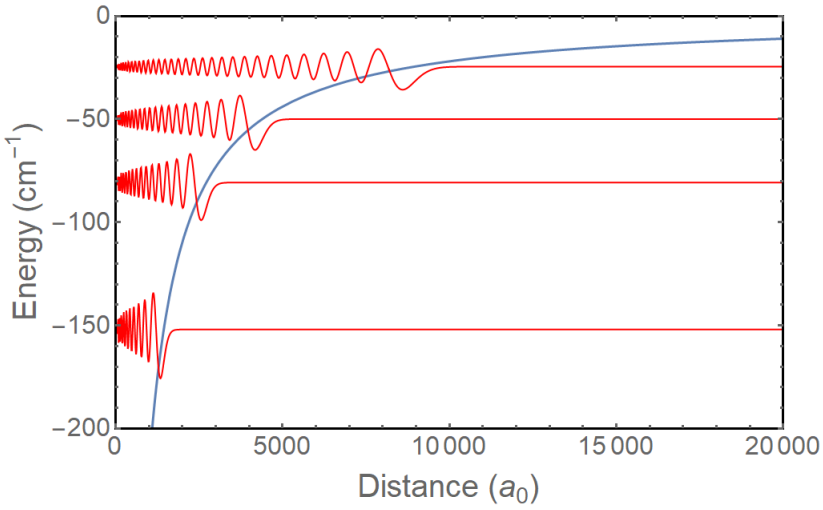

Figure 2.3: Radial wavefunctions of Rb Rydberg atoms generated using the RADIAL program [91]. The blue line is the l-dependent potential, and the red lines are the radial wavefunctions of the 30s, 40s, 50s, and 60s in the Rb atom.

L	a_1	a_2	a_3	a_4	r_c
0	3.69628474	1.64915255	-9.86069196	0.19579987	1.66242117
1	4.44088978	1.92828831	-16.79597770	-0.81633314	1.50195124
2	3.78717363	1.57027864	-11.65588970	0.52942835	4.86851938
3	2.39848933	1.76810544	-12.07106780	0.77256589	4.79831327

Table 2.2: Constants used for calculating the Rydberg atom wavefunctions.

2.2 Rydberg pair interactions

The interactions between two Rydberg atoms that are separated by a distance R are mainly electrostatic. For atoms in $n \approx 1, 2, 3$ levels, the interaction can be calculated using the *ab initio* numerical techniques. However, using the same

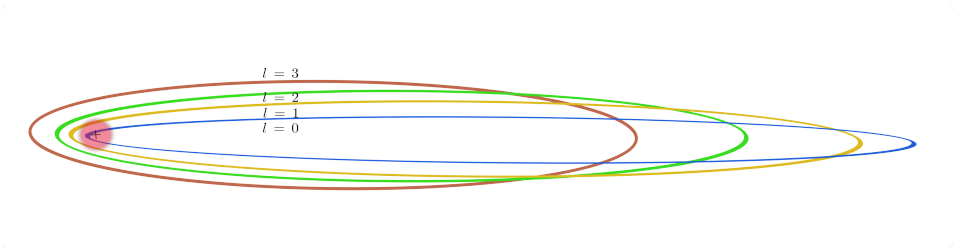

Figure 2.4: Penetration of the low angular momentum state electrons into the Rydberg atom ionic core.

ab initio calculations to study the interaction between highly excited Rydberg states is impractical. This problem can be simplified by using the multipole expansion of the interaction operator [92, 93],

$$V(\mathbf{R}, \mathbf{r}_{1A}, \mathbf{r}_{2B}) = \sum_{L_1,L_2=1}^{N} \sum_{M=-L_<}^{L_<} \frac{(-1)^{L_2} f_{L_1 L_2 M}}{R^{L_1+L_2+1}}(\mathbf{R}) Q_{L_1 M}(\mathbf{r}_{1A}) Q_{L_2 -M}(\mathbf{r}_{2B}), \tag{2.6}$$

where the Q_{LM} is the multipole operator for each atom with electronic coordinate $\mathbf{r}$,

$$Q_{LM} = \left\{ \frac{4\pi}{2L+1} \right\} r^L Y_{LM}(\hat{r}), \tag{2.7}$$

and $f_{L_1 L_2 M}$ is,

$$f_{L_1 L_2 M} = \frac{(L1 + L2)!}{[(L_1 + M)!(L_1 - M)!(L_2 + M)!(L_2 - M)!]}. \tag{2.8}$$

In Eq. 2.6, the monopole terms $L_1 = L_2 = 0$, vanish because the Rydberg atoms are neutral atoms without a net charge. The leading term of the interaction is the dipole-dipole interaction which results in van der Waals and resonant dipole potentials. For dipole-dipole interaction ($\propto R^{-3}$) in Eq. 2.6, we set $L_1 = L_2 = 1$.

$L_1 = L_2 = 2$ corresponds to the quadrupole-quadrupole ($\propto R^{-5}$) interactions. For dipole-quadrupole interactions ($\propto R^{-4}$), one of the variables (L_1 or L_2) is 1, and another one is 2. Eq. 2.6 is only valid when the wavefunctions of the atoms do not overlap. For cases when $r_{2B} > R + r_{1A}$, $r_{1A} > R + r_{2B}$, and $|r_{1A} - r_{2B}| \leq R \leq r_{1A} + r_{2B}$ the interaction potential has different terms [94, 92]. In this thesis, we work with Rydberg atoms separated at distances larger than the Leroy radius where the wavefunctions of the atoms do not overlap; thus, the exchange interaction and autoionization effect are negligible. The Leroy radius is defined as [95],

$$R_{LR} = 2(\langle\psi_1|r_{1A}^2|\psi_1\rangle^{1/2} + \langle\psi_2|r_{2B}^2|\psi_2\rangle^{1/2}) \tag{2.9}$$

where ψ_1 is the wavefunction of the first atom, and ψ_2 belongs to the second atom. For Rb atom in 50s state the $R_{LR} \approx 0.75\,\mu m$.

It is very common for calculations to consider only the dipole-dipole interactions between Rydberg atoms. In our pair-potential calculations, we also consider quadrupole-quadrupole and dipole-quadrupole interactions. The quadrupole interactions are important for understanding the true nature of the interactions between a pair of Rydberg atoms.

2.2.1 Stark effect

The potentials also depend on the magnitude and direction of an applied electric field. Applying a background electric field to the system polarizes the Rydberg

atoms and creates permanent dipole moments in each atom. The background electric field causes the atomic state energies of the Rydberg atoms to be shifted and mixes the field-free states. One advantage of applying a controlled background electric field is the possibility of tuning interaction potentials. As an example, one can create potential wells that can hold many bound states for pairs of Rydberg atoms [96]. Although neglecting electric fields in calculations is quite common, many experiments have a small background electric field. In our pair-potential calculations, the presence of the background electric field is to control and tune the Rydberg-Rydberg interactions. The Stark Hamiltonian for a Rydberg atom in an electric field is defined as,

$$H_s = \mathbf{d} \cdot \mathbf{E}. \tag{2.10}$$

In this equation, only the valence electron is considered for the dipole moment $\mathbf{d}$, to experience the electric field E. The matrix elements of the Stark interaction for dipole transition between states $|l^{'}, j^{'}, m^{'}\rangle$ and $|l, j, m\rangle$ is,

$$\langle W, l, j, m|Ez|W^{'}, l^{'}, j^{'}, m^{'}\rangle = \delta(m_j, m_j^{'})\delta(l, l^{'} \pm 1)\langle W, l|r|W^{'}, l\rangle Ez$$
$$\times \sum_{m_l = m_j \pm 1/2} \langle l, 1/2, m_l, m_j - m_l|j, m_j\rangle\langle l^{'}, 1/2, m_l, m_j - m_l|j, m_j\rangle\langle l, m_l|cos(\theta)|l^{'}, m_l\rangle, \tag{2.11}$$

where j is the total angular momentum, $j = l \pm 1/2$. W and $W^{'}$ are the energy of states $|l, j, m\rangle$ and $|l^{'}, j^{'}, m^{'}\rangle$ respectively. The term containing $\cos(\theta)$ term in

Eq. 2.11 is evaluated as following,

$$\begin{aligned}\langle l, m_l|\cos(\theta)|l-1, m_l\rangle &= \left(\frac{l^2-m^2}{(2l+1)(2l-1)}\right)^{1/2}, \\ \langle l, m_l|\cos(\theta)|l+1, m_l\rangle &= \left(\frac{(l+1)^2-m^2}{(2l+3)(2l+1)}\right)^{1/2}.\end{aligned} \tag{2.12}$$

Equation 2.11 is diagonalized to obtain Strak shifted eigenenergies and eigenfunctions. The Stark shifted eigenvectors and eigenvalues are used to construct the pair state Hamiltonian matrix for pair interaction calculations in an electric field.

2.2.2 Potential curve calculation

For calculating pair-potential curves, the one-atom Hamiltonian is constructed by calculating the energies of the states of interest and nearby states. For this purpose, we use the quantum defect model and write the field-free binding energy using Eq. 2.2. The one-atom Stark Hamiltonian matrix is constructed from the basis of selected atomic states with the field-free energies placed along the diagonal of the matrix. Off-diagonal elements of the matrix represent the electric field coupling terms. This forms the one-atom Stark Hamiltonian matrix as expressed in Eq. 2.11. From Eqs. 2.6, 2.7, and 2.8 the pair state Hamiltonian is defined as [96],

$$\begin{aligned}&\langle\widetilde{\alpha}|\otimes\langle\widetilde{\beta}|H(R)|\widetilde{\alpha'}\rangle\otimes|\widetilde{\beta'}\rangle = \delta_{\alpha\alpha'}\delta_{\beta\beta'}E_{\alpha\beta} \\ &+\langle\widetilde{\alpha}|\otimes\langle\widetilde{\beta}|\Big(\sum_{L_1,L_2=1}^{2}\sum_{m=-L<}^{L<} C_{L_1,L_{2m}}\frac{r_{1A}^{L_1}r_{2B}^{L_2}}{R^{L_1+L_2+1}}Y_{L_1m}^{(1)}Y_{L_2m}^{(2)}\Big)|\widetilde{\alpha'}\rangle\otimes|\widetilde{\beta'}\rangle\,,\end{aligned} \tag{2.13}$$

where $C_{L_1,L_{2m}}$ is,

$$C_{L_1,L_{2m}} = (-1)^{L_2} \frac{4\pi}{[(2L_1+1(2L_2+1))]^{1/2}} \times \frac{(L_1+L_2)!}{[(L_1+m)!(L_1-m)!(L_2+m)!(L_2-m)!]^{1/2}}. \tag{2.14}$$

Equation 2.13 shows the interaction terms that depend on the distance between two atoms R, as R^{-3}, R^{-4}, and R^{-5}. The off-diagonal terms are the sum of the dipole-dipole, dipole-quadrupole, and quadrupole-quadrupole coupling terms, which are specified by a sum over L_1 and L_2. For dipole-dipole interactions $L_1 = L_2 = 1$ while for quadrupole-quadrupole interactions $L_1 = L_2 = 2$. For dipole-quadrupole interactions one of the variables is 1 and other one is 2 [96]. Since the electron clouds of the Rydberg atoms do not overlap, we have the freedom to write the basis states for the Rydberg pairs using independent atom quantum numbers: $|\widetilde{\alpha}\rangle \otimes |\widetilde{\beta}\rangle = |n, l, j, m\rangle \otimes |n', l', j', m'\rangle$. The tilde indicates the eigenfunctions of the Stark Hamiltonian. The asymptotic Stark shifted pair energies is shown by $E_{\alpha\beta} = E_\alpha + E_\beta$. The $\vec{r}_{1A}$ and $\vec{r}_{2B}$ are shown in Fig. 2.5 and represent the distance of the valance electron from the core. Subscripts 1 and 2 are used to distinguish between atom 1 and atom 2 spherical coordinates. By diagonalizing the two-atom Hamiltonian at different internuclear distances R, it is possible to construct a set of potential curves [49, 96].

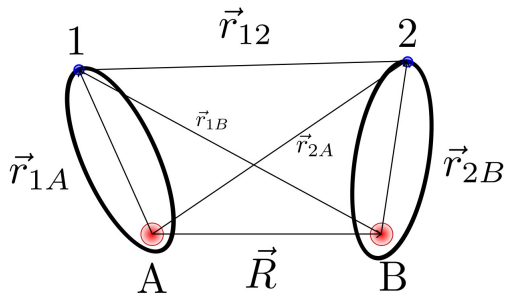

Figure 2.5: Two atoms with nuclei of A and B and two electrons 1 and 2.

2.3 Atom light interaction

This part of the thesis is dedicated to studying the interaction between Rydberg atomic ensemble in a monochromatic laser light where there are more than two atoms in the system. For such many-body systems, we consider two-level atoms and use the density matrix to calculate the response of the interacting Rydberg medium to the applied monochromatic laser light. The interaction between Rydberg atoms in the leading dipole-dipole interaction term in Eq. 2.6, is the van der Waals interaction. The calculations are semiclassical as the laser light is a classical field, and the atoms are treated quantum mechanically.

2.3.1 Two-level atom in laser field

The state of a two-level atom can be expressed by,

$$|\psi^q\rangle = \sum_i a_i^q \, |i\rangle \, . \tag{2.15}$$

Here, a_i^q is the probability of the system to be in state $|i\rangle$ and $\{|i\rangle\}$ are an orthonormal basis set. For the two level atom system $\{|i\rangle\}$ are defined as,

$$|g\rangle = \begin{pmatrix} 1 \\ \\ 0 \end{pmatrix}, \; |r\rangle = \begin{pmatrix} 0 \\ \\ 1 \end{pmatrix}. \tag{2.16}$$

A schematic of a two-level atom in monochromatic laser light is shown in Fig. 2.6. In this figure, the laser radiation frequency is ω. The ground state is $|g\rangle$ with energy $\hbar\omega_g$, and the excited state is $|e\rangle$ with energy $\hbar\omega_e$. The separation between the two states is $\hbar\omega_0 = \hbar\omega_e - \hbar\omega_g$. The spontaneous decay of the excited state (the Rydberg state) is shown by Γ. The electric field of the incident radiation is,

$$\begin{aligned} \mathbf{E}(t) &= \mathbf{E}_0 \cos(\omega t) \\ &= \frac{E_0\,\hat{e}}{2}\,(e^{i\omega t} + e^{-i\omega t}), \end{aligned} \tag{2.17}$$

where $\hat{e}$ shows the polarization direction of the electric field and E_0 is the magnitude of the electric field. Here the direction of the electric field is considered to be parallel to the atomic dipoles. The atom-light Hamiltonian is defined as,

$$H_{LA} = H_{atom} + H_{light}, \tag{2.18}$$

H_{atom} is the atomic Hamiltonian when there is no external field, and H_{light} accounts for the atom-light interaction. H_{LA} can be written as,

$$H_{LA} = \hbar\omega_e \,|e\rangle\,\langle e| + \hbar\omega_g \,|g\rangle\,\langle g| - \langle e|\,\hat{\boldsymbol{\mu}}\cdot\mathbf{E}\,|g\rangle\,|e\rangle\,\langle g| - \langle g|\,\hat{\boldsymbol{\mu}}\cdot\mathbf{E}\,|e\rangle\,|g\rangle\,\langle e|\,, \tag{2.19}$$

where the transition dipole matrix element of the atoms for transition between state i and j is defined as, $\hat{\boldsymbol{\mu}}_{ij} = \langle i| - e\hat{\mathbf{r}}\,|j\rangle$. They represent the transition

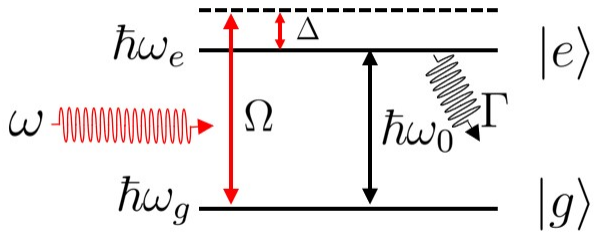

Figure 2.6: Schematic of a two-level system in monochromatic laser light. Γ is the decay rate of the excited state. The ground state $|g\rangle$ with energy $\hbar\omega_g$ is coupled to the excited state $|e\rangle$ with $\hbar\omega_e$ by laser radiation of frequency ω, Rabi frequency Ω, and detuning Δ.

strength between states g and e, $\mathbf{r}$ is the position of the electron, and e is the electron charge. The terms $|g\rangle\langle e|$ and $|e\rangle\langle g|$ are the transition operators, and $|e\rangle\langle e|$, $|g\rangle\langle g|$ are the projection operators. In the case of many atoms in the system, for constructing the density matrix, more general forms of the transition operator, $\sigma^j_{\mu\nu} = |\mu\rangle_{jj}\langle\nu|$, $(\mu \neq \nu)$, or projection operator $(\mu = \nu)$ are used. The index j is to distinguish between different atoms in the system. Using the dipole approximation, provided the electric field does not change rapidly, the coupling between monochromatic laser light and the two atoms is written as $V = -\hat{\boldsymbol{\mu}} \cdot \mathbf{E}$. Substituting Eq. 2.17 into the coupling term V results in,

$$\begin{aligned} V &= -\frac{\hat{\boldsymbol{\mu}} \cdot \hat{e}\, E_0}{2}\,(e^{-i\omega t} + e^{i\omega t}) \\ V_{eg} &= -\frac{\mu_{eg}\, E_0}{2}\,(e^{-i\omega t} + e^{i\omega t}) \\ V_{ge} &= -\frac{\mu_{ge}\, E_0}{2}\,(e^{-i\omega t} + e^{i\omega t}). \end{aligned} \tag{2.20}$$

Writing the coupling in terms of Rabi frequencies $\Omega = -\mathbf{E}\cdot\hat{\boldsymbol{\mu}}\,\hbar^{-1}$, $\Omega_{eg} = E_0 e\hbar^{-1}\langle g|\,r\,|e\rangle$ and $\Omega_{ge} = E_0 e\hbar^{-1}\langle e|\,r\,|g\rangle$, the coupling terms become,

$$\begin{aligned} V &= \frac{\hbar\Omega}{2}\,(e^{-i\omega t} + e^{i\omega t}) \\ V_{eg} &= \frac{\hbar\Omega_{eg}}{2}\,(e^{-i\omega t} + e^{i\omega t}) \\ V_{ge} &= \frac{\hbar\Omega_{ge}}{2}\,(e^{-i\omega t} + e^{i\omega t}). \end{aligned} \tag{2.21}$$

Therefore, from Eqs. 2.19 and 2.21, H_{LA} in matrix form can be constructed as,

$$H_{LA} = \frac{\hbar}{2}\begin{pmatrix} 2\omega_g & \Omega(e^{-i\omega t} + e^{i\omega t}) \\ \Omega(e^{-i\omega t} + e^{i\omega t}) & 2\omega_e \end{pmatrix}. \tag{2.22}$$

We make the calculations more tractable by applying several unitary transformations, such that H_{LA} can become time indipendent [97]. The first unitary transformation $U_1(t)$ is,

$$U_1 = \begin{pmatrix} e^{-i\omega_g t} & 0 \\ 0 & e^{-i\omega_e t} \end{pmatrix}. \tag{2.23}$$

Applying it on the wavefunction in Schrödinger picture gives the wavefunction in the interaction picture, $|\psi_I\rangle = U_1(t)\,|\psi_S\rangle$. The new Hamiltonian in the interaction picture is $H^1_{LA} = i\hbar\frac{dU_1^\dagger}{dt}U_1 + U_1^\dagger H_{LA} U$ [98]. H^1_{LA} in matrix form is,

$$H^1_{LA} = \frac{\hbar}{2}\begin{pmatrix} 0 & \Omega e^{i\Delta t}(e^{-2i\omega t} + 1) \\ \Omega e^{-i\Delta t}(1 + e^{2i\omega t}) & 0 \end{pmatrix}, \tag{2.24}$$

where Δ is the detuning and is defined as $\Delta = \omega - \omega_0 = \omega - (\omega_e - \omega_g)$. Applying another unitary transformation,

$$U_2 = \begin{pmatrix} e^{i\frac{\Delta}{2}t} & 0 \\ 0 & e^{-i\frac{\Delta}{2}t} \end{pmatrix}, \tag{2.25}$$

the time-dependent detuning component of the Hamiltonian is removed. The Hamiltonian becomes,

$$H_{LA}^{2} = \frac{\hbar}{2}\begin{pmatrix} \Delta & \Omega(e^{-2i\omega t}+1) \\ \Omega(1+e^{2i\omega t}) & -\Delta \end{pmatrix}. \tag{2.26}$$

To perform an energy shift, the result of the third unitary transformation,

$$U_3 = \begin{pmatrix} e^{-i\frac{\Delta}{2}t} & 0 \\ 0 & e^{-i\frac{\Delta}{2}t} \end{pmatrix}, \tag{2.27}$$

on the H_{LA}^{2} is,

$$H_{LA}^{3} = \frac{\hbar}{2}\begin{pmatrix} 0 & \Omega(e^{-2i\omega t}+1) \\ \Omega(1+e^{2i\omega t}) & -2\Delta \end{pmatrix}. \tag{2.28}$$

The $e^{-2i\omega t}$ and $e^{2i\omega t}$ are fast rotating terms as they rotate twice as fast compared to the laser frequency. Based on the rotating wave approximation (RWA), these terms are ignored, and the Hamiltonian for a two-level system presented in Fig. 2.6 becomes,

$$H_{LA}^{rwa} = \frac{\hbar}{2}\begin{pmatrix} 0 & \Omega \\ \Omega & -2\Delta \end{pmatrix}. \tag{2.29}$$

2.3.2 Three-level atom in a laser field

A schematic of a three-level atom in a laser field is shown in Fig. 2.7. The three-level atom model is used to explain phenomena such as electromagnetically induced transparency (EIT). The Hamiltonian of a three-level atom in a laser field can be achieved similar to the two-level system as discussed in section 2.3.1.

The atom-light Hamiltonian in Eq. 2.18 can be written for the three-level system in the following form,

$$\begin{aligned} H_{LA} &= \hbar\omega_e \left|e\right\rangle \left\langle e\right| + \hbar\omega_g \left|g\right\rangle \left\langle g\right| + \hbar\omega_r \left|r\right\rangle \left\langle r\right| \\ &- \left\langle e\right| \hat{\boldsymbol{\mu}} \cdot \mathbf{E} \left|g\right\rangle \left|e\right\rangle \left\langle g\right| - \left\langle g\right| \hat{\boldsymbol{\mu}} \cdot \mathbf{E} \left|e\right\rangle \left|g\right\rangle \left\langle e\right| \\ &- \left\langle e\right| \hat{\boldsymbol{\mu}} \cdot \mathbf{E} \left|r\right\rangle \left|e\right\rangle \left\langle r\right| - \left\langle r\right| \hat{\boldsymbol{\mu}} \cdot \mathbf{E} \left|e\right\rangle \left|r\right\rangle \left\langle e\right| . \end{aligned} \tag{2.30}$$

With the relation of the Rabi frequency defined in Eq. 2.31, Ω_p and Ω_c can be written as,

$$\begin{aligned} \Omega_p &= \frac{eE_{0p}}{\hbar} \left\langle e\right| \hat{e} \cdot \mathbf{r} \left|g\right\rangle \\ \Omega_c &= \frac{eE_{0c}}{\hbar} \left\langle r\right| \hat{e} \cdot \mathbf{r} \left|e\right\rangle . \end{aligned} \tag{2.31}$$

In the Hamiltonian given in Eq. 2.30 the excited state $\hbar\omega_e$ and Rydberg state $\hbar\omega_r$ energies can be written relative to the ground state $\hbar\omega_g = 0$. In the three-level atom, after applying dipole approximation, the unitary transformations, and the RWA, the Hamiltonian is written as,

$$H^{rwa}_{3level-LA} = \frac{\hbar}{2} \begin{pmatrix} 0 & \Omega_p & 0 \\ \Omega_p & -2\Delta_p & \Omega_c \\ 0 & \Omega_c & -2(\Delta_p + \Delta_c) \end{pmatrix}, \tag{2.32}$$

where Δ_p and Δ_c are the detunings of the probe and coupling laser from resonance and are defined as,

$$\begin{aligned} \Delta_p &= \omega_p - \omega_e \\ \Delta_c &= \omega_c - (\omega_r - \omega_e) \end{aligned} \tag{2.33}$$

.

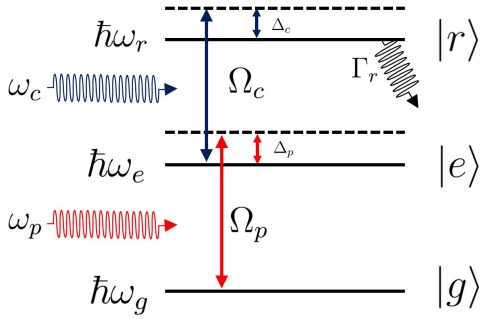

Figure 2.7: Energy level diagram of the three-level system in the presense of two laser fields. This system is used in three-level density matrix and cavity-assisted EIT calculations presented in chapter 5. The energies of the ground state $|g\rangle$, excited state $|e\rangle$, and Rydberg state $|r\rangle$ are $\hbar\omega_g$, $\hbar\omega_e$, and $\hbar\omega_r$, respectively. Δ_p and Δ_c are the detunings of the lasers from the atomic transitions. Decay of the Rydberg state is presented by Γ_r.

2.3.3 Density matrix

To describe statistical concepts in quantum mechanics, the density matrix formalism was first introduced by von Neumann (1927) [99]. Density matrix methods provide a uniform treatment of all quantum mechanical states. In recent years, in modern atomic physics, density matrix techniques have become an important tool for describing the various quantum mechanical phenomena [100]. The calculations in chapters 4 and 5, when the system consists of a few atoms, are based on the many-body density matrix. Usually, the study of the dynamic properties of a system with few atoms is done through the time-dependent

Schrödiner equation, $i\hbar\frac{d}{dt}|\psi\rangle = H_{tot}|\psi\rangle$, where H_{tot} is the total Hamiltonian of the system. However, in atomic systems presented in chapters 4 and 5, due to a dissipative process of spontaneous emission, performing unitary operations on the time-dependent Schrödiner equation is not possible. Therefore, other statistical methods such as stochastic wave-function evolution [101] or density matrix methods can be advantageous. In this thesis, describing the dynamics of the system is done through density matrix calculations. The density matrix is defined as,

$$\rho = \sum_q b(q)\,|\psi^q\rangle\,\langle\psi^q|\,. \tag{2.34}$$

Here, $b(q)$ is the probability of the system to be in pure state q, where the state of the system is,

$$|\psi^q\rangle = \sum_i a_i^q\,|i\rangle\,. \tag{2.35}$$

For a two-level atom system, $|\psi\rangle = a_g|g\rangle + a_r|r\rangle$. The $|i\rangle$s are solutions to the time-independent Schrödinger equation, $\hat{H}_{atom}|i\rangle = E_i|i\rangle$, and form a complete orthonormal basis set $\{|i\rangle\}$. The density operator for pure states two-level system is $\rho = |\psi\rangle\langle\psi|$, or in matrix form,

$$\rho = \begin{pmatrix} \sigma_{gg} & \sigma_{gr} \\ \sigma_{rg} & \sigma_{rr} \end{pmatrix}, \tag{2.36}$$

where $\sigma_{gg} = |g\rangle\langle g|$, $\sigma_{gr} = |g\rangle\langle r|$, $\sigma_{rg} = |r\rangle\langle g|$, and $\sigma_{rr} = |r\rangle\langle r|$. The time evaluation of the system is calculated using the Liouville-von Neumann equation

$$\frac{d}{dt}\rho = \frac{1}{i\hbar}[\hat{H}, \rho]. \tag{2.37}$$

To add the decays of the excited state to the equations, the Lindblad operator is added to the Liouville-von Neumann equation. For a two-level system the Lindblad master equation is,

$$\frac{d}{dt}\rho = \frac{1}{i\hbar}\left[\hat{H}, \rho\right] + \mathcal{L}_{21}(\rho) + \mathcal{L}_{d}(\rho), \tag{2.38}$$

where $\mathcal{L}_{21}(\rho)$ is the decay operator and $\mathcal{L}_{d}(\rho)$ is the dephasing operator due to finite laser linewidth. In general, the decay Lindblad operators can be written as [102],

$$\mathcal{L}(\rho) = -\frac{1}{2}\sum_{n}(C_n^{\dagger}C_n\rho + \rho C_n^{\dagger}C_n - 2C_n\rho C_n^{\dagger}). \tag{2.39}$$

The Lindblad operator represents the loss of population of state $|i\rangle$ due to the spontaneous emission through all decay and dephasing modes [103]. For a two-level Rydberg atom, there is one decay mode, as shown in Fig. 2.6. The decay rate is equal to the e^{-1} finite lifetime of the Rydberg state, τ_r. The decay modes C for a two-level are defined as,

$$C = \sqrt{\Gamma_{gr}}\,|g\rangle\langle r| = \sqrt{\Gamma_{gr}}\sigma_{gr}. \tag{2.40}$$

In general the decay operator of a state $|i\rangle$ is $C_i = \sum_j \Gamma_{ij}\sigma_{ij}$, which is equal to τ_i^{-1}, the e^{-1} lifetime of state $|i\rangle$. The dephasing operator is $\mathcal{L}_d(\rho) = -\sum_{i,j}\gamma_{ij}\rho_{ij}\sigma_{ij}$, where γ_{ij} are summations over linewidth of all laser fields coupling the states $|i\rangle$ and $|j\rangle$.

The solution for the dynamics of a two-level system can be calculated analytically by writing Eq. 2.38 as a set of coupled rate equations called optical

Bloch equations (OBE),

$$\begin{aligned}
\frac{d}{dt}\tilde{\rho}_{11} &= -\Gamma_r\tilde{\rho}_{11} + \frac{i\Omega}{2}(\tilde{\rho}_{21} - \tilde{\rho}_{12}),\\
\frac{d}{dt}\tilde{\rho}_{22} &= \Gamma_r\tilde{\rho}_{11} - \frac{i\Omega}{2}(\tilde{\rho}_{21} - \tilde{\rho}_{12}),\\
\frac{d}{dt}\tilde{\rho}_{12} &= (i\Delta - \frac{\Gamma_r}{2})\tilde{\rho}_{12} - \frac{i\Omega}{2}(\tilde{\rho}_{11} - \tilde{\rho}_{22}).
\end{aligned} \tag{2.41}$$

Γ_r is the decay rate of the Rydberg level and $\tilde{\rho}_{11}$, $\tilde{\rho}_{22}$, and $\tilde{\rho}_{12}$ are new variables. They are defined as,

$$\begin{aligned}
\tilde{\rho}_{11} &= \rho_{11},\\
\tilde{\rho}_{22} &= \rho_{22},\\
\tilde{\rho}_{12} &= e^{i\omega t}\rho_{12},\\
\tilde{\rho}_{21} &= e^{-i\omega t}\rho_{21}.
\end{aligned} \tag{2.42}$$

For the steady state solution, by replacing $\frac{d}{dt}\rho = 0$ in Eq. 2.38, and conservation of the population $\rho_{11} + \rho_{22} = 1$, the result is,

$$\tilde{\rho}_{21} = -\frac{i\Omega/2}{\Gamma_r/2 - i\Delta}(\rho_{11} - \rho_{22}). \tag{2.43}$$

For a multi level system, it is not possible to solve the coupled equations analytically. Therefore, for such systems, a numerical approach is used.

2.3.4 Adiabatic elimination of the intermediate state

In the three-level atom model a large detuning from the intermediate state $|\Delta_p|$ $\gg |\Delta_c|$, $|\Omega_p|$, $|\Omega_c|$, and small decay (Γ_{32}) from $|r\rangle$ to $|e\rangle$ will reduce the population of the intermediate state $|e\rangle$ sinificantly. In such conditions, the intermediate state can be neglected, and the atom can be considered as an effective two-level

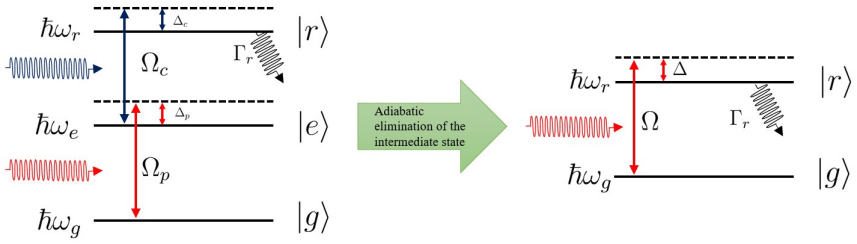

Figure 2.8: Adiabatic elimination of the intermediate level .

atom as shown in Fig. 2.8 [104]. The effective two-level Hamiltonian becomes,

$$H_{eff} = \frac{\hbar}{2}\begin{pmatrix} 0 & \Omega_{eff} \\ \Omega_{eff} & -2\Delta_{eff} \end{pmatrix}, \tag{2.44}$$

where the effective two-photon detuning is,

$$\Delta_{eff} = \Delta_c - \frac{|\Omega_c|^2}{4\Delta_g} + \frac{|\Omega_g|^2}{4\Delta_g}. \tag{2.45}$$

In Eq. 2.44, the two-photon effective Rabi frequency is,

$$\Omega_{eff} = \sqrt{\Omega_{eff}^{res^2} + \Delta_{eff}^2}, \tag{2.46}$$

here Ω_{eff}^{res} is the effective Rabi frequency at resonant and is defined as,

$$\Omega_{eff}^{res} = \frac{\Omega_p \Omega_c}{2\Delta_p}. \tag{2.47}$$

Eliminating the intermediate state $|e\rangle$ adiabatically will result in treating the Lindblad operator along with other components of the system with effective two-level atoms. The calculations presented in chapter 4 are based on two-level atoms. The result of the two-level atoms also can be applied to three-level atoms

where the intermediate state can be eliminated adiabatically. For instance, in systems such as our group's cavity-QED experiment where the probe detuning is larger than the coupling detuning and the two coupling Rabi frequencies, Ω_g and Ω_c, the system can be effectively considered as a two-level system. In this case the above expressions for effective quantities can be used.

2.4 N two-level atom system

The many-body interacting Rydberg ensembles in chapters 4 and 5 consist of an ensemble of N two-level atoms and N three-level atoms, respectively. The laser field resonantly couples the atomic ground state $|g\rangle$ to the highly excited Rydberg state $|r\rangle$ with Rabi frequency Ω, Fig. 2.6. The three atoms in the system are excited into the Rydberg state $|r\rangle$. The interaction between the atoms in the Rydberg state can be expressed as $\Delta_{ij} = \hbar C_p |r_i - r_j|^{-p}$. Terms with $p = 3$ in Δ_{ij} represent dipole-dipole interactions, and terms with $p = 6$ represent the van der Waals interaction. In many-body interacting atoms, the van der Waals interaction potential is used. The pair-wise interaction potential between three Rydberg atoms shown in Fig. 2.9c is defined as $V_{ij} = \hbar \sum_{i<j}^{N} \hat{\sigma}^i_{rr} \Delta_{ij} \hat{\sigma}^j_{rr}$.

The total Hamiltonian of the system is obtained by adding the atom-atom interaction Hamiltonian to the two-level atom-light interaction Hamiltonian for the N atom system, and is defined as, $\hat{H}_T = \hat{H}^{rwa}_{LA} + \hat{H}_{aa}$. In this Hamiltonian, we consider the rotating wave approximation as was discussed in the previous

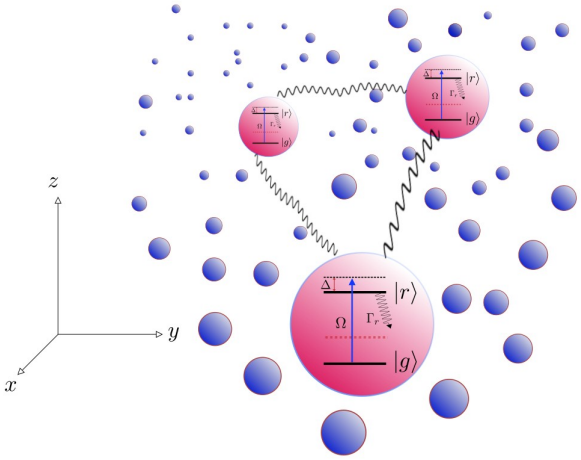

(a) Many-body ensemble

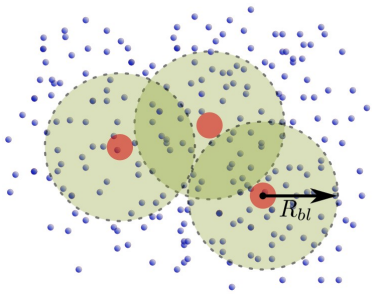

(b) Blockade volume

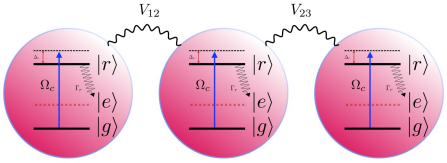

(c) Pairwise interaction between three Rydberg atoms

Figure 2.9: (a) Shows the many-body system, which consists of ground-state atoms (blue spheres) and three excited atoms to the Rydberg state (red spheres). (b) The interaction between the Rydberg state prevents other ground state atoms in the blockaded volume (green circle) from being excited to the Rydberg state. The blockaded volume is $4/3\pi R_{bl}^3$. (c) The pairwise interaction potential between atoms 1 and 2 is $V_{12} = V_{21}$ and between atoms 2 and 3 is $V_{23} = V_{32}$. State $|e\rangle$ is adiabatically eliminated in the calculations.

section 2.3.1. The $\hat{H}_{LA}^{rwa}$ is atom field Hamiltonian, and $\hat{H}_{aa}$ is the interaction between the atoms.

$$\hat{H}_{tot} = \hat{H}_{LA}^{rwa} + \hat{H}_{aa} \tag{2.48}$$

where,

$$\begin{aligned} \hat{H}_{LA}^{rwa} &= -\hbar \sum_{i}^{N} [\Delta \hat{\sigma}_{rg}^{i} \hat{\sigma}_{gr}^{i} + \Omega(\hat{\sigma}_{gr}^{i} + \hat{\sigma}_{rg}^{i})] \\ \hat{H}_{aa} &= \hbar \sum_{i<j}^{N} \hat{\sigma}_{rr} \Delta_{ij} \hat{\sigma}_{rr}. \end{aligned} \tag{2.49}$$

$$\hat{H}_{tot} = -\hbar \sum_{i}^{N} [\Delta \hat{\sigma}_{rg}^{i} \hat{\sigma}_{gr}^{i} + \Omega(\hat{\sigma}_{gr}^{i} + \hat{\sigma}_{rg}^{i})] + \hbar \sum_{i<j}^{N} \hat{\sigma}_{rr} \Delta_{ij} \hat{\sigma}_{rr}. \tag{2.50}$$

The Rydberg atoms spontaneously decay to the ground state with a decay rate of Γ_r. Other non-radiative decay mechanisms such as dephasing due to collisions and Doppler shifts can be included in the calculations. For simplicity, the dephasing effect is not introduced in the calculations of the two-level system presented in chapter 4. The decay was added to the calculation via the Lindblad operator. The Lindblad operator for the radiative decay of two-level many-body system is,

$$\mathcal{L}_{tot}(\rho) = \sum_{i}^{N} \mathcal{L}^{i}(\rho) = \sum_{i}^{N} \frac{1}{2} \Gamma_{r}^{i} [2\hat{\sigma}_{gr}^{i} \hat{\rho} \hat{\sigma}_{gr}^{i} - (\hat{\sigma}_{rr}^{i} \hat{\rho} + \hat{\sigma}_{rr}^{i} \hat{\rho})]. \tag{2.51}$$

The many-body interaction Hamiltonian in the Lindblad master equation is used to study the system dynamics of several interacting Rydberg atoms.

Chapter 3

Pair potential calculations

3.1 Introduction

This chapter presents the study of the interaction between a pair of Rydberg atoms in the presence of the background electric field. The pair-potential curves for two interacting Rydberg atoms are theoretically calculated. In the calculation, the interacting Rydberg atoms are Rubidium atoms in the $50S_{1/2}$ quantum states in the blockade regime, R_{bl} $4-6$ μm. The range of internuclear distances is varied from 0.5 to 10 μm while applying several backgrounds DC electric fields.

We use calculations of Rydberg atom potential energy curves and surfaces to explain results obtained in [54] quantitatively. In [54], it was shown that one can enhance or suppress the blockade effect in a quasi one dimensional sample of Rubidium atoms by tilting an electric field by an angle θ, with respect to the axis of the sample, Fig. 3.1. Tilting the electric field with respect to the trap axis can change the orientation of the electric field induced dipoles in the one dimensional sample of Rydberg atoms, hence changing the strength of the interactions along the axis of the trap [105]. We performed a series of pair potential calculations for the case of the $50S_{1/2} + 50S_{1/2}$ Rubidium Rydberg atom pair state. Single-atom Stark calculations [106, 107] were used in the original work to estimate the dipole-dipole interaction coefficient C_3 arising

from the electric field induced dipoles. The C_6 coefficient was obtained using a perturbative calculation. The results of this theoretical approach lead to a C_3 that deviated from the experimental results by a factor exceeding seven [54]. Our calculations, which take into account the leading multi-pole interactions between Rydberg atoms and applied electric field, show better agreement with the experiment. Our C_3 coefficient is greater than the asymptotic calculation and differs by only 20% from the one obtained by fitting the experimental data, which is within experimental error for this type of measurement. Besides, our C_6 coefficient is larger and in better agreement with the experimental values, differing only by $\sim 8\%$ rather than $\sim 17\%$.

Our results demonstrate that the C_6 and C_3 coefficients are not independent of one another and the asymptotic approximation, traditionally used to calculate long range potentials for ground state atoms, is frequently invalid for Rydberg atoms over the most critical internuclear separations. A straightforward way to see the interdependence is to notice that as the two atoms approach each other, the van der Waals interaction hybridizes the atoms orbitals, which changes the polarizability of each atom as R changes, resulting in what is effectively an R-dependent electric field induced dipole-dipole potential. The dipole-dipole potential that would result from two otherwise non-interacting Rydberg atoms is not the same as when the atoms are interacting via another strong multipolar interaction. Practically, this means that one must exercise care when using asymptotic polarizabilities to directly determine the C_3 coefficient resulting from

electric field induced atomic dipoles. In such cases, matrix diagonalization, rather than perturbation theory, is generally required to calculate Rydberg atom interactions accurately.

3.1.1 1D blockade experiment

In the experiment, the sample consists of a tightly confined atomic sample that is held in a quasi-electrostatic trap (QUEST). The QUEST is created by a linear polarized 10.6 μm CO_2 laser. The power of the CO_2 laser was 80 W. The QUEST produced a non-polarized, approximately 1D atomic sample, Fig. 3.1, with $\sim 10^6$ atoms at a peak density of $\approx 10^{12}$ cm^{-3} and a temperature of 60 μK. To load the trap, the CO_2 laser was focused on a magneto-optical trap. The CO_2 beam waist is 15 μm [54]. Rydberg atoms are excited using a 2-photon process consisting of the absorption of a 780 nm photon and a tunable photon at $\sim$ 480 nm. The $50S_{1/2}$ state excitation is performed by a laser pulse train and is detected by pulsed-field ionization. The laser pulse train operates at 100 Hz for 1.5 s and is composed of two narrow-bandwidth quasi-continuous wave laser pulses near 780 and 480 nm, whose duration is about 1 μs. The lasers have intensities of $I_{780} = 1.6$ mW cm^{-2} and $I_{480} = 100$ W cm^{-2} corresponding to a Rabi frequency of 32 MHz for each laser. The electric field is generated by a system of eight independently controlled electrodes, which are distributed in two sets of aligned cloverleaves. This system allows the control of the most important experimental parameter, the angle between the QUEST axis and a constant

external electric field applied to the atomic sample, θ in Fig. 3.1. During the Rydberg excitation and detection, the QUEST is turned off for 15 μs to avoid any unwanted effects such as ac Stark shifts or photoionization. The QUEST decay allows us to study the $50S_{1/2}$ Rydberg state population as a function of the ground state atomic density, which is measured by the state-selective absorption imaging technique. The background electric field is estimated to be < 20 mV cm^{-1}. A boxcar gate is used to selectively detect the $50S_{1/2}$ atoms as a function of the ground state atomic density. This information, along with the excitation laser intensities, is used to find the average internuclear distance between Rydberg atoms, ~ 4 to 6 μm, and ground state atoms. More details of the experimental setup can be found in [54, 108, 109]. The first step of the experiment was to obtain a Stark shift spectrum at the highest achievable density in order to find the electric field strength at which the dipole-dipole and van der Waals interactions are comparable (Fig. 1(b) in [54]) 2370 mV cm^{-1}. To experimentally determine the interaction potentials between the $50S_{1/2}$ Rydberg atoms, the population of the initially excited state was measured as a function of ground state atomic density for several θ at an electric field amplitude of 2370 mV cm^{-1}, at a single atom excitation laser detuning of $\Delta_{480} = -151$ MHz (Fig. 2 in [54]). The experimental results clearly show that the blockade effect depends on θ. The work also showed that the measurement performed at the magic angle is very similar to the measurement performed at zero fields, suggesting an electric field induced dipole-dipole interaction and the one dimensional character

of the atomic sample are important to interpret the results.

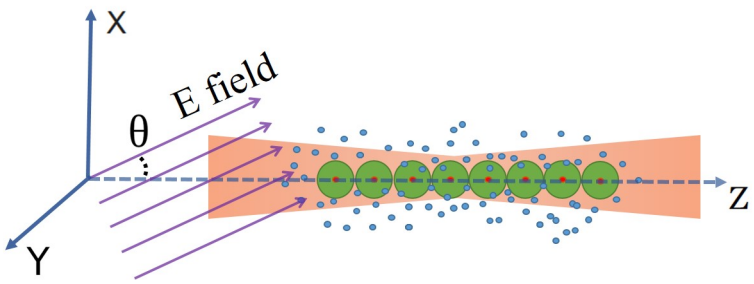

Figure 3.1: One dimensional trapped atomic sample in an electric field. The figure illustrates the one dimensional distribution of super atoms excited due to the Rydberg atom blockade along the dipole trap axis. The figure defines the tilt angle of the electric field relative to the trap axis θ.

3.1.2 Classical hard sphere model

We used the hard-sphere model in our calculations to account for the Rydberg blockade sphere and relate the experimental results to the theory. The blockade sphere is the volume around an excited Rydberg state in which no other ground-state atom can be excited to the Rydberg state as shown in Fig. 3.2. We considered the excitation volumes as a group of densely packed hard spheres. Therefore, the hard-sphere dynamics depend on the Rydberg atom population density ρ_{Ryd}, and ground-state population ρ_g. To study the dynamics, we can write a first-order differential equation as [110],

$$\dot{\rho}_{Ryd} = A\mathcal{V}\rho_g - B\rho_{Ryd} \tag{3.1}$$

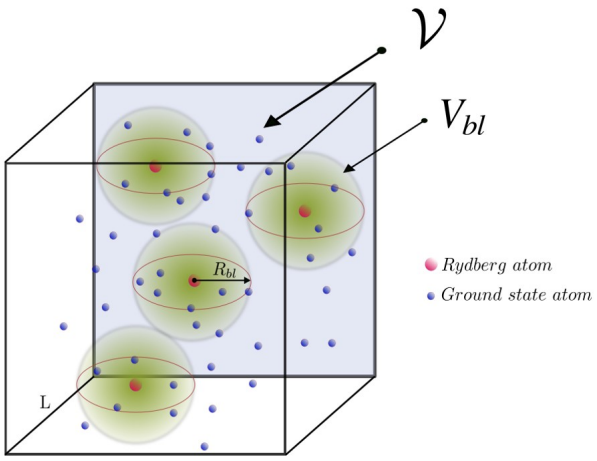

Figure 3.2: The Rydberg atomic ensemble. The blue spheres are the ground-state atoms. The red spheres are the Rydberg atoms, and the volume around them indicated with green color is the blockade volume. The available fractional number for the third Rydberg blockade sphere is $0 < \mathcal{V} < 1$.

where ρ is the total density. A and B are the excitation and de-excitation rates. $\mathcal{V}$ is the fractional available volume. We can set $A = B$ when dealing with systems that consist of two-level atoms with a small loss. $\mathcal{V}$ is the fraction of the total volume available for placing the following blockade spheres in the ensemble. $\mathcal{V}$ is a number between 0 and 1. When $\mathcal{V} = 1$, the volume is empty of blockade spheres, and the whole $V_{bl} = \frac{4}{3}\pi R_{bl}^3$ is available to the center of the subsequent blockade sphere. When $\mathcal{V} = 0$, the hard spheres are densely packed in the ensemble, and there is no volume available for adding another V_{bl}. If we consider that each Rydberg atom in the sample subtracts a V_{bl} from the total volume, we can write $\mathcal{V} = (1 - \rho_{Ryd} V_{bl})$. The steady-state solution of Eq. 3.1 by

using $\rho_g = \rho - \rho_{Ryd}$ results in the following expression for the ρ_{Ryd},

$$\rho_{Ryd} = \frac{2 + V_{bl}\rho - \sqrt{4 + (V_{bl}\rho)^2}}{2V_{bl}}. \tag{3.2}$$

We use this expression in order to find the Rydberg density in our calculations. When the magnitude of the interaction potential is comparable to the laser linewidth, we can relate the two and find the blockade radius, which results in finding the blockade volume, V_{bl}. Using the results of the measurements in [54], C_3 and C_6 coefficients were extracted. Using the $50S_{1/2}$ Rubidium Rydberg state population measured as a function of ground state atomic density for several θ, a classical hard-sphere model in the steady state was applied [111, 112] to determine C_3 and C_6. As it was discussed in section 3.1.2 this model treats Rydberg atoms as hard spheres with a radius equal to the blockade radius R_{bl}, thereby defining an exclusion volume around each excited atom. The excitation volume is assumed to be densely packed by these spheres, so that information about the excited state population is obtained. The blockade radius is an important parameter in such a model, and it can be obtained by imposing the condition that laser bandwidth $\delta\nu$, matches the effective potential at the interatomic distance R_{bl}, which is angle dependent. R_{bl} is used to obtain the blockade volume V_{bl}, where, $\mathrm{V}_{bl} = \frac{4\pi}{3}R_{bl}^3$. Using Eq. 3.2 and the effective potential expression, when it is equal to the laser bandwidth, allows us to obtain the

Rydberg density, which is given by:

$$\frac{\rho_{Ryd}(\theta)}{\rho} = \frac{3 - \frac{3}{2}\sqrt{\frac{4}{9}\pi^2\rho^2(\sqrt{4C_6 + C_3^2P(\theta)^2} + C_3P(\theta))^2 + 4}}{2\pi\rho(\sqrt{4C_6 + C_3^2P(\theta)^2} + C_3P(\theta))} + \frac{1}{2} \tag{3.3}$$

where,

$$P(\theta) = 1 - 3\cos^2(\theta) \tag{3.4}$$

is the P_2 Legendre polynomial. ρ is the ground state density, and $\rho_{Ryd}(\theta)$ is the angle dependent Rydberg density. Under these conditions, the experiment determined $C_6^{exp} = 18418$ MHz μm^6 and $C_3^{exp} = 99.74$ MHz μm^3. The van der Waals interaction parameter C_6, is close to the theoretical one for the $50S_{1/2}$ state, $C_6^{ST} = 15296$ MHz μm^6 which was obtained perturbatively [113]. However, the dipole-dipole interaction parameter is seven times larger than the theoretical one $C_3^{ST} = 14.375$ MHz μm^3, obtained from a single-atom Stark calculation. The discrepancy is due to the fact that these methods of calculation do not fully explain the complex nature of the interaction between two Rydberg atoms. Because high angular momentum states are energetically nearby, ($l_{max} = n - 1$), the multilevel character of the interaction needs to be included to obtain accurate potential curves [54, 109]. The multitude of quasi-resonant interactions makes the asymptotic calculation of the interaction invalid over a large and relevant range of internuclear separations, particularly near the blockade radius. The interaction of many levels changes the polarizability of the atoms as a function of R, making the electric field induced dipole-dipole interaction different from

what it would be if the asymptotic polarizabilities were used to calculate its magnitude.

3.1.3 Theory work

To achieve control over Rydberg atom blockade, the induced atomic dipole moments orientation was changed in [54] by changing the external DC electric field relative to the long axis of the trap θ. In the presence of an external electric field, the interaction potential changes to an angular dependent potential because the atoms become polarized [54, 105]. The potentials corresponding to individual magnetic sub-levels are also angularly dependent. However, if there is no field to provide an orientation in space there is no angular dependence, as there exists an isotropic, degenerate superposition of magnetic sub-levels. The orientational field can be supplied by a continuous field, as primarily addressed in this work, a laser through its polarization, or by other interactions in the molecular frame. In this work, we investigate asymptotic S-states, which are described approximately by isotropic van der Waals potentials when the atoms are far apart. Intuitively, under the experimental conditions, the interaction potential consists of two pieces, the van der Waals and the dipole-dipole potentials. The effective interaction potential adopting this approximation can be written as follows,

$$V_{eff}(R,\theta) = \frac{C_6}{R^6} + \frac{C_3}{R^3}[1 - 3\cos^2(\theta)]. \tag{3.5}$$

In this equation, C_3 is the dipole-dipole interaction parameter, resulting from

the polarization of the atoms in the external electric field, and C_6 is the van der Waals coefficient. The dipole-dipole potential in the present case can be written as a semi-classical expression,

$$V(R) = \frac{\mu^2}{4\pi\epsilon_0 R^3}[\cos(\theta_{12}) - 3\cos(\theta_1)\cos(\theta_2)]. \tag{3.6}$$

μ is the electric field induced permanent dipole of the atoms, which we assume to be in the same atomic state. θ_{12} is the angle between two dipoles, and θ_1 (θ_2) is the angle between the dipole of atom 1 (atom 2) and the internuclear axis. Since the permanent dipoles are produced as a result of an external electric field and our sample in the experiment is a quasi one dimensional sample, the dipole orientations are always in the direction of the external electric field. Thus, θ_{12} is always zero and $\theta_1 = \theta_2$. The simplified version of Eq. 3.6 can be written as,

$$V(R) = \frac{\mu^2}{4\pi\epsilon_0 R^3}[1 - 3\cos^2(\theta)]. \tag{3.7}$$

The prefactor in this expression is the C_3 coefficient. The angular dependence in the potential energy is given by θ.

These expressions are an intuitive way to think about what is happening in the experiment. In fact, we later show by calculating the potential energies according to the method found in Ref. [49] that the dominant interactions are a field induced dipole-dipole interaction and a van der Waals interaction. Consistent with the experiment, these interactions magnitudes, particularly the electric field induced dipole-dipole interaction cannot be accurately calculated

without considering both interactions simultaneously, i.e., these interactions are not independent of each other and should be diagonalized together. The issue with using these expressions to calculate the angular dependence of the interactions can be understood if we write down an expression for C_3,

$$C_3 = \frac{e^2 a_0^2}{4\pi\epsilon_0} \quad \langle 50\widetilde{S_{1/2}50}S_{1/2}|r_1|50\widetilde{S_{1/2}50}S_{1/2}\rangle \times \quad \langle 50\widetilde{S_{1/2}50}S_{1/2}|r_2|50\widetilde{S_{1/2}50}S_{1/2}\rangle \,. \tag{3.8}$$

Here, $\langle 50\widetilde{S_{1/2}50}S_{1/2}|r_1|50\widetilde{S_{1/2}50}S_{1/2}\rangle$ is the dipole moment of atom one in an external electric field while the same expression with r_2 gives the dipole moment of the second atom. In the dipole moment expressions, r_1 only acts on electron 1 and r_2 acts on electron 2. e is the electron charge and a_0 is the Bohr radius. Here we take the most plausible approach of using the molecular wavefunction in the background electric field, indicated by the tilde and the relevant Rydberg pair state $50S_{1/2} + 50S_{1/2}$ [49]. However, the problem with the expression is that it is clearly dependent on R due to the van der Waals interaction. Although this is a straightforward argument, it effectively illustrates why calculating the dipole moments individually using the asymptotic atomic states can result in a poor approximation to the angular dependent interaction potentials. Based on the experimental work, we performed a series of pair-potential calculations for Rubidium in the $50S_{1/2} + 50S_{1/2}$ quantum state for various electric field angels θ. By simultaneously considering multipolar interaction terms up to the quadrupole between Rydberg atoms, we have found a more accurate result for

the dipole-dipole coefficient C_3, and van der Waals coefficient C_6, by fitting our results to the model potential. These fits demonstrate that qualitatively the interaction studied in the experiment is dominated by the isotropic van der Waals and anisotropic electric field induced dipole-dipole potentials. Quantitatively, the fitted C_6 and C_3 agreed with the experimental results much more closely than the original estimates based on the asymptotic atomic wavefunctions. We use the effective C_3 and C_6 to compare to the experimental data since the model potential yields a more intuitive picture than the full calculated potential. The calculated potential can also be related to the experiment by calculating the blockade radius at each angle, but it is not quantitatively different from the model potential in this particular case.

When the electric field is held at zero, the Rydberg atoms do not have permanent dipoles, and the interaction between Rydberg atoms at the blockade radius is predominantly a van der Waals interaction. Fig. 3.3 shows the potential curves along with the population of the $50S_{1/2} + 50S_{1/2}$ quantum state for internuclear distances $R = 3\,\mu$m to $R = 6\,\mu$m. The potential in Fig. 3.3 is weakly repulsive in zero electric field. For the electric field used in the experiment, there are substantial changes to the interaction potentials as shown in Fig. 3.4. Most notably, the strength of the $50S_{1/2} + 50S_{1/2}$ potential changes in an electric field of $2370\,\mathrm{mV\,cm^{-1}}$. We first kept θ fixed at zero degrees and examined the interaction potential for different internuclear distances. The result of the pair potential calculations for an electric field of $2370\,\mathrm{mV\,cm^{-1}}$ for $\theta = 0$ is shown

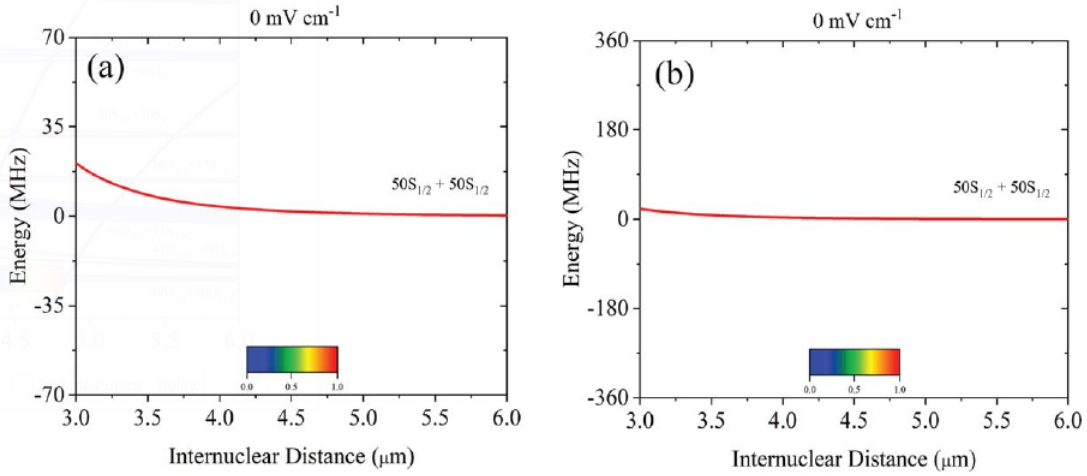

Figure 3.3: Interaction potential curve of the $50S_{1/2} + 50S_{1/2}$ in zero electric field. Here the source of interactions is mainly of the van der Waals type. The population of $50S_{1/2} + 50S_{1/2}$ is large for distances larger than 1.5 μm. The magnitude of the $50S_{1/2}$ component is shown for comparison with the potentials at 2370 mV cm^{-1}. The color indicates the fraction of $50S_{1/2} + 50S_{1/2}$ in the state. As can be observed in the plot, the state is almost entirely $50S_{1/2} + 50S_{1/2}$. (a) shows the potential on a scale where the curvature is evident. (b) shows the potential on the same scale as Fig. 3.4 illustrating the fact that in small electric fields the curve is energetically isolated. Consequently, the curve is predominantly $50S_{1/2} + 50S_{1/2}$ character, corresponding to the red color in the plot.

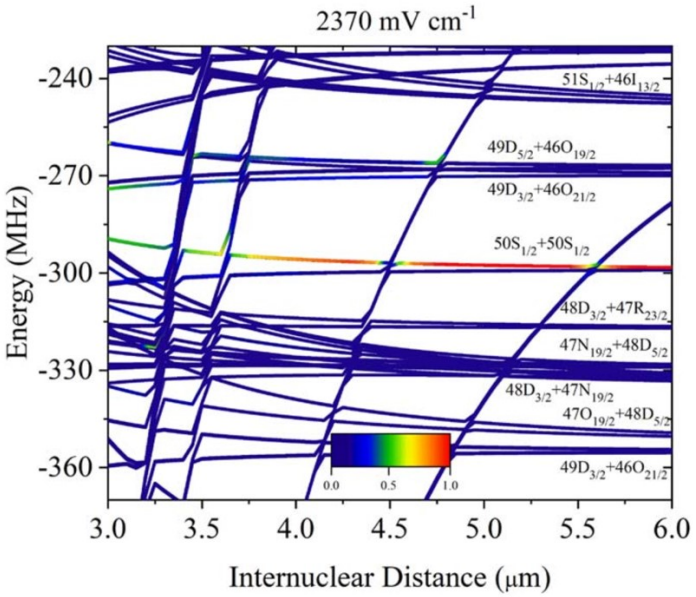

Figure 3.4: Pair potential for $50S_{1/2} + 50S_{1/2}$ in an electric field of $2370\,\mathrm{mV\,cm^{-1}}$ for $\theta = 0\,$degrees. The darker red color shows higher $50S_{1/2} + 50S_{1/2}$ population for different internuclear distances for a constant electric field. The potential energy curves shown in the figure are very different from those with 0 applied electric field because the Stark effect causes some of the n=47 (n is the principal quantum number) Stark manifold states to intersect the $50S_{1/2} + 50S_{1/2}$ curves. This is essentially why the electric field induced dipole-dipole interaction is stronger than first calculated. The interplay between the electric field and the Rydberg atom interactions is complicated because it is highly multilevel in nature for this particular case. The zero of the energy scale is set at the field free $50S_{1/2}+50S_{1/2}$ asymptote.

in Fig. 3.4. We also calculated the amplitude of $50S_{1/2} + 50S_{1/2}$ as a function of internuclear distance for a background electric field of $2370\,\mathrm{mV\,cm^{-1}}$. The amplitude allowed us to verify the potential that was excited in the experiment. We calculated the population by first obtaining the asymptotic wavefunctions for the state of interest $50S_{1/2} + 50S_{1/2}$, and nearby states. When the atoms are interacting, the wavefunction of the system can be written as a superposition of asymptotic atom pair wavefunctions,

$$|50\widetilde{S_{1/2}50}S_{1/2}\rangle = \alpha(R)|50S_{1/2}50S_{1/2}\rangle + \sum_{n,l,n',l'} \beta_{n,l,n',l'}(R)\,|nl\,n'l'\rangle\,. \tag{3.9}$$

$|50\widetilde{S_{1/2}50}S_{1/2}\rangle$ consists of mixture of all states that have interactions with $50S_{1/2} + 50S_{1/2}$ or are coupled by the external electric field. We calculate the probability amplitude of $50S_{1/2} + 50S_{1/2}$ using $\langle 50S_{1/2}50S_{1/2}|50\widetilde{S_{1/2}50}S_{1/2}\rangle$ for each internuclear distance, R. $|50\widetilde{S_{1/2}50}S_{1/2}\rangle$ is the state that carries mostly $50S_{1/2} + 50S_{1/2}$ character, which is shown in red in Fig. 3.4. The higher shading of the red color shows a larger component of $50S_{1/2}+50S_{1/2}$. The mixing between $50S_{1/2} + 50S_{1/2}$ and neighboring states can be seen as the internuclear distance between the Rydberg atoms changes. Fig. 3.4 is more complicated than Fig. 3.3 because the electric field that polarizes the atoms is large enough so that the nearby n=47 Stark manifold is driven into the $50S_{1/2} + 50S_{1/2}$ state. The fact that the state of interest interacts with high angular momentum states results in larger polarizability and, therefore, a larger electric field induced dipole-dipole in-

teraction. In Fig. 3.4 the interaction is dominated by the dipole-dipole potential since it is much stronger at $\theta = 0$ than the van der Waals contribution.

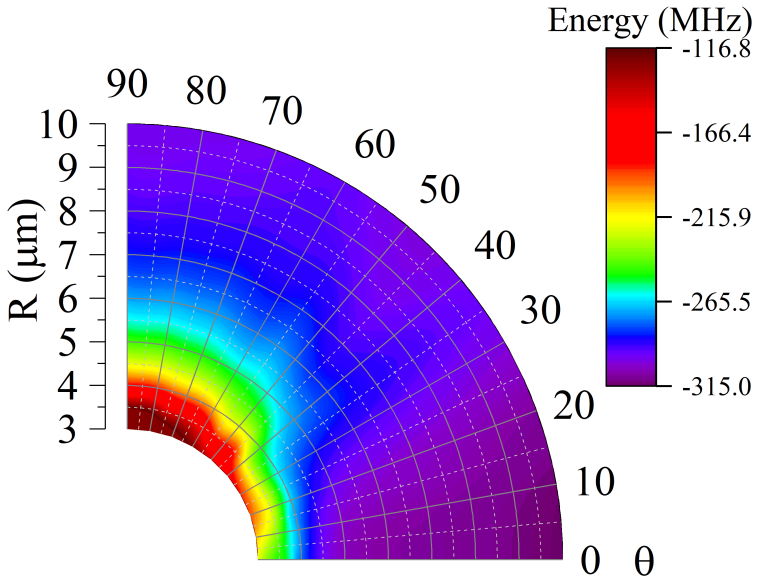

Figure 3.5: Tilting the electric field direction changes the potential energy surface of the interacting Rydberg atoms each in the $50S_{1/2}$ state at an electric field of $2380\,\mathrm{mV\,cm^{-1}}$. By changing the direction of the electric field, the magnitude of the $\cos(\theta)$ term in V_{eff} changes. Both the van der Waals and dipole-dipole parts of the potential energy surface are shown. Zero energy is chosen to correspond to the zero electric field $50S_{1/2} + 50S_{1/2}$ asymptote.

Performing anisotropic calculations for various background electric field θ enables us to study the angular dependence of the dipole-dipole interaction while taking account of the van der Waals interaction. The interaction between

the two Rydberg atoms is seen to depend on the direction of the applied background electric field in Fig. 3.5. The plot shows the full interaction potential, including both the dipole-dipole and van der Waals contribution of $50S_{1/2}+50S_{1/2}$ Rubidium Rydberg atoms in an electric field of $2380\,\mathrm{mV\,cm^{-1}}$. Calculating the potential at the magic angle which satisfies the $P_2(\cos\theta) = 0$, where the P_2 is the Legendre polynomial of second order, results in an interaction potential that just contains the van der Waals potential, $\theta = 54.7^{\circ}$. Subtracting the van der Waals potential from the full potential leaves the dipole-dipole interaction potential. The van der Waals potential model is isotropic and approximated as a pure S-state. The dipole-dipole interaction described here is diagonal, i.e., the dipole-dipole interaction does not couple atoms in different states, becuase they are 'static' dipoles formed by the polarization induced by the external electric field in our approximation. The potentials were fitted in the region between $3\,\mu$m to $6\,\mu$m because this region spanned the blockade radius, Fig. 3.4.

Fig. 3.6 shows the magnitude of the static dipole-dipole interaction potentials for $R = 4.2\,\mu$m for various angles. This figure demonstrates that the remaining interaction potential is well characterized as a dipole-dipole interaction around the blockade radius as argued. Changing the orientation or magnitude of the constant external electric field changes the interaction strength between the Rydberg atoms. For example, in Fig. 3.5, when θ is zero, we have maximum attraction between the two induced dipoles, because the opposite charges of the dipoles are closer to each other. Changing the orientation of the external electric

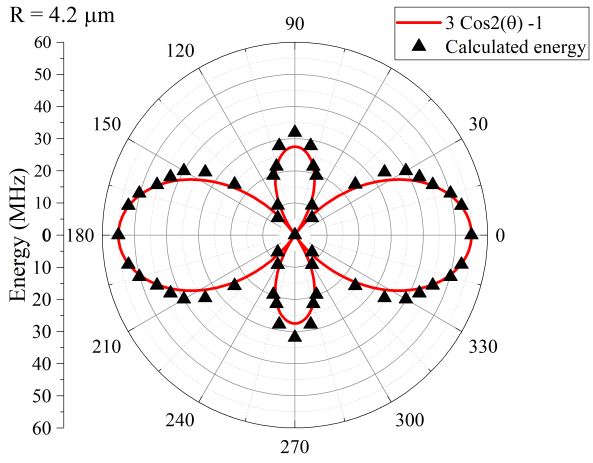

Figure 3.6: The magnitude of the dipole-dipole interaction part of the potential energy at 4.2 μm for an electric field of 2380 mV cm^{-1}. The diagram shows that the angular dependence of the potential energy surface is well-represented by a dipole-dipole interaction. The potential is attractive along $\theta = 0$ degrees and repulsive along $\theta = 90$ degrees.

field to $\theta = 90^o$ will result in maximum repulsion between the two dipoles, since the orientation of induced dipoles are perpendicular to the internuclear axis which causes like charged poles of the dipoles to be closer to each other. The effect is also observed in Fig. 3.5 where the potential is slightly attractive along $\theta = 0$ degrees but is repulsive at short range and more strongly repulsive along $\theta = 90$ degrees.

If we use the full potential calculations to obtain the C_3 coefficient around the blockade radius, $R = 3 - 6\,\mu$m, by fitting the model potential to the

calculations shown in Fig. 3.4 and Fig. 3.5, we obtain $C_3 \sim 120\,\mathrm{MHz}\,\mu\mathrm{m}^3$, which is in reasonable agreement with the experiment, given the prior estimates found in Ref. [54]. The theoretical value for C_3 is approximately 20% different from the experimentally obtained result of $C_3^{exp} = 99.7\,\mathrm{MHz}\,\mu\mathrm{m}^3$. The value obtained by single-atom Stark calculations for C_3 is $14.375\,\mathrm{MHz}\,\mu\mathrm{m}^3$, which is approximately seven times smaller than the experimental value. The C_6 coefficient is also obtained by fitting the calculated potential to the model potential in Fig. 3.4. Using our method the van der Waals coefficient is found to be $C_6 \sim 19970\,\mathrm{MHz}\,\mu\mathrm{m}^6$ which is in better agreement with the experimental value than the estimates in Ref. [54]. The reason that C_3 is larger than estimated is due to the fact that the applied electric field in the experiment is large enough to shift the $50S_{1/2} + 50S_{1/2}$ state into the nearby n=47 Stark manifold. The mixing with the high angular momentum states is important and demonstrates the multilevel nature of the interatomic forces near the blockade radius in this case, consistent with the experiment.

Fig. 3.7 shows the number of $50S_{1/2}$ atoms per ground state atom as well as the blockade radius as a function of θ. The fit to the hard sphere model that was used to extract C_6^{exp} and C_3^{exp} is also shown in Fig. 3.7 as is the graph of the hard sphere model based on our calculation of the electric field dependent interaction potential. Fig. 3.7 is showing the relationship between the experimental data and calculations. In this figure the Rydberg density obtained using the hard sphere

model, Eq. 3.3. Although the hard sphere model assumes a repulsive potential, we use it for our analysis even at $\theta = 0$ degrees where the potential becomes slightly attractive. The attractive part of the potential is < 1 MHz, which is the linewidth of the lasers. The blockade radius changes from $4\,\mu$m to $6\,\mu$m as θ sweeps from 0 to 90 degrees. There are around $\sim 250 - 1000$ ground state atoms in a blockade volume. At $\theta = 0$ degrees, where the dipoles are aligned head to tail, the blockade radius is at a minimum since the dipole-dipole potential is attractive while the van der Waals potential is repulsive. When $\theta = 90$ degrees, the potentials have the same sign and the blockade radius increases.

Fig. 3.7 shows that the angular dependence of the actual potential is well described by the calculational approach of Ref. [49]. The application of the electric field to polarize the atoms clearly has an effect on the blockade radius, it is changed by $\pm 20\%$ when θ changes from 0 to 90 degrees. The theory curve in Fig. 3.7 actually reproduces the data as well as the least squares fit over the extent of the range of θ if the clear systematic error in the experiment is taken into account. The clear outlying point at 15 degrees probably has perturbed the least squares fit enough to shift the curve. The theory curve that we have calculated here, shown in Fig. 3.7, has no adjustable parameters. Only our fit of the calculation and the experimentally measured density are needed to calculate the curve. Although the fit of V_{eff} and our calculation fit the data well, discrepancies between the data and experiment could arise because we are using a limited model to calculate the curves in Fig. 3.7. There are still higher order

interactions and state mixing, so the splitting of the potential into one with dipolar angular dependence and an isotropic piece is not exact. The benefit of the simple picture presented in this thesis outweighs the value of rigorously or semi-rigorously modifying V_{eff}. Including higher orders of interaction complicates the form of the interaction potentials. The experimental data and the degree to which it agrees with our approximation justifies our approach.

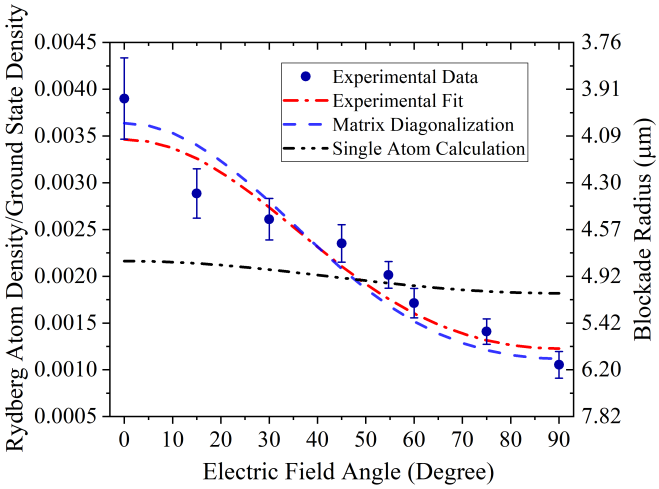

Figure 3.7: This figure shows the number of Rydberg atoms per ground state atom that are excited at different electric field angles θ. The points are the data from Ref. [54]. The red dot-dashed line shows the fit from which C_3 and C_6 were obtained from the experimental data using a nonlinear least squares fit. The blue dashed line shows the results of the calculation presented in the paper. There are no fitting parameters used to plot the blue dashed line, only the experimental measured density is used for the plot. The black dot-dot-dashed line is the estimated theoretical result presented originally in Ref. [54]. The agreement between the experimental results and the full atom-pair calculation is similar to the nonlinear least squares fit of the experimental data. The right hand y-axis labels shows how the blockade radius changes as a function of θ based on the assumption that the peak ground state density is $10^{12}\,\mathrm{cm}^{-3}$. It is a straightforward nonlinear scaling based on how many ground state atoms fit into a blockade sphere at uniform density.

Chapter 4

Many body Rydberg interaction

One of the critical research areas in physics is the control of many-body quantum systems. To achieve such control, the study of the interaction between microscopic components of a many-body quantum system is particularly important. Several systems can fulfill the goal of studying such interactions. For instance, one form of interaction studied in an ultra-cold atomic system is a short-range contact interaction. This type of interaction can be adjusted via Feshbach resonances [114]. In the previous chapter, the study of the interaction between a pair of Rydberg atoms in the presence of the background electric field and Rydberg blockade phenomena was presented. The Rydberg atoms are a very versatile basis for the study of the interaction in many-body quantum systems [1]. The interaction between atoms excited to the Rydberg states can form the Rydberg blockade [53]. Rydberg blockade has been an essential source in many other Rydberg fields, such as information processing with Rydberg atoms [17, 16, 19], scalable quantum computation [115], and quantum error correction [116]. This chapter presents the interaction between many atoms in a Rydberg blockaded ensemble for different atomic densities. This section studies the effect of changing interatomic interaction strength for such systems. Changing the system parameters, such as increasing the density of atoms in the ensemble, results in higher interaction strength between the atoms excited

into the Rydberg state. Increasing the interaction strength causes a transitions between phases of the system from two-body interacting to many-body collective phase.

4.1 Rydberg blockade, super atom and collective effect

As discussed in chapters 2 and 3, one of the outcomes of the distance-dependent interactions between atoms in Rydberg states is the Rydberg excitation blockade. Fig. 4.1 illustrates the blockade mechanism. The interaction shifts doubly excited states out of resonance with the excitation light and limits the population of the excited Rydberg state. The two excited Rydberg states can not appear at internuclear separation less than the blockade radius R_{bl}, and the excitation to the Rydberg state is suppressed in this region. This chapter studies the many-body effects appearing in a cloud of atoms that are coherently excited to a Rydberg state. The system is a two-level system consisting of ground and excited Rydberg state. The Hamiltonian of the system is a many-body interacting Hamiltonian introduced in chapter 2 (Eq. 2.50). The system dynamics are studied via the Lindblad master equation (Eq. 2.38) with many-body Lindblad operator in Eq. 2.51. The study of the interacting Rydberg ensemble for different densities is done with the density matrix formalism. The atomic gas under study is a three-dimensional sample with different atomic densities that are achieved by changing the number of atoms and the interaction volume. Various observables

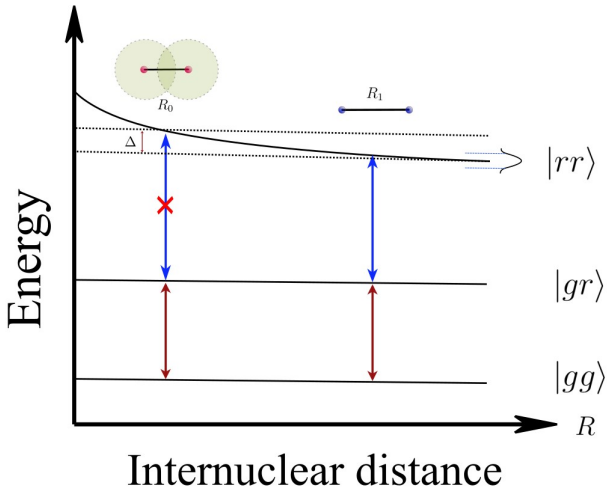

Figure 4.1: Energy level diagram of repulsive interacting Rydberg pairs $|rr\rangle$. The blue detuned ($\Delta > 0$) excitation establishes the pair of Rydberg atoms at an internuclear distance of R_0.

that can be extracted from the density matrix calculations are presented in this chapter.

4.1.1 Blockade and hard sphere model

The classical hard-sphere model presented in chapter 3 can be used to calculate the fraction Rydberg excitation probability. This model is based on coarse-graining of the experimental volume into blockade spheres that is illustrated in Fig. 4.2. The fraction of excited atoms without interaction between excited atoms is $f_0 = \langle \sigma_{rr} \rangle$. This quantity represents the steady-state excitation probability of a single atom. Therefore, the total number of Rydberg excitations in a sample with the density of n and volume V is $N_{Ryd} = f_0 n V$. When there is an interaction

between Rydberg atoms in the system, the blockade volume $\frac{4}{3}\pi R_{bl}^3$ represents an excluded volume out of the total volume in which there is no possibility of other excitations. This results the number of Rydberg excitations to be $N_{Ryd} = f_0 n V_u$. Where V_u is the available volume in the total volume to ground state atoms to be excited to the Rydberg state. Therefore $V_u = V - V_b N_{Ryd}$ is unblockaded volume. The Rydberg excited fraction f_r, is obtained by solving the above equations self constantly. Therefore f_r can be written as [117],

$$f_r = \frac{N_{Ryd}}{N} = f_0 n \frac{V - V_b N_{Ryd}}{N} = f_0 - f_0 n V_b f_r, \tag{4.1}$$

which in terms of f_0 is,

$$f_0 v_b n = \frac{f_0 - f_r}{f_r} = \frac{f_0}{f_r} - 1, \tag{4.2}$$

where $\frac{f_0}{f_r} - 1$ is called blockaded fraction f_{bl}. Defining the critical density as $n_{crit} = \frac{1}{f_0 V_b}$ the blockade fraction can be written as,

$$f_{bl} = \frac{n}{n_{crit}}. \tag{4.3}$$

In the process of coherent excitation in the blockade regime, it is not possible to distinguish between atoms excited to the Rydberg state. This leads to a collective enhancement of the atom-light coupling that improves the excitation rate. This enhancement depends on the number of atoms in the sample. Each realization of the system is defined with the state vector,

$$|\psi\rangle = \sum_{i=1}^{N} c_i |\phi_i\rangle, \tag{4.4}$$

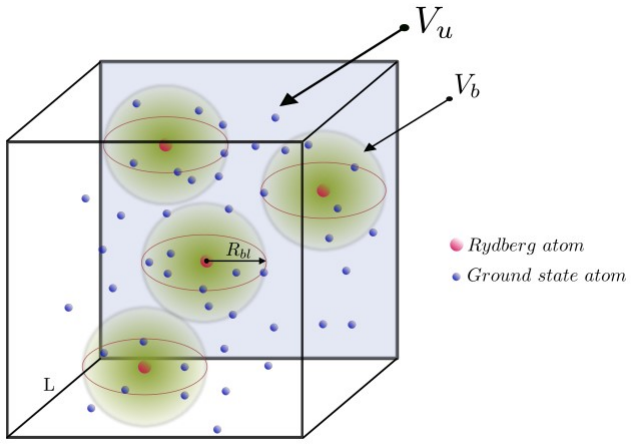

Figure 4.2: The hard spheres that are exclusion volume created by the Rydberg blockade V_b. The V_u is the unblockaded volume.

where c_i is the coefficient vector and $|\phi_i\rangle$ is the basis vector. In the form of product state, the basis states are,

$$|\phi\rangle = \bigotimes_{i=1}^{N} |\alpha_i\rangle = |\alpha_1, ..., \alpha_{N-1}, \alpha_N\rangle \,. \tag{4.5}$$

Here, α_i represent either the ground state or the excited state, $\alpha_i \in \{g, r\}$. The ground state of a many-body system containing N atoms is defined as,

$$|g\rangle = \frac{1}{\sqrt{N}} \sum_{1}^{N} |g_1, g_2, ..., g_i, ..., g_{N-1}, g_N\rangle \,, \tag{4.6}$$

and the excited Rydberg state is,

$$|r\rangle = \frac{1}{\sqrt{N}} \sum_{i=1}^{N} |g_1, g_2, ..., r_i, ..., g_{N-1}, g_N\rangle \,. \tag{4.7}$$

The many-body ground state and the Rydberg blockaded excited state are coupled together with a collective Rabi frequency $\Omega_c = \sqrt{N}\Omega$ [118, 119], and the

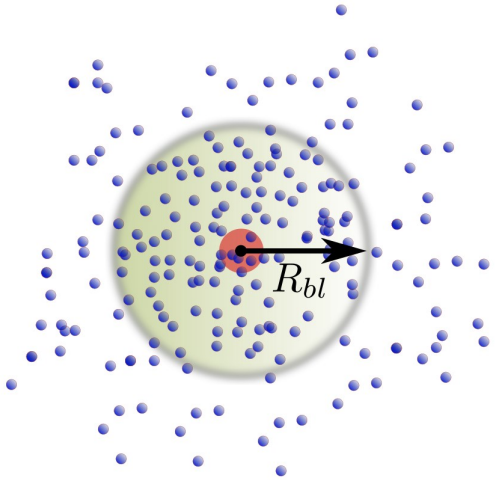

Figure 4.3: Superatom picture. There is only one Rydberg atom present in the volume $4/3\pi R_{bl}^2$. R_{bl} is the blockade radius.

excited state collectively shares the single Rydberg excitation. The collective behavior of the ensemble of atoms is a demonstration of quantum mechanics at mesoscopic scales. In these circumstances, the entire ensemble shows the behavior of a single two-level system. Since in the Rydberg blockade volume, there exists one excitation that is shared between all atoms, this volume can be pictured as a super-atom [120, 121] as depicted in Fig. 4.3. In this picture, Rydberg gases with volume V and density n can be visualized as an arrangement of densely packed blockade spheres similar to face center cubic (fcc) lattices in solids [122]. Comparing the excitation laser energy and the interaction strength, the blockade sets in as soon as the interaction-induced energy shift becomes comparable to the collective Rabi frequency. The collective Rabi frequency declares that there are multiple atoms in a superatom. Considering the blockade

volume as hard-spheres, which means there is a maximum number of blockade volumes that can fit volume V we can drive a relation for blockade radius R_{bl},

$$\frac{C_6}{R_{bl}^6} = \sqrt{N_b}\Omega, \tag{4.8}$$

where N_b is the number of blockaded atoms. Estimating the number of blockaded atoms N_b using an atomic density n in a d-dimensional system leads to $N_b \sim nR_{bl}^d$. Therefore the expression for R_{bl} from Eq. 4.8 becomes,

$$R_{bl} \sim \left(\frac{C_6}{\Omega\sqrt{n}}\right)^{\frac{2}{d+12}}. \tag{4.9}$$

From the above equations (Eq. 4.8 and Eq. 4.9) the number of Rydberg atoms can be calculated [123, 77],

$$N_{Ryd} \sim \frac{N}{N_b} \sim R_{bl}^{-d} \sim C_6^{\frac{2}{d+12}}. \tag{4.10}$$

Eq. 4.10 is extracted based on universal scaling quantum phase transition [77] and is discussed in the following sections.

In our calculations, we make several realizations of the system by randomly generating the position of the atoms in an interaction box. The observables are calculated from averaging over these many realizations. The atomic density is changed by changing the volume of interaction and the number of atoms inside the volume. The sample under study is considered to be a frozen interacting gas [11], where the atoms are motionless, and the blackbody radiation is ignored. This means the lifetime of coherence of the excited state is longer than the experimental observation. With frozen atoms, we study the system dynamics with

Lindblad master Eq. 2.38. In the superatom picture, we can define the n Rydberg excitation probabilities in the ensemble of atoms as $P_r(n) =< \hat{\sum}_r^{(n)} >$ [124]. For a blockaded volume, this probability is $\hat{\sum}_r^{(1)} = \sum_{j=1}^{N} \hat{\sigma}_{rr}^{j} \prod_{i\neq j}^{N} \hat{\sigma}_{gg}^{i}$. The result of the density matrix calculations for dynamics of Rydberg excitation for one and four, two-level atoms with no decay of the Rydberg state ($\Gamma_r = 0$) and with the decay of Rydberg state ($\Gamma_r \neq 0$) are shown in Fig. 4.4a and b. In the Fig. 4.4b the collective Rabi frequency Ω_c is different by a factor of $\sqrt{4}/\sqrt{2} = 1.41421$ for four and two atoms in the same volume.

4.2 Complex susceptibility

The optical response of the ensemble of atoms to the applied electric field is defined in terms of optical susceptibility. The susceptibility χ, is a complex parameter that relates the applied electric field to the polarization density vector [65]. The macroscopic definition of the polarization vector is,

$$\begin{aligned} \mathbf{P} &= (\varepsilon - \varepsilon_0)\mathbf{E} = \varepsilon_0 \chi \mathbf{E} \\ \chi &= \chi_R + i\chi_I, \end{aligned} \tag{4.11}$$

where χ_R is the real part, and χ_I is the imaginary part of the susceptibility. The real part of χ is responsible for the dispersive phase shift, and the imaginary part defines the absorption of light. The non-linear response of a medium to the exposed light is expressed by Taylor's expansion of the χ,

$$\chi = \chi^{(1)} + \chi^{(2)}E + \chi^{(3)}E^2 + \chi^{(4)}E^3 + ..., \tag{4.12}$$

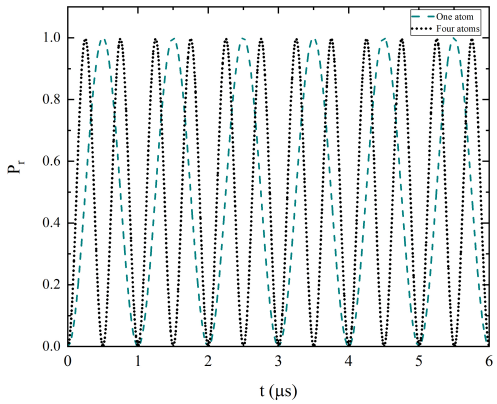

(a) $\Gamma_r = 0$

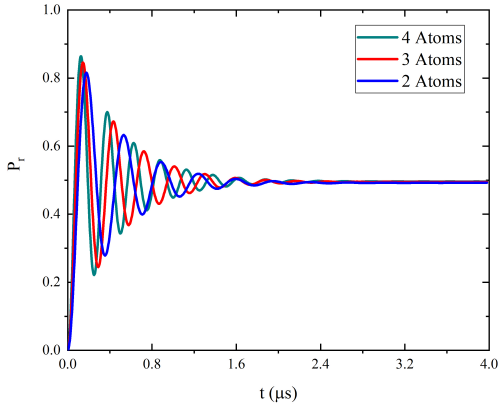

(b) $\Gamma_r = 50$ KHz

Figure 4.4: (a) Probability of Rydberg excitation. The collective Rabi frequency $\Omega_c = \sqrt{N_b}\Omega$, for one and four two-level atoms in the interaction volume. The comparison between one and four atom systems shows a collective relation, $\Omega_c = \sqrt{4}\Omega$. (b) Probability of Rydberg excitation in a superatom for a system with Rydberg state decay of $\Gamma_r = 50$ KHz.

where $\chi^{(1)}$ is the linear response of the medium, and higher-order terms define the medium non-linear response. As one of many possible effects, for instance, $\chi^{(3)}$ corresponds to the Kerr effect [64, 125]. The macroscopic polarization of the medium can be related to individual dipole moments of the atoms by averaging out the dipole moments of individual atoms as [37, 64, 65],

$$\mathbf{P} = n \langle \hat{\mathbf{d}} \rangle \tag{4.13}$$

Here n is the atomic density, and $\langle \hat{\mathbf{d}} \rangle$ is the average dipole moments of a two-level atom in the ensemble. By studying the dynamics of the system through the Eq. 2.38 for the many-body system, the average dipole moment as an observable of the system can be found through density matrix as the expectation value of the $\langle \hat{\mathbf{d}} \rangle$ from,

$$\langle \hat{\mathbf{d}} \rangle = Tr[\rho \, \hat{\mathbf{d}}]. \tag{4.14}$$

Since the dipole moment $\mathbf{d}$, for the same atomic levels are zero, $\langle 1|\hat{\mathbf{d}}|1\rangle = \langle 2|\hat{\mathbf{d}}|2\rangle = 0$ the expression for polarization vector becomes,

$$\mathbf{P} = n \, d_{21}(\sigma_{21} + \sigma_{12}) = 2 \, n \, d_{21}\sigma_{21}. \tag{4.15}$$

Form Eqs. 4.11, 4.13, and 4.15, the macroscopic polarization equation and $\Omega_c = -\frac{\varepsilon_0 \, \hat{d}_{21}.\mathbf{E}}{2}$, the expression for the linear susceptibility is,

$$\chi = -\frac{2 \, n \, d_{21}^2}{\Omega_c \, \varepsilon_0 \hbar} \, \sigma_{21}. \tag{4.16}$$

Where n is the density, d is the magnitude of the dipole moment, and σ_{21} is the projection operator defined in chapter 2.

In our calculations, the total susceptibility is the addition of individual susceptibilities caused by each atom. It is defined as,

$$\begin{aligned}\chi_{total} &= \sum_i \chi_i \\ &= -\frac{2\,d_{21}^2}{\Omega_c\,\varepsilon_0\hbar\,V}\,\sum_i \widetilde{\sigma}_{21}^i,\end{aligned} \tag{4.17}$$

where V is the volume, and χ_i is the susceptibility of all individual atoms. $\widetilde{\sigma}_{21}^i$ is the element of the density matrix for the i^{th} atom. For example, for a system containing two atoms, the density matrix is,

$$\begin{pmatrix} \sigma_{11}[1]\sigma_{11}[2] & \sigma_{11}[1]\sigma_{12}[2] & \sigma_{11}[2]\sigma_{12}[1] & \sigma_{12}[1]\sigma_{12}[2] \\ \sigma_{11}[1]\sigma_{21}[2] & \sigma_{11}[1]\sigma_{22}[2] & \sigma_{12}[1]\sigma_{21}[2] & \sigma_{12}[1]\sigma_{22}[2] \\ \sigma_{11}[2]\sigma_{21}[1] & \sigma_{12}[2]\sigma_{21}[1] & \sigma_{11}[2]\sigma_{22}[1] & \sigma_{12}[2]\sigma_{22}[1] \\ \sigma_{21}[1]\sigma_{21}[2] & \sigma_{21}[1]\sigma_{22}[2] & \sigma_{21}[2]\sigma_{22}[2] & \sigma_{22}[1]\sigma_{22}[2] \end{pmatrix}. \tag{4.18}$$

The brackets [1] and [2] after the σ show that the expression belongs to atoms 1 and 2, respectively. The matrix elements that need to be considered for calculating the susceptibility of the atom one χ_1 are $\sigma_{11}[2]\sigma_{21}[1]$ and $\sigma_{21}[1]\sigma_{22}[2]$. Furthermore, for the second atom χ_2, the elements of the density matrix contributing to the susceptibility of atom two are $\sigma_{11}[1]\sigma_{21}[2]$ and $\sigma_{21}[2]\sigma_{22}[1]$. Therefore, the expression for the total susceptibility for a system with two atoms is,

$$\chi_{total} = -\frac{2\,d_{21}^2}{\Omega_c\,\varepsilon_0\hbar\,V}\,(\sigma_{11}[2]\sigma_{21}[1]+\sigma_{21}[1]\sigma_{22}[2]+\sigma_{11}[1]\sigma_{21}[2]+\sigma_{21}[2]\sigma_{22}[1]) \tag{4.19}$$

The result of the susceptibility for several interaction volumes (Fig. 4.5) and a

different number of atoms on resonance $\Delta = 0$, is shown in Fig. 4.6, and as a function of the detuning of the laser light in Fig. 4.7. Each curve in Fig. 4.7 is an average of 50 sets of random positions of atoms in the interaction box. Each set of random positions of the atoms represents a single realization of the experiment. Since the position of the atoms is generated randomly, the atoms have different interactions in every single realization of the experiment. To study the dynamics of the system, the Lindblad master equation is solved (Eq. 2.38) for many-body interacting Rydberg gas. The data for imaginary part of the susceptibility is illustrated in Fig. 4.6 and Fig 4.7. These plots are for when the system reaches equilibrium in each realization of the experiment. This is equivalent to solving the stationary Lindblad master equation, $\frac{d\rho}{dt} = 0$. The important feature of Fig 4.7 is the critical density of the system, after which adding any number of atoms to the system will not change the susceptibility. At the critical density, the system susceptibility with several atoms in the interaction volume is the same as the susceptibility caused by one atom in the same region. This indicates that the system is in the blockaded regime, and only one atom is allowed to be excited into the Rydberg state. Decreasing the system volume (size of the experimental volume) reduces the distance between the atoms and increases the interaction simultaneously. This shifts the required energy for the second and higher number of atoms excitation out of reach of the laser linewidth. It means there is no more than one excitation in the system, and the excitation to the Rydberg state is suppressed. The critical size after which the system enters into the strongly

interacting regime (interaction volume L^3) is for the volume with a side length of $4 < L < 5$ μm. This gives a critical density of $1.6 \times 10^{10} \lesssim n_{crit} \lesssim 6.25 \times 10^{10}$ cm^3 when there are 2 to 4 atoms in the interaction volume. The critical density n_{crit}, separates the two phases of the system, from weak interacting to strong interacting phases. The formation of the Rydberg blockaded system at a specific n_{crit}, sets the boundary between these two phases. Fig. 4.8 shows fluctuation of the susceptibility around its mean value for several realizations of the system. The fluctuations in the weakly interacting regime are small. As the system enters smaller system sizes ($L \sim 10$ μm), the fluctuation in susceptibility increases due to increasing interaction strength. Reducing the system size which results in increasing the interaction strength, the fluctuation in susceptibility reaches its maximum value at $L \sim 5$ μm and drops to zero for $L \sim 3$ μm. In system sizes $L \sim 3$ μm, the interaction between the Rydberg state is strong, and all curves belonging to a different number of atoms collapse into one curve. This means there is just one atom in the system excited into the Rydberg state, and the blockade volume is formed. The expected experimental absorption signal also drops when the system enters into blockaded strong interaction regime. The experimental absorption signal can be calculated from the imaginary part of the susceptibility. The electric field of the laser field that passes through a medium with length l is,

$$E = E_0 e^{i(kn_r l - \omega t)} = E_0 e^{-k\chi_I l/2} e^{i(k\chi_R l/2 - \omega t)}, \tag{4.20}$$

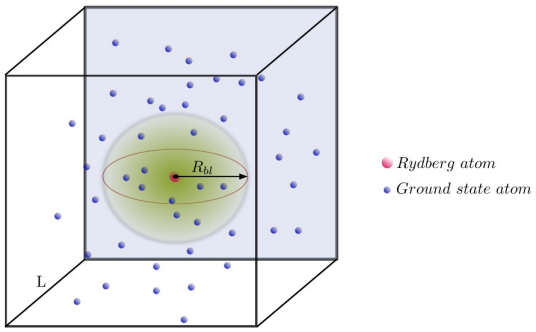

Figure 4.5: The interaction (experimental volume) with length L. The blockade volume is shown as a green sphere at the center of the box. Blue circles are ground state atoms, and the red circle shows the excited Rydberg state.

where k is the wave vector, n_r is the refractive index, χ_I and χ_R are the imaginary and real part of the susceptibility, respectively. A light passing through a medium is attenuated caused by the imaginary (absorptive) part of the susceptibility χ_I. The outcoming light also experiences a phase shift introduced by the real part of the susceptibility, χ_R. The relation between the imaginary and real part of the susceptibility to the passing light in the medium can be written as,

$$\begin{aligned} T &= \frac{I}{I_0} = exp^{(-k\chi_I l)} \\ \Delta\phi &= k\chi_R l/2. \end{aligned} \tag{4.21}$$

Eq. 4.21 shows that one can get information about the susceptibility in the experiment by measuring the transmitted light or its phase shift [103].

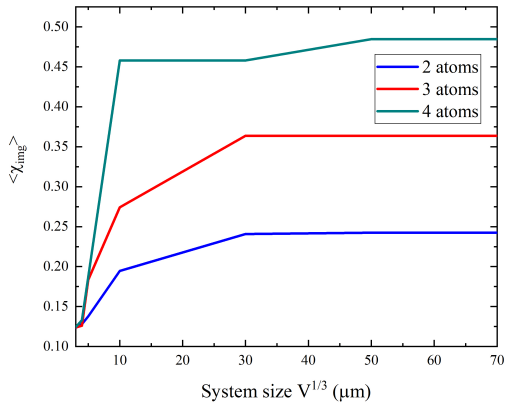

Figure 4.6: Imaginary part of susceptibility for interacting many-body Rydberg gas on resonance, $\Delta = 0$. The suppression of the imaginary part of the susceptibility appears after the size of the interaction volume is reduced and reaches $L \sim 5$ μm ($V = L \times L \times L$). The system entered into the strongly interacting regime, which is the blockaded regime.

4.3 Pair correlation function, $g^{(2)}(\mathbf{R})$

The pair correlation function $g^{(2)}(\mathbf{R})$, defines the spatial correlation between Rydberg atoms. It measures a conditional probability of the existence of an excited Rydberg atom at a distance of R from an already excited atom. The van der Waals interaction introduced in section 2.4 only depends on the internuclear distance between the atoms, $R = R_i - R_j$. The pair correlation function for two atoms is defined as [126, 127],

$$g_{ij}^{(2)} = \frac{\langle \sigma_{rr}^{i} \sigma_{rr}^{j} \rangle}{\langle \sigma_{rr}^{i} \rangle \langle \sigma_{rr}^{j} \rangle}. \tag{4.22}$$

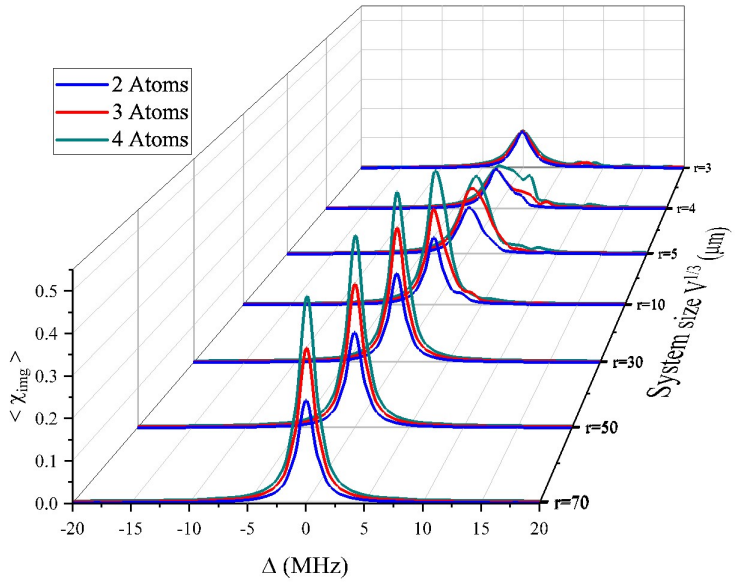

Figure 4.7: Imaginary part of susceptibility for interacting many-body Rydberg gas. After the length size of the interaction volume reaches $L \sim 5\ \mu$m, there is a suppression of the imaginary part of susceptibility. The distortion of the plots at $10 \lesssim L \lesssim 4\ \mu$m, particularly for the four atoms case, is due to the increased interaction between the atoms. In this region, some atoms are excited on different detuning (not on resonance). The imaginary part of susceptibility is proportional to the absorption signal in the experiment. Increasing the number density does not change the system response to the monochromatic laser light, and the system is in a blockaded regime. For larger interaction volumes, however, adding the number of atoms from 2 to 4 atoms in the interaction volume enhances the absorption of the monochromatic light in the system as the susceptibility increases.

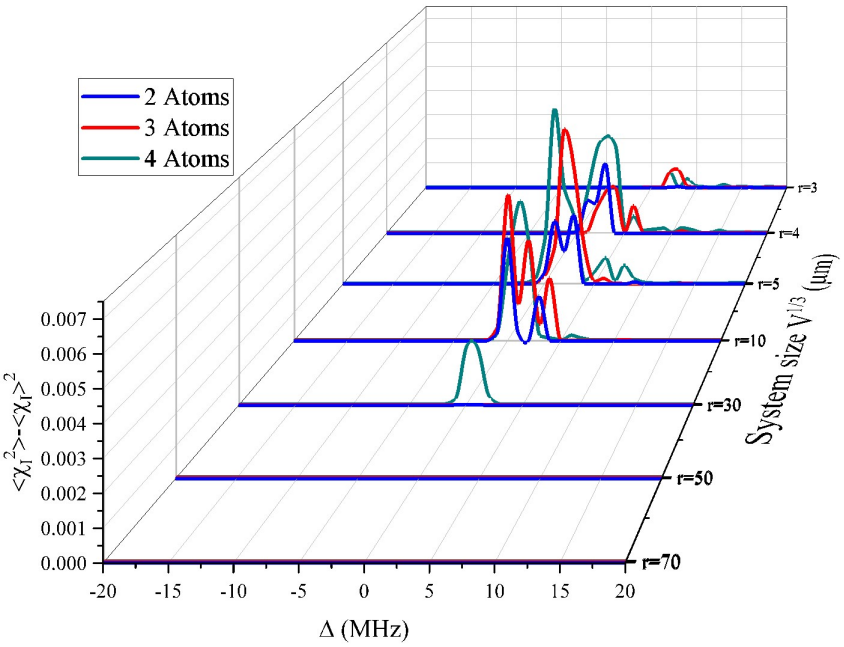

Figure 4.8: Fluctuations in the imaginary part of susceptibility for interacting many-body Rydberg gas. Around system sizes of $L \sim 10$ μm, fluctuations in the susceptibility are increased at resonance $\Delta = 0$ MHz. This system size ($L \sim 10$ μm) is the starting point for suppressing the imaginary part of susceptibility. The fluctuations are maximum at $L \sim 5$ μm. They decrease for smaller system sizes and become close to zero for $L \sim 3$ μm, where all systems with different atom numbers show the same susceptibility. This indicates the transition between the weakly interacting regime to the strong interaction regime where the blockade volume is formed.

The pair correlation of the whole system consists of summation over all interacting pairs and is defined as,

$$g^2(R) = \frac{\sum_{ij}^{(R,|R_i-R_j|)} g_{ij}^2}{\sum_{ij}^{(R,|R_i-R_j|)} 1}, \tag{4.23}$$

where $\sum_{ij}^{(R,|R_i-R_j|)}$ is the sum over all interacting pairs with a distance $|\mathbf{R_i} - \mathbf{R_j}|$ that are confined in domain $[R, R + |R_i - R_j|]$. The denominator gives the number of pairs in the system. This means for systems with $g^{(2)}(R) = 1$, the atoms are uncorrelated and $g^{(2)}(R) = 0$ represents the pairs with a small mutual distance that cannot be excited simultanously [123]. For $g^{(2)}(R) > 1$ the Rydberg excitation are more likely seperated by a distance R than uncorrelated atoms ($g^{(2)}(R) = 1$). The blockade radius can be evaluated through the pair correlation function, Eq 4.23. Fig. 4.9 shows the pair correlation function at resonance ($\Delta = 0$) after the system reaches its stationary state, $t_{max} = 250/\Omega$. Analyzing the calculated blockade radius given in Eq. 4.9, can be done by comparing it to the pair correlation plots in Fig. 4.9. At system sizes $L = 3\,\mu\,\mathrm{m}$, the pair correlation is zero. For different Rabi frequencies the pair correlation function is different as predicted in Eq. 4.9. For different Rabi frequencies (Ω) and system sizes $4.25 \lesssim L \lesssim 6.40\ \mu\mathrm{m}$, the curves for various numbers of atoms are separated from each other (indicated with the dashed line in Fig. 4.9) introducing different pair correlation values in the same experimental volume. Below the point of separation, all curves collapse to the same value, which can only happen if there is just one excitation in the system. For instance, for

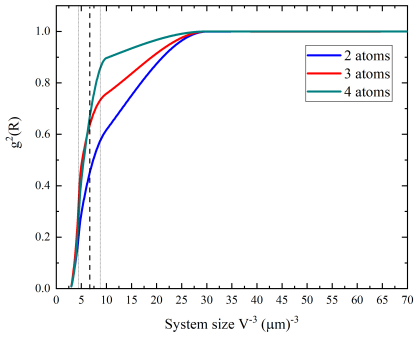

(a) $\Omega = 0.1$ MHz

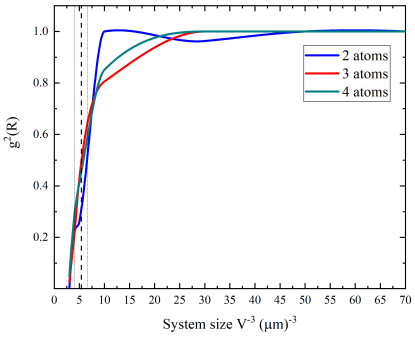

(b) $\Omega = 0.2$ MHz

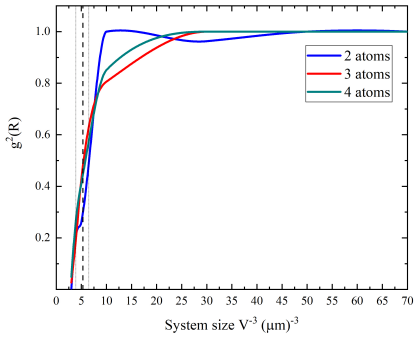

(c) $\Omega = 0.4$ MHz

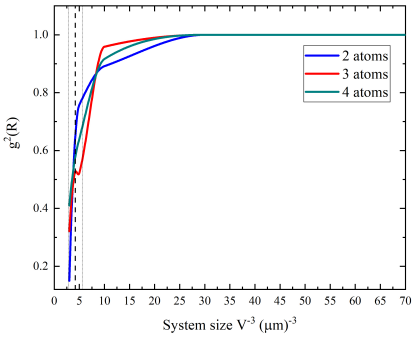

(d) $\Omega = 1$ MHz

Figure 4.9: Pair correlation function $g^2(R)$, at resonance $\Delta = 0$ for different atom numbers after $t_{max} = 250\,\Omega$ evolution time, in the stationary regime. $g^2(R) = 0$ for system sizes ≤ 3 μm which corresponds to densities $\gtrsim 10^{11}$ cm^{-3}. The dashed line represents the position of the blockade radius. When the size of the system is of the order of the blockade radius, the correlation between atoms for various atom numbers gives the same correlations.

$\Omega = 0.1$ MHz, for $L \lesssim 6.40\,\mu$m, all curves for a different number of atoms (2, 3, and 4 atoms) collapse into one curve. Therefore the estimate of the blockade radius is $5 \lesssim R_{bl} \lesssim 8.5$ μm with center at $R_{bl} \approx 6.40$ μm. The calculated blockade radius from Eq. 4.9 for $\Omega = 0.1$ MHz, and density of $n = 3.2 \times 10^{16}$ m^{-3}, is $R_{bl} = 6.40286$ μm. With the same analogy, for different Rabi frequencies $\Omega = 0.2, 0.4,$ and 1 MHz the blockade radii are, 5.54, 5.08, and 4.25 μm, respectively. This comparison shows the scaling expression and density matrix calculation (Eq. 4.9) give a reasonable and comparable values for the blockade radii (R_{bl}) for different system sizes and different Rabi frequencies. Another important feature of Fig. 4.9a is that the correlations become stronger as the density increases.

4.4 Rydberg excitation statistics, Mandel Q parameter

The mean number of Rydberg excitation $\langle N_{Ryd} \rangle$ does not provide a qualitative study of the Rydberg population in each realization of the system. This prohibits detailed information on the number of excitations in each realization of the system. To study the excitation dynamics, the Mandel Q factor [128] provides proper knowledge of the system. Many system realizations should present small or no fluctuations in the blockade regime. This also can be quantified by the Q parameter. Mandel Q factor defined as [128],

$$Q = \frac{\langle N_{Ryd}^2 \rangle - \langle N_{Ryd} \rangle^2}{\langle N_{Ryd} \rangle} - 1 \tag{4.24}$$

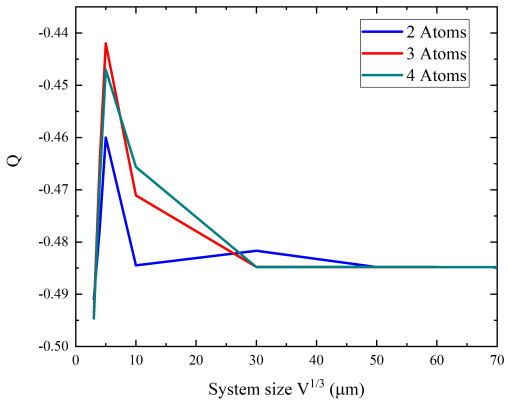

Figure 4.10: Mandel Q factor at resonance excitation $\Delta = 0$ for different system sizes and $\Omega = 0.1$ MHz.

where $\langle N_{Ryd} \rangle$ is [123],

$$\langle N_{Ryd} \rangle = 0 + P_{Ryd}(1) + P_{Ryd}(2) + P_{Ryd}(3) + ... \tag{4.25}$$

and the q^{th} order of the Rydberg excitation is,

$$\langle N^q_{Ryd} \rangle = \sum_{0}^{m_{max}} m^q P_{Ryd}(m). \tag{4.26}$$

Here $P_{Ryd}(m)$ is the probability of seeing exactly m excited atom to the Rydberg state in the system. This probability can be found by,

$$P_{Ryd}(m) = \sum_{i=1}^{N} \rho_{ii} \delta_{m^{(i)},m}, \tag{4.27}$$

where $m^{(i)}$ is the number of excitation in state $|\phi_i\rangle$ in Eq 4.4. The delta Kronecker ensures that only diagonal density matrix elements with m number of excitations are included in the summation. The characterization of the excitation statistics

with the Mandel Q parameter value gives the statistics on counting Rydberg excitations. It compares the measured excitation number fluctuations to the Poisson statistics ($\langle N^2\rangle - \langle N\rangle^2 = \langle N\rangle$). The suppression of fluctuations in the counting statistics of Rydberg excitations is one of the consequences of the formation of the Rydberg blockade [68]. For $Q = 0$ the excitation is Poissonian, while $Q < 0$ is sub-Poissonian (squeezed), and $Q > 0$ is super-Poissonian (broadened) statistics [129, 69, 130]. From the blockade sphere picture for high densities, the number of Rydberg excitations in the gas is determined by the number of blockaded spheres that can fit into the interaction volume, which is the excitation volume created by the laser mode volume. In the dense packing limit, where the blockade spheres fill out the excitation volume, the fluctuations of Rydberg excitation are minimum between consecutive system realizations, and the number of Rydberg excitations is fixed. This can be seen as a transition from a weak interacting regime to a strongly interacting regime. This characteristic is evident in observables such as number distributions of Rydberg excitations and consequently in Mandel Q parameter from Poissonian to sub-Poissonian statistics [67]. Therefore, the extent of sub-Poissonian character is a measure for the blockade effectiveness [131]. Fig. 4.10 shows the Q parameter for the on-resonance case for the system with different sizes and various atom numbers in the interaction volume. For Fig. 4.10 the Rabi frequency is $\Omega = 0.1$ MHz, the decay of the Rydberg state is $\Gamma_r = 50$ KHz, and the interaction coefficient is $C_6 = 19970$ MHz μm^6 [53]. The fluctuation in the number of Rydberg excitations

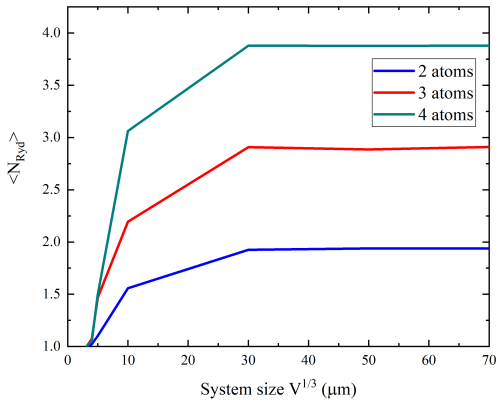

Figure 4.11: The number of excited atoms for different system sizes at resonance $\Delta = 0$ MHz. At $L \approx 5$ μm, the number of Rydberg excitations for 3 and 4 atoms systems collapse to the same value. The highest fluctuation in the number of excitation (highest Q value) appears at this system size.

is small for large system sizes. Decreasing the system size (increasing density) to $L = 5$ μm, which corresponds to $\sim 10^{10}$ cm^{-1}, a jump in fluctuations of the Rydberg excitation appears. The fluctuation again decreases for $L = 4$ and 3 μm system sizes. The lowest fluctuation is at $L = 3$ where there is just one Rydberg excitation in the system. At $L \approx 5$ μm the interaction between Rydberg state starts to push the required excitation energy for the consecutive excitations out of reach of the laser linewidth, and the blockade volume start to form. This is the resonant distance between pair of atoms. The number of excited atoms is shown in Fig. 4.11. Fig 4.12 also shows the number of Rydberg excitation populations for various detunings and system sizes. The sub-Poissonian counting statistics

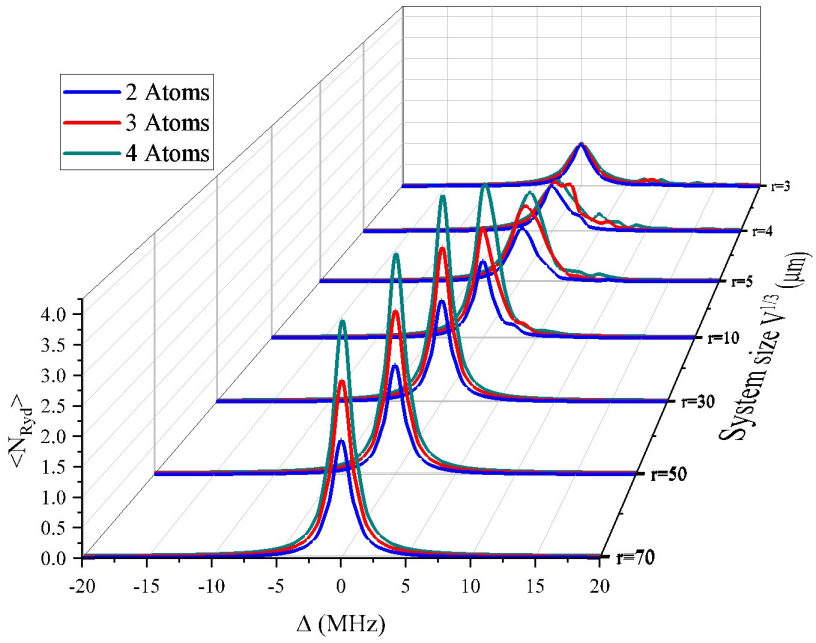

Figure 4.12: Average number of excited atoms in different volumes (densities). When the interaction volume is deceased, the suppression of the number of excited atoms appears. After interaction volume reaches $\sim 4^3\mu$m adding more atoms into the interaction volume will not change the number of excited atoms in the system.

of Rydberg excitations in an ultracold atomic sample is the clear signature of many-body quantum correlations [68]. The Mandel Q parameter also can be defined in terms of the pair correlation function,

$$Q = 4\pi n_c rit \int \left(\frac{N-1}{N} g^{(2)}(R) - 1 \right) R^2 dR, \tag{4.28}$$

where N is the total number of atoms in the excitation volume. n_{crit} is the critical Rydberg density, $n_{crit} \propto R_{bl}^{-d}$, where d is the system dimensionality. Eq. 4.28 highlights that sub-Poissonian counting statistics are connected to the spatial correlations presented by pair correlation function $g^{(2)}(R)$ [131].

4.5 Phase transition in interacting Rydberg ensembles

In macroscopic systems, the classical thermodynamics concepts are required to express the phase transition and phase states of any system. Thermodynamics defines suitable physical quantities that describe macroscopic properties of matter [132]. In classical thermodynamics, the transition between two phases of a macroscopic system is a result of variations in one of the thermodynamic parameters of the system (for instance, temperature) and has a discontinuous character. The variable that controls the phase transition is usually an intensive variable, for instance, pressure, temperature, index of refraction, and density. The classical thermodynamic description of phase transitions is successful in expressing the universal character of phase transitions. It can appropriately describe different systems with different interactions between atoms and molecules without

revealing the essence of underlying phenomena at a microscopic level [133]. This section studies the microscopic character of phase transition in the ensembles of interacting Rydberg atoms.

4.5.1 First and continuous phase transition

A phase transition in a system happens when there is a singularity in a thermodynamic potential or one of its derivatives, such as free energy $\mathcal{F}$. When these singularities exist, a sharp change in the properties of the matter is visible. There are many examples of such changes in substances, such as transitions from gas to a liquid, from a regular conductor to a superconductor, from paramagnets to ferromagnets, or changes that happen in the solutions of surfactant molecules when increasing the concentration of a surfactant. The phase transition is usually classified into first and continuous phase transitions. If a finite discontinuity is present in one (or more) of the thermodynamic potentials, the transition is classified as a first-order phase transition. If the first derivative is continuous but the second or higher derivatives are discontinuous or infinite, the transition is called continuous or critical. Sometimes the continuous phase transition is referred to as second-order phase transition or higher-order depending only on singularities in the derivative of the thermodynamic potential. This classification is founded on Ehrenfest defining the order of transitions which is based on discontinuities in the thermodynamic derivatives [134]. The Ehrenfest classification does not consider the divergence of the thermodynamic quantity. Mainly Fisher's

definition of a continuous phase transition is referred to as the classification for higher-order phase transitions [135]. The appropriate thermodynamic potential depends on the system. For example, for magnetic systems, the free energy $\mathcal{F}$ defined as,

$$\mathcal{F} = E - TS, \tag{4.29}$$

is the appropriate thermodynamic potential, while for liquids, Gibb's free energy,

$$\mathcal{G} = \mathcal{F} + PV, \tag{4.30}$$

is the proper thermodynamic potential. In Eq. 4.29, E is the internal energy, T and S are temperature and entropy respectively. In Eq. 4.30, P is the pressure and V is volume of the system. In liquid systems, the discontinuities appear in the volume, and entropy [136].

4.5.2 Classical and quantum phase transitions

Phase transitions also can be categorized based on the type of fluctuations in the ordered state that the system experience at the transition between phases. The phase transitions that occur at finite temperature are called classical phase transitions. In this type of phase transition, the macroscopic order such as crystal structure, is destroyed by thermal fluctuations. The second type of phase transition is non-thermal phase transitions, in which the transition happens at zero temperature and all thermal fluctuations are frozen out. This type of transition is due to quantum fluctuations that may be strong enough to drive

a transition from one phase to another by breaking the ordered state of the system and resulting in a macroscopic change in the system [76]. They are often called quantum phase transition since they are embedded in the Heisenberg uncertainty principle. The control parameter in quantum phase transition is non-thermal such as a magnetic field or pressure [137]. These types of systems in which the concept of temperature is absent exist in many fields, such as social sciences, economics, informational processes, etc. Despite the differences in the thermal and non-thermal systems, it was discovered that the behavior of such non-thermal systems resembles the behavior of thermodynamic systems, especially at the phase transition, which is identical to the critical phenomenon of statistical physics [138].

4.5.3 Phase transition and universality in interacting Rydberg systems

As described in the previous sections, thermodynamics gives a universal macroscopic description of the equilibrium properties of phase transitions. This is independent of the precise microscopic nature of the transition. To understand the nature of phase transitions at the microscopic level, one needs to study the specifics of the interparticle interactions [133]. The formation of the Rydberg blockade caused by the interaction between Rydberg atoms transforms the phase of the Rydberg ensemble from a two-body interacting phase to a many-body collective phase (blockade phase). This section studies the effect of changing

interatomic interaction strength for such transitions. Introducing a dimensionless quantity na^3, one can characterize the strength of the interaction in the system. Where n is the density, and a is a length at which the interaction potential between atoms becomes effective. In the $na^3 \gg 1$ regime, the non-interacting particle approximations are not valid, and quantum correlations become important. There have been many studies done on interacting Rydberg systems with the mean-field approximation for the strongly interacting regime by taking the Rydberg blockade into account [15, 77, 78]. The effective range of the van der Waals potential ($V_{vdW} \approx -C_6/r^6$) that is used in this thesis to express the interaction between Rydberg atoms is $4 \lesssim a \lesssim 10$ μm. Therefore for a system sizes $L = 3$ μm with four atoms in the interaction volume ($n \approx 10^{11}$ cm^{-3}), the system is in a strong interacting regime $10 \lesssim na^3 \lesssim 150$ [15]. By changing the parameters of the system in the many-body Hamiltonian presented in Eq. 2.50 the thermodynamic phases of the Hamiltonian and ensemble of the interacting atoms is explored in this section. The system parameters are system size L (system density n), Rabi frequency Ω, and the detuning Δ. The phase diagram plot in the parameter space of Δ and Ω is shown in Fig 4.13. It shows different phases of the system for the order parameter, which is the Rydberg excitation fraction for different system sizes from $L = 10$ μm to $L = 3$ μm. For $L = 3$ μm, the system is in the strong interaction many-body regime. The Rydberg fraction

number is defined as,

$$f_R = \frac{\langle N_{Ryd} \rangle}{N} = \langle \sigma_{rr}^{(i)} \rangle, \tag{4.31}$$

where N is the total number of atoms, N_{Ryd} is the number of Rydberg atoms in the system, and $\sigma_{rr}^{(i)} = |r\rangle^{(i)} \langle r|^{(i)}$. In Fig. 4.14 the boundary between the paramagnetic phase where all atoms are in the ground state (when $f_R \approx 0$) to the crystalline phase where the Rydberg excitations are spatially distributed. The Mandel Q parameter in Fig. 4.14b for $\Delta > 0$ shows super-Poissonian behavior for that region of the phase diagram indicating the Rydberg excitations are all over the space except for when the van der Waals interactions become comparable to the detuning in the Hamiltonian (Eq. 2.50). The green dashed line in Fig. 4.14a sets the boundary between the system's no excitation phase and small Rydberg excitations phase. This gives a relation between Δ and Ω as $|\Delta| \propto -\Omega^{0.84}$. The Rydberg excitation fraction as a function of the Rabi frequency and detuning exhibits a smooth crossover between 0 excitations and a maximum of half of atoms excitations. The phase transition in the strongly interacting Rydberg ensemble resembles the magnetic phase transition in the spin systems. It has been shown via the mean-field approach that such phase transitions in Rydberg systems are in the universality class of the Ising model, and the behavior of the system is in analogy to the Ising spin system [77]. The Rydberg state corresponds to the spin-up state and the ground state to the spin-down state in the experiment. The interaction between spins is replaced with the van der

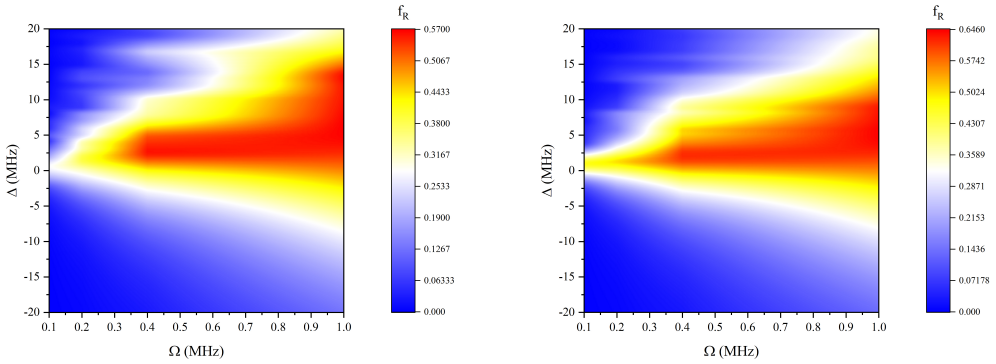

(a) $L = 4$ μm

(b) $L = 5$ μm

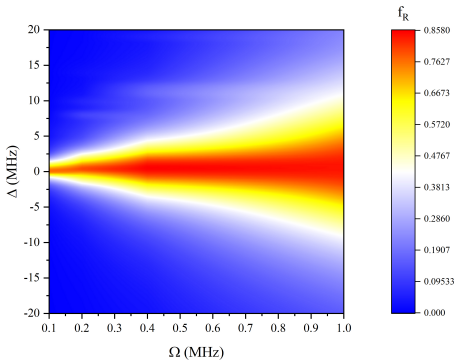

(c) $L = 10$ μm

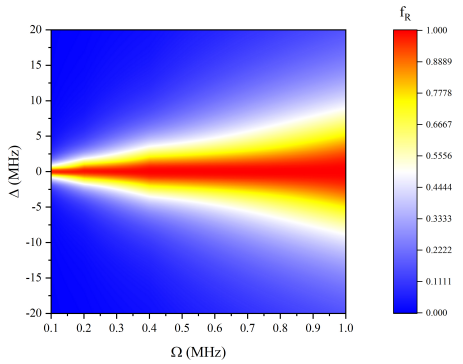

(d) $L = 30$ μm

Figure 4.13: Phase diagram of the system for different densities ($L = 4, 5, 10$ and 30) in Ω and Δ parameter space. f_R is the Rydberg fraction number as defined in the text. Increasing the density from $n = 1.4 \times 10^8$ cm^{-3} corresponding to system size of $L = 30$ μm to $n = 6.25 \times 10^{10}$ cm^{-3} corresponding to system size of $L = 4$ μm, The Rydberg fraction f_R, is reduced from 1 to 0.57 at maximum excitation (Red color).

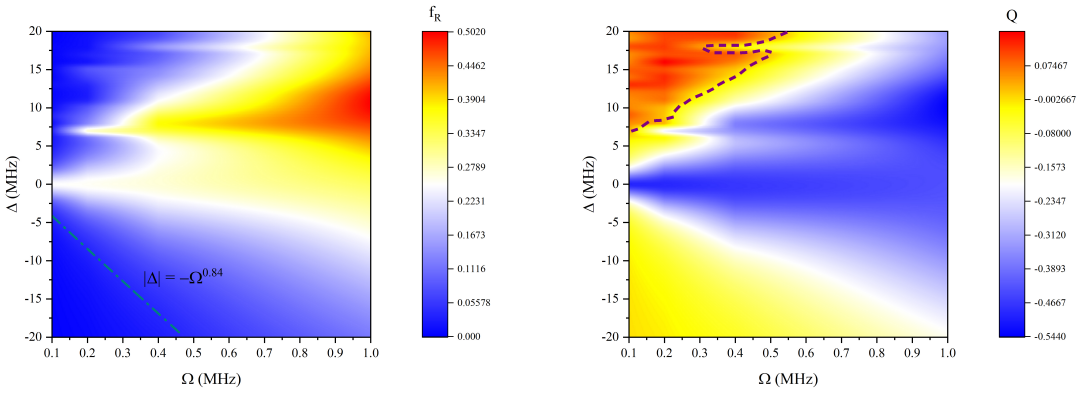

(a) $L = 3$ μm (b) Mandel Q factor

Figure 4.14: (a) The phase diagram of the dissipative interacting Rydberg system for system size of $L = 3$ μm ($n = 10^{11}$ cm^{-3}). The phase diagram is plotted as a function of the Rabi frequency and the detuning. It shows the order parameter, the Rydberg excitation fraction f_R. The dashed line separates the phases from no excitations to when there are excitations in the system. (b) Shows the Mandel Q factor for the same system presented in (a). The super-Poissonian ($Q > 0$) region is separated from Poissonian ($Q = 0$) and sub-Poissonian ($Q < 0$) regions via the red dash line.

Waals interaction, which is repulsive for $|50S\rangle$ Rydberg states. In the interacting Rydberg system, the Rabi frequency corresponds to the critical value of the Ising transverse field, and the detuning corresponds to the Ising interaction [72]. The Hamiltonian in Eq. 2.50 presented in chapter 2 can be written in Ising transverse field Hamiltonian [77, 139],

$$\hat{H} = -\frac{\Delta}{2}\sum_i \hat{\sigma}_z^{(i)} + \frac{\hbar\Omega}{2}\sum_i \hat{\sigma}_x^{(i)} + \frac{C_6}{2}\sum_{i<j}\frac{(1+\hat{\sigma}_z^{(j)})(1+\hat{\sigma}_z^{(i)})}{|\vec{r}_j - \vec{r}_i|^6}, \tag{4.32}$$

where $(1+\hat{\sigma}_z^{(i)}) = 2\sigma_{rr}^{(i)} = 2\,|r\rangle^{(i)}\,\langle r|^{(i)}$ is the projection to the excited Rydberg state of the ith atom. The term with C_6 coefficient is the van der Waals interaction between the Rydberg states. The C_6 (van der Waals coefficient) scales as $\tilde{n}^{11}$, where the $\tilde{n}$ is the principal quantum number of the Rydberg state [1]. For this model, the density matrix solution of the Lindblad equation (Eq. 2.38) in the stationary state regime predicts different regions in the phase diagram of the system.

The zero-temperature phase diagram presented in Fig. 4.14a can be divided into different regions. Close to the critical point ($\Delta_{crit} = 0$ and vanishing $\Omega \to 0$) there is a smooth transition from paramagnet phase ($\Delta < 0$), when all atoms are in the ground state (all spins are downward), to the crystalline arrangement of atoms ($\Delta > 0$). In the crystalline phase, the excitation to the Rydberg state is distributed spacially such that the repulsive van der Waals interaction is minimum. Close to the critical point, where the system exhibits the second-order phase transition, the behavior of the system can be studied based on the

universal scaling as described in the critical phenomenon [140, 141]. The system becomes scale-invariant in the vicinity of the critical point. Consequently, the microscopic details of the system become irrelevant. At the diverging length scale, the macroscopic behavior becomes important due to the long-range physics, and all observables can be described by the power laws of the diverging scale. Many different systems despite having different microscopic properties close to the critical point, where the long-range physics becomes important, behave the same. Depending on the behavior of different systems close to their critical point, they belong to different universal classes [78]. The transition from a strong suppression of Rydberg excitation to the uncorrelated regime can be observed in the pair correlation figures (Fig. 4.15). $g^{(2)}(R)$ is vanishing in the blockaded region. Increasing the system size with the same number of atoms in the system (smaller density), the pair correlation function exhibits a consistent value close to one in Fig. 4.15d for the entire Ω spectrum. For the higher densities (such as $n \approx 10^{11}$ cm^{-3}, $L \approx 3$ μm) there is a region in which the pair correlation function diverges to values > 1.05 shown in crosshatched purple color in Fig. 4.15. The transition from this region to the suppressed Rydberg excitation region is sharp, which is due to van der Waals repulsion [120].

In the critical region, the system is independent of the microscopic arrangement of atoms, and it is considered isotropic and homogenous. In the critical region on the resonance line ($\Delta = 0$), the system follows the critical behavior

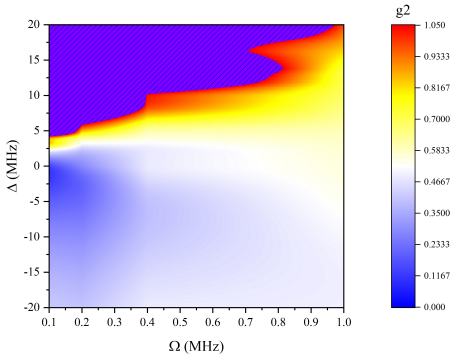

(a) $L = 4$ μm

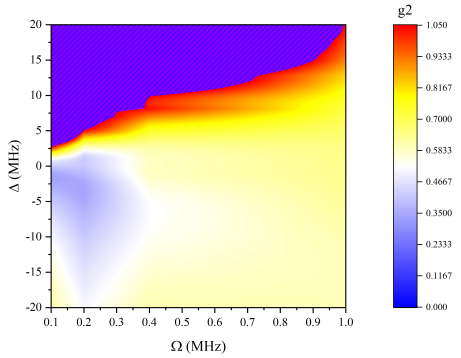

(b) $L = 5$ μm

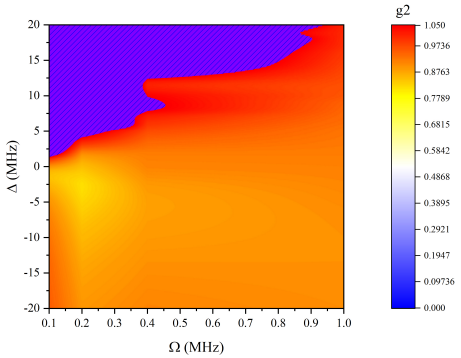

(c) $L = 10$ μm

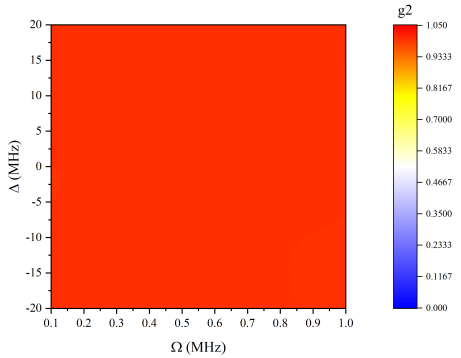

(d) $L = 30$ μm

Figure 4.15: Pair correlation funtion for different system densities in paramter Δ and Ω space. The crosshatched region shows values larger than 1.05. For smaller system sizes, higher densities, the correlated (blue color) region covers a larger portion of the Δ and Ω space. As the system size grows larger (e.g., $L = 30$), the uncorrelated region dominates.

of the second-order quantum phase transition. Therefore, close to the critical point, the system can be characterized by a single dimensionless quantity α. This quantity is defined as $\alpha = \frac{\hbar\Omega}{C_6 n^2}$ and compares the interaction energy ($C_6 n^2$) to the coupling energy ($\hbar\Omega$) [77]. The Rydberg excitation fraction f_R, shows an algebraic behavior and collapse to a simple power-law with respect to α as shown in Fig 4.16 and is in agreement with the categorized universal scaling behavior. The relation between f_R and the α can be written as,

$$f_R \sim \alpha^{\mathcal{V}}, \tag{4.33}$$

where $\mathcal{V}$ is the universal scaling exponent. This exponent is reported before from mean-field calculation [77] to be $\mathcal{V} = 0.404$. By means of density matrix calculations this exponent turns out to be 0.446 ± 0.02533 for $\alpha \ll 1$ as shown in Fig 4.16. This number is $\sim 9\%$ larger than the result obtained from the mean-field approximation reported in [77]. The reason for the different roots in different system sizes and different numbers of atoms that are used in the calculations. For a more accurate comparison, one needs to perform density matrix calculation with a comparable number of atoms to the previous mean-field calculations in [77]. This task is computationally costly since the size of the density matrix grows exponentially with respect to the particle numbers. For N two-level atoms the dimension of the Hilbert space grows as 2^N.

To investigate and observe the phase diagram of the interacting Rydberg systems that have different sizes close to the critical point, in addition to α, a

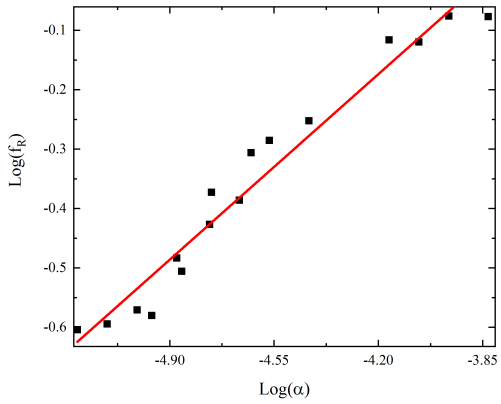

Figure 4.16: Result of calculation along with linear fit to the data (red line) for Rydberg fraction f_R. The Rydberg fraction is plotted as a function of the dimensionless parameter α at resonance ($\Delta = 0$). The exponent extracted from fitting to the data is $\mathcal{V} = 0.446 \pm 0.02533$.

dimensionless detuning δ is defined as a control parameter. This dimensionless quantity is defined by comparing detuning (Δ) with interaction energy ($C_6 n^2$) and is equal to $\delta = \frac{\hbar\Delta}{C_6 n^2}$ [78]. As discussed in the above paragraphs, investigating the phase diagram of the Ising Hamiltonian for interacting Rydberg system, similar to the ferromagnets, the Rydberg blockaded ensemble experiences the second-order phase transition at the critical point $\Delta = 0$. For ferromagnetic materials, the order parameter is the magnetization M. The control parameters are temperature and the magnetic field. Ferromagnetic material experiences the second-order phase transition close to the Curie temperature T_C, and when $H \to 0$. In ferromagnetic materials for temperatures above the Curie temperature T_C the system is non-magnetic and possesses a rotational symmetry. However,

for temperatures below the Curie temperature (T_C) there is a transition to the ferromagnetic phase, and the rotational symmetry vanishes. Close to the second-order phase transition, the system is described with universal scaling laws [78]. In the interacting Rydberg system, the control field H, for the ferromagnetic materials is replaced with α. The dimensionless detuning δ, plays the role of the temperature in the ferromagnetic case. The phase diagram of the Rydberg excitation fraction in δ-α parameter space is depicted in Fig. 4.17. The pair correlation function for the same region in Fig. 4.17 close the critical transition point ($\delta = 0$) is illustrated in Fig. 4.18. Close to the critical point when $\alpha \to 0$ and $\delta < 0$ the pair correlation is minimum and shows values closer to 0 indicating correlated excitation (suppression of excitation). For $\delta > 0$ when $\alpha \to 0$ the Rydberg excitations become uncorrelated by increasing the δ. More insight into the phase diagram can be found from the fluctuations of the Rydberg excitation. Note that in the mean-field approximation studies, because of the nature of the calculation, the pair correlation can not be calculated directly [77]. In the mean-field approximation, all atoms are considered identical and uncorrelated particles. This allows to view the interaction by neighboring atoms as an overall background field, which means the interaction between atoms is based on the effective average interaction of all atoms with each individual atom. In Fig. 4.19 the Mandel Q factor is shown in the δ and α parameter space close to the critical transition point. The transition between sub-Poissonian and super-Poissonian

statistics separates the $\delta < 0$ and $\delta > 0$ regions for $\alpha \to 0$, indicating the transition between two phases. Considering the analogy between ferromagnetic material close to the Curie point and the interacting Rydberg system close to the critical point ($\delta = 0$, $\alpha \to 0$), Fig. 4.20 shows the result of the density matrix calculations for the order parameter f_R. In Fig. 4.20 the Rydberg excitation fraction shows a sudden drop toward zero for $\delta < 0$ and $\alpha \to 0$ values close to the critical transition point ($\delta = 0$). The order parameter in interacting Rydberg ensemble behavior resembles the magnetization close to critical Curie temperature for the ferromagnetic materials [78, 142].

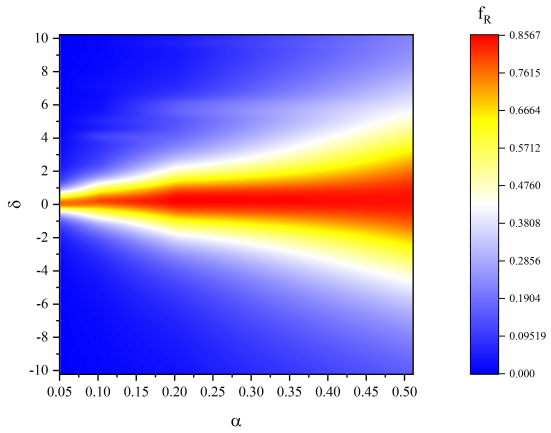

Figure 4.17: Rydberg excitation fraction as a function of dimensionless parameters α and δ. The parameter α is close to critical point $\alpha \to 0$. This region has a higher Rydberg excitation probability for $\delta > 0$. Below 0 ($\delta < 0$), the excitation of the Rydberg state goes to zero for $\alpha \to 0$.

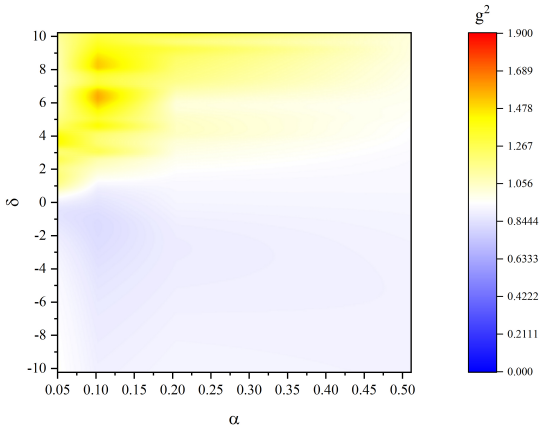

Figure 4.18: Pair correlation function for α and δ space. The correlation between Rydberg excitations in the ensemble separates the parameter space into two regions for $\delta < 0$ and $\delta > 0$. Where for $\delta < 0$, $g^{(2)}(R)$ is smaller than 1 and for $\delta > 0$ it grows to values larger than 1. As we sweep the parameter space closer to the critical point $\delta = 0$ and $\alpha \to 0$, $g^{(2)}(R)$ is closer to 0, which shows correlated Rydberg excitations.

4.6 Off-resonant excitation

Off-resonant excitations arise when the laser detuning compensates the Rydberg interaction. For the off-resonant laser frequency the interaction potential V_{rr}, can compensate for the detuning Δ, which results in the $V_{rr} = \Delta$ condition for a two-level system. This means that in spite of the Rydberg blockade, two atoms can simultaneously be excited to the Rydberg state off-resonantly. The study of off-resonant laser excitation showed a dynamical formation of floating

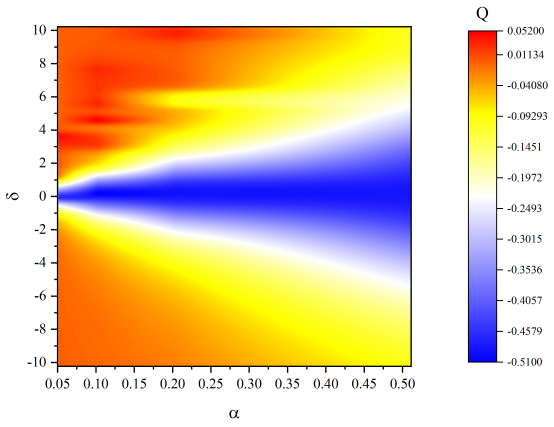

Figure 4.19: Mandel Q parameter showing the fluctuation in the parameter space for dimensionless parameters δ and α. For $\delta > 0$ close to the critical point $\alpha \to 0$, the system experiences super-Poissonian Rydberg excitation statistics. For $\alpha > 0$ and on resonance $\delta = 0$ the Rydberg excitation fraction shows sub-Poissonian statistics.

Rydberg excitation crystals which provides a possibility of adjusting the lattice constants through the laser detuning [123, 131]. The far off-resonant excitation can also overcome the excitation blockade resulting in the possibility of selectivity exciting pair of atoms to the Rydberg state at a shorter distance compared to the blockade radius [143]. The strongly correlated excitations in many-body systems where the Rydberg excitation is the source of interaction and the excitations are restricted to specific distances called Rydberg aggregates [73, 74]. In this section the pair correlation $g^{(2)}(R)$, Mandel Q parameter, and Rydberg excitation number $< N_{Ryd} >$ are presented for detuning range of $-20 < \Delta < 20$ MHz. The density matrix formalism makes it possible to study the dynamical properties of

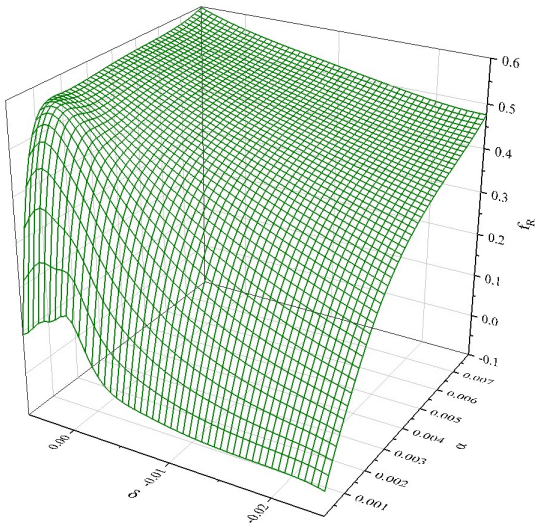

Figure 4.20: Result of density matrix calculations for Rydberg excitation fraction in parameter (δ and α) space close to the second-order phase transition.

the system that are presented in this chapter. The presented data correspond to t_{max} when the system reaches its stationary state. The dynamical study of the system with means of density matrix calculation is the subject of a future study. The mechanism of off-resonant excitation in Fig. 4.1 shows that positive detunings ($\Delta > 0$) can partially balance for the repulsive interaction, for instance, the repulsive interaction between Rydberg atoms in $|50S\rangle$ states. That means Rydberg pairs separated by $\sim R_0$ are preferred. The off-resonant excitation sets distance resonant condition,

$$R_{dis-res} = \left(\frac{C_6}{\Delta}\right)^{\frac{2}{d+12}}, \tag{4.34}$$

for a d dimentonal system. Off-resonant excitation for blue detuning features a positive Q value at high densities $n \gtrsim 10^9$ ($L \lesssim 10$ μm). These super-Poissonian statistics imply broadening excitations of the Rydberg state. This means that in an experiment, one can see a strong fluctuation in the Rydberg excitation. The fluctuations in the excited atom number are shown in Mandel Q parameter in Fig. 4.21. The super-Poissonian feature of the excitation is not present up to atomic densities $\sim 4 \times 10^9$ cm^{-3} (system size of $5 \lesssim \mathrm{V}^{1/3} \lesssim 10$ μm), and the excitation statistics follow the Poissonian statistics. When the system enters the strongly interacting regime (system size of $\mathrm{V}^{1/3} \lesssim 5$ μm), the off-resonant excitations feature super-Poissonian (broadened) excitation. The broadened excitation increases for off-resonant excitation as the density of the system and the interaction between atoms increase. Close to $n \sim 10^{11}$ cm^{-3} the blue detuned off-resonant excitation is maximum.

The pair correlation function also shows non-trivial behavior at off-resonant detuning in system densities around $\sim 4 \times 10^9$ cm^{-3} corresponding to a system size of $\mathrm{V}^{1/3} \sim 10$ μm. The pair correlation function for various system sizes and densities are shown in Fig. 4.22. The pair correlation function for off-resonant excitation shows the formation of more Rydberg atoms when the laser is detuned from resonance. Fig. 4.23 shows the mean number of excited Rydberg states for different laser tuning when the size of the interaction volume and the number of atoms are changed. The collective coupling of the atoms to the laser field is larger than the detuning. For stronger driving, the collective coupling strength

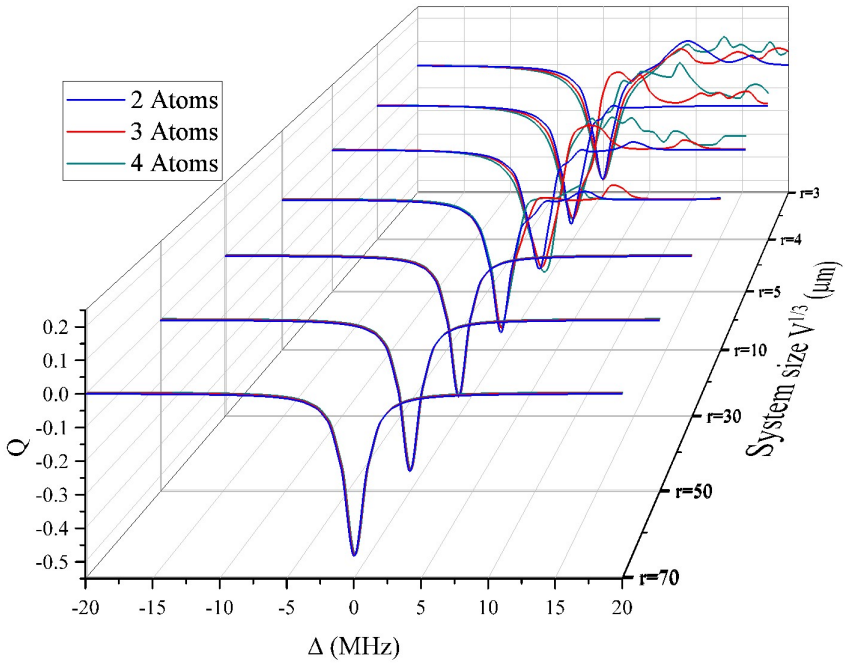

Figure 4.21: Mandel Q factor for $-20 < \Delta < 20$ MHz. The fluctuation in the number of Rydberg excitation increases at off-resonant detuning for system sizes < 10 μm and is visible with the super-Poissonian nature of the curves ($Q > 0$). The Rabi frequency for this figure is $\Omega = 0.1$ MHz.

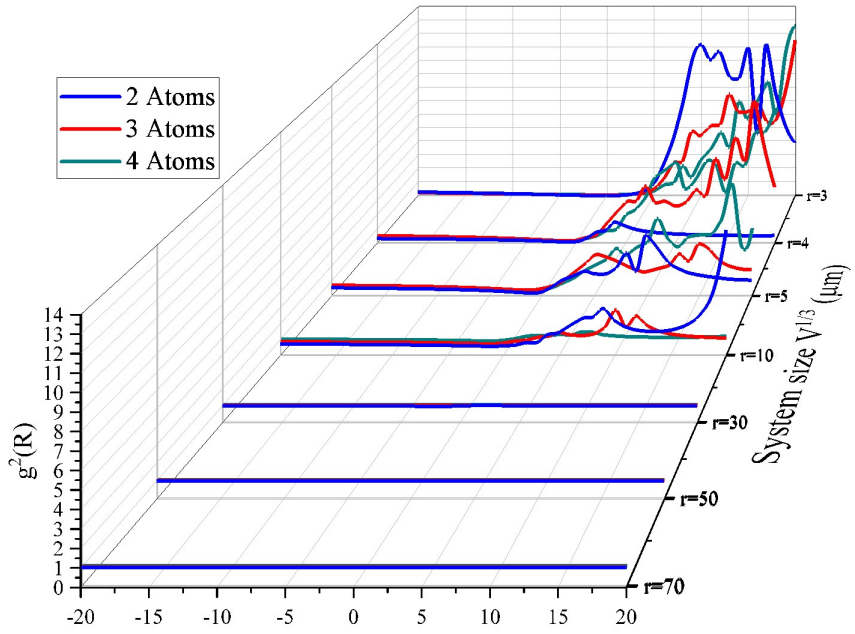

Figure 4.22: Pair correlation function $g^2(R)$ for different density and system sizes at $\Omega = 0.1$ MHz. $g^2(R) = 1$ for system sizes $\gtrsim 5$ μm which corresponds to densities $\approx 10^{10}$ cm^{-3}. The off-resonance (blue detuned) value for the pair correlation function in a strongly interacting regime (system sizes $3 \lesssim L \lesssim 10$ μm) is the indication of highly uncorrelated excitation.

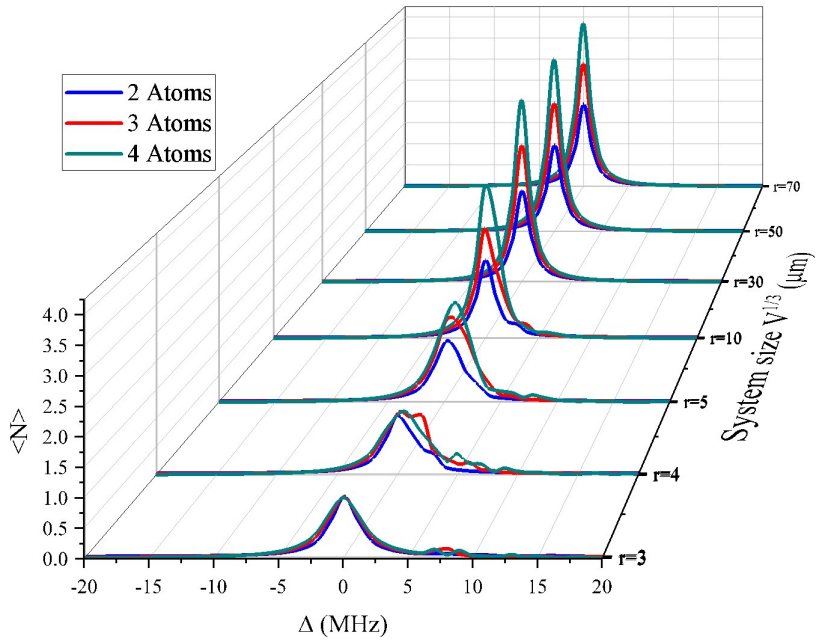

Figure 4.23: Number of excitation for $\langle N_{Ryd} \rangle$ for different densities and system sizes at $\Omega = 0.1$ MHz. $\langle N_{Ryd} \rangle$ depicted here is for when the system is reached to the stationary state. For $\Omega = 0.1$ MHz the off-resonant excitation in the strong interaction regime for system sizes $10 \lesssim L \lesssim 3$ μm (corresponds to densities $\approx 10^{10}$ cm^{-3}) is not comparable to the excitation regime. However, the excitation shows a super-Poissonian feature. This indicates large fluctuations of Rydberg excitation in an off-resonance regime which corresponds to the fact that many atoms are collectively excited in the resonant channel.

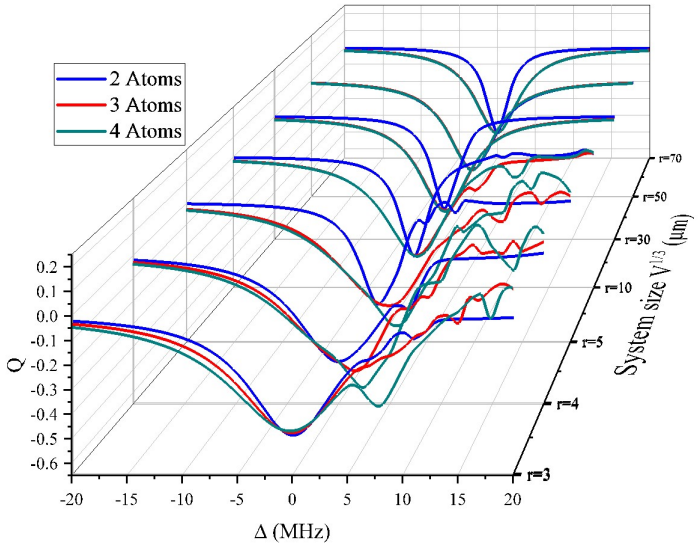

Figure 4.24: Mandel Q factor for $-20 < \Delta < 20$ MHz for driving Rabi frequency of $\Omega = 0.4$ MHz. The fluctuation in the number of Rydberg excitation increases at off-resonant detuning for system sizes < 10 μm. The super-Poissonian nature of the curves ($Q > 0$) can be seen for system sizes $L \lesssim 10$ μm.

$\sqrt{N_b}\Omega$ pushes the off-resonant excitation further in the blue detuning regime. The detuning becomes comparable with $\sqrt{N_b}\Omega$, which results in a comparable number of excitations. For $\Omega = 0.4$ MHz, the Q parameter, pair correlation $g^{(2)}(R)$, and the number of excited atoms for different detuning and system sizes are showed in figures, 4.24, 4.25, and 4.26 respectively. For $\Delta > 0$ the statistical distributions similar to the $\Omega = 0.1$MHz case become super-Poissonian ($Q > 0$). This feature can signify the excitation of aggregates composed of multiple Rydberg atoms [73]. To quantitatively compare the off-resonance excitations for both $\Omega = 0.1$ MHz and $\Omega = 0.4$ MHz, a comparison between Q,

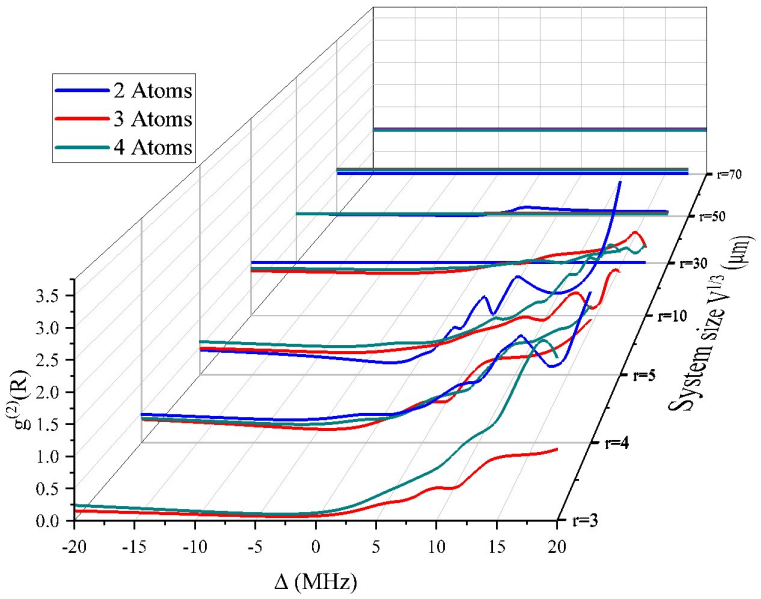

Figure 4.25: Pair correlation function $g^2(R)$ for different densities and system sizes for $\Omega = 0.4$ MHz laser Rabi frequency. $g^2(R) = 1$ for system sizes $\gtrsim 10$ μm which corresponds to densities $\approx 10^{10}$ cm^{-3}. The off-resonance (blue detuned) value for the correlation function in a strongly interacting regime (system sizes $3 \lesssim L \lesssim 10$ μm) is the indication of highly uncorrelated excitation. The pair correlation values for strong driving $\Omega = 0.4$ MHz is smaller compared to the $\Omega = 0.1$ case in Fig. 4.22.

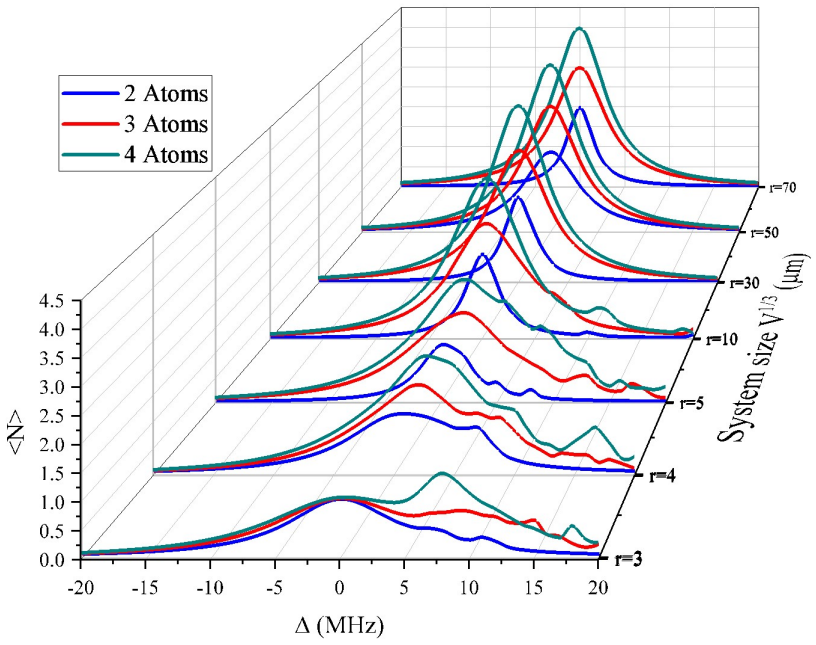

Figure 4.26: Number of excitation for $\langle N_{Ryd} \rangle$ for different densities and system sizes at $\Omega = 0.4$ MHz. The system is in a stationary state. For $\Omega = 0.4$ MHz, the off-resonant excitation in the strong interaction regime, system sizes $10 \lesssim L \lesssim 3$ μm, which corresponds to densities $\approx 10^9 - 10^{11}$ cm^{-3}, is comparable to the excitation regime. However, the excitation shows super-Poissonian characteristics. This indicates large fluctuations of Rydberg excitation in the off-resonance regime, which corresponds to the fact that many atoms are collectively excited in the resonant channel.

$g^{(2)}(R)$, and $\langle N_{Ryd} \rangle$ at detuning of $\Delta = 7$ MHz are depicted in figures, 4.27, 4.28, and 4.29 respectivly. From Fig. 4.29 and Fig. 4.28 it can be seen that the excitation probabilities on the blue side of the resonance are enhanced at $\Delta = 7$ MHz. That is due to repulsive Rydberg-Rydberg interactions. The estimate of the timescale on which off-resonant excitations become important can be achieved by comparing the resonant collective Rabi frequency ($\Omega_c = \sqrt{N_b}\Omega$) with the off-resonant Rabi frequency for one-photon excitation $\Omega_{off} = \frac{\Omega^2}{\Delta}$ [72].

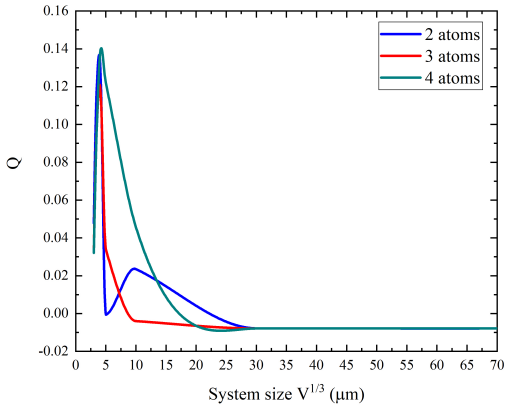

(a) 0.1 MHz

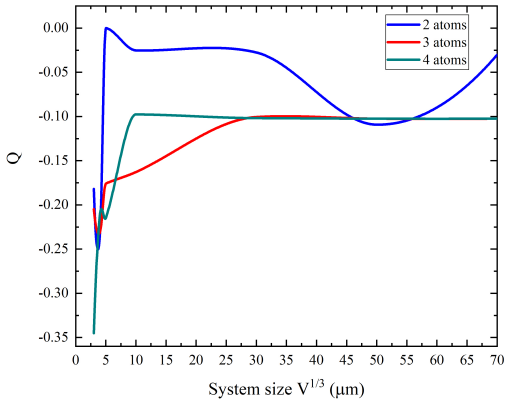

(b) 0.4 MHz

Figure 4.27: The Q paramters for $\Omega = 0.1$ and $\Omega = 0.4$ MHz at 7 MHz detuning. (a) The super-Poissonian nature of the off-resonance excitation in the 0.1 graph shows higher Rydberg excitations fluctuations than the sub-Poissonian excitations in (b) at 7 MHz detuning.

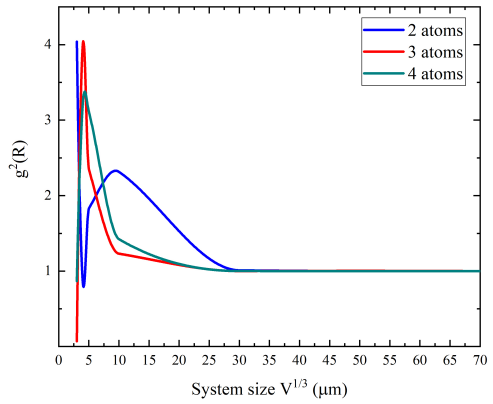

(a) 0.1 MHz

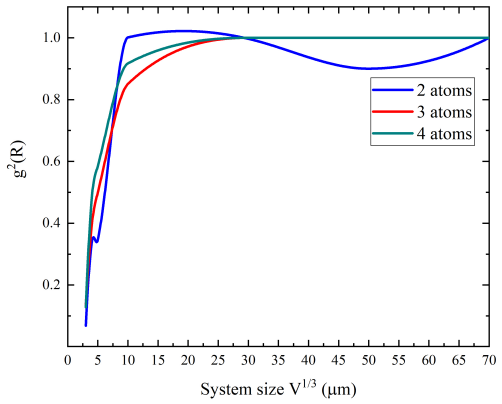

(b) 0.4 MHz

Figure 4.28: The pair correlation function for $\Omega = 0.1$ and $\Omega = 0.4$ MHz at 7 MHz detuning. (a) shows the $g^{(2)}(R)$ for 0.1 MHz. In (a), the excitations are more likely to happen at distance R between the atoms where the sharp peaks appear and $g^2(R) > 1$. The Rydberg states at 7 MHz detuning are excited for small systems sizes $L \lesssim 5$ μm, which is the signature of the formation of Rydberg aggregates.

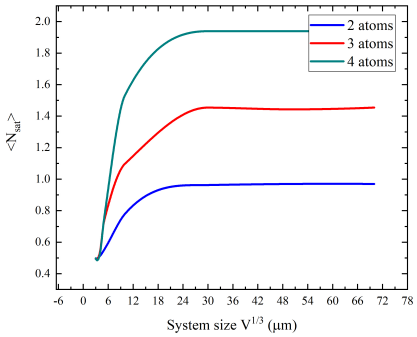

(a) $\Omega = 0.1$ MHz $\Delta = 0$ MHz

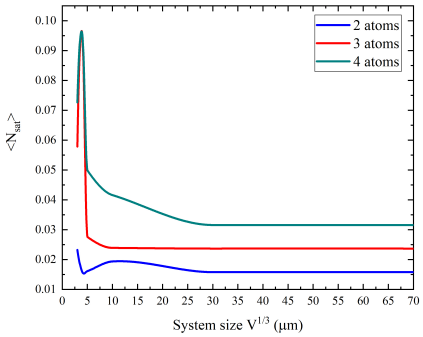

(b) $\Omega = 0.1$ MHz $\Delta = 7$ MHz

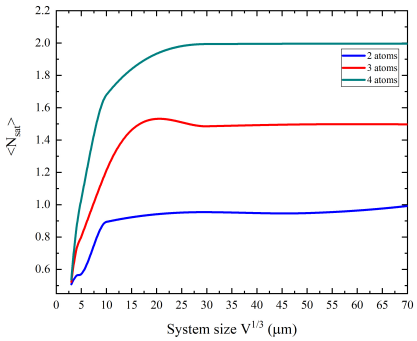

(c) $\Omega = 0.4$ MHz $\Delta = 0$ MHz

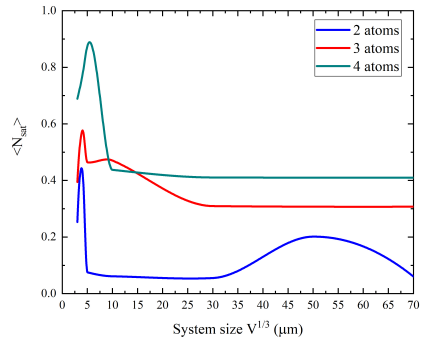

(d) $\Omega = 0.4$ MHz $\Delta = 7$ MHz

Figure 4.29: The population of Rydberg state for $\Omega = 0.1$ and $\Omega = 0.4$ MHz at resonance and off-resonance (a)$\Delta = 0$ and (b)$\Delta = 7$ MHz. The strong driving laser causes more excitation at off-resonance when $\Delta = 7$ MHz. Higher densities result in a higher population of the Rydberg state. The distance-dependent resonance of the off-resonant excitation in $\Delta = 7$ MHz detuning is visible with the sharp peaks in (b) and (d) graphs.

Chapter 5

Cavity-QED calculations

5.1 Cavity-QED

In this chapter, the result of the density matrix calculations for three-level atoms is used to investigate the cavity assisted-EIT where a Rydberg atomic ensemble is placed inside a high fitness optical cavity (F$\sim$28,000). The study of the interaction between matter and the electromagnetic field is the subject of cavity quantum electrodynamics (CQED). The combination of a resonator and matter confined in it has been studied in many different systems. The various type of CQED is distinguished either by a different type of matter or resonator. Several types of matter in CQED studies include neutral atoms [144, 145, 146], ions [147, 148, 149], molecules [150, 151], quantum dots [152, 153], nitrogen-vacancy centers [154, 155], etc. There are also different CQED systems based on types of resonators that confine the matter. Several examples of such systems that have been studied include millimeter-wave cavities [156, 157], optical cavities [158], microtoroid cavities [159], photonic defect crystal cavities [160, 161], fiber cavities [162, 163], superconducting stripline resonator [164], etc. In all of these systems, the resonator restricts the field mode that interacts with the matter inside the resonator. Then, the emitted light corresponding to those interacting modes leaks out of the resonator and can be detected outside the

resonator. The leaked out light holds the information of the quantum state of the matter inside the resonator.

Combining the field of Rydberg physics and CQED is achieved by placing the Rydberg atoms inside a cavity and is the subject of this chapter. One way to study such systems is by utilizing electromagnetically induced transparency (EIT) [165, 166, 167]. In addition, it is also useful for fundamental and application purposes to study the Rydberg atom interactions inside the cavity. This investigation allows realizing novel quantum states like multi atom entangled states by means of Rydberg atoms in CQED, which is harder to do by other means [168]. The density matrix calculation scheme, which was explained in the previous chapters, can be helpful to theoretically study the interaction of the Rydberg atoms in a cavity. Also, using semi-classical treatment of the transmission light signal from the cavity reveals the intra-cavity field information. In the past, many experiments have investigated the intracavity EIT phenomena with Rydberg atoms for both low [169] and intermediate [170] finesse optical cavities.

The results reported [171] along with the calculations done in this thesis, can be used to study the Rydberg atom-cavity system for different densities and configurations of the Rydberg atomic ensemble inside a cavity. The system consists of a single-mode cavity and N three-level ^{87}Rb atoms where the ground state $|1\rangle$ is $|5S_{1/2}\rangle$, the intermediate state is $|2\rangle = |5P_{3/2}\rangle$, and the Rydberg state $|3\rangle$ is nS or nD state. Fig. 5.1 shows the schematic of the three-level atom in the monochromatic laser light inside a cavity. The transition between

the states is a two-photon transition in a ladder-type EIT scheme. The atomic transition from the ground state to the intermediate state $|1\rangle \rightarrow |2\rangle$ is done via cavity mode-coupling the two states with a single-atom coupling constant of $g = \mu\sqrt{\omega_p/2\hbar\epsilon_0 V}$. ω_p is the EIT probe laser frequency which is also coupled to the cavity. μ is the atomic transition dipole moment for $|1\rangle \rightarrow |2\rangle$ transition. V is the cavity mode volume. The transition between the intermediate state and the Rydberg state $|2\rangle \rightarrow |3\rangle$ is done with the coupling laser with Rabi frequency Ω_c.

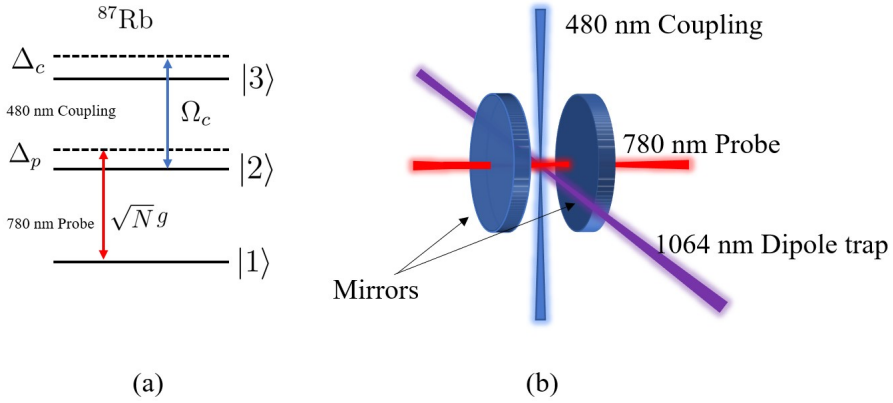

Figure 5.1: (a) Energy levels of the ^{87}Rb that is used for the three-level density matrix calculations and also for the Rydberg EIT experiment. State $|1\rangle$ is $|5S_{1/2}\rangle$, the intermediate state is $|2\rangle = |5P_{3/2}\rangle$, and the Rydberg state $|3\rangle$ is level nS or nD. (b) Schematic of the experimental setup.

One way to obtain the information of the intracavity fields is through a steady-state solution of the equation of motion of the intracavity fields, which is

defined as [171, 172],

$$\dot{\hat{a}} = -\frac{i}{\hbar}[\hat{a}, H_{atom} + H_{field} + H_{int}] - \frac{k_1 + k_2}{2}\hat{a} + \sqrt{k_1}\hat{a}_{in}, \tag{5.1}$$

$\hat{a}$ is the annihilation operator for intracavity photons, k_1 is the coupling constant for the external, and k_2 is the coupling constant for the internal fields on each cavity mirror. In this formalism, the input mirror is represented by subscript 1, and the output mirror is denoted by 2, and k_1 and k_2 are considered to be equal to k. H_{int} is the interaction Hamiltonian for the atom-cavity system, while the interaction between atoms is neglected. H_{atom} is the atom-field Hamiltonian, and H_{field} is the Hamiltonian of the field. The Hamiltonians of the system are written in the following form [171],

$$\begin{aligned} H_{int} &= -\hbar \sum_{j}^{N} (g\hat{a}\hat{\sigma}_{21}^{j} + \Omega_c \hat{\sigma}_{32}^{j}) + H.C., \\ H_{atom} &= \hbar \sum_{j}^{N} [\Delta_p \hat{\sigma}_{22}^{j} + (\Delta_p + \Delta_c)\sigma_{33}^{j}], \\ H_{field} &= \hbar \Delta_{cav} a^{\dagger} a, \end{aligned} \tag{5.2}$$

where g is the single atom coupling constant of the coupling between cavity and the atomic transition $|1\rangle \longrightarrow |2\rangle$. In Eq. 5.2, σ_{lm}^{j} $(l, m = 1, 2, 3)$ is the atomic operator for the jth atom. The coupling between atomic transition $|2\rangle \longrightarrow |3\rangle$ is treated classically with Rabi frequency Ω_c. The probe and coupling laser detunings are $\Delta_p = \omega_p - \omega_{12}$ and $\Delta_c = \omega_c - \omega_{23}$, respectively. Δ_{cav} is the cavity field detuning, and it is the difference between cavity mode frequency and the probe laser frequency, $\omega_{cav} - \omega_{12}$. The steady-state solution of Eq. 5.1 after using

transformation, $\hat{a} = \hat{a}e^{i\Delta_p t}$, results in,

$$\hat{a}(\omega_p) = \frac{\sqrt{k}\hat{a}_{in}(\omega_p)}{k - i\Delta - i\frac{\omega_p l}{2L}\chi}, \tag{5.3}$$

here $\Delta = \Delta_p - \Delta_{cav} = \omega_p - \omega_{cav}$. l is the length of the atomic sample. L is the length of the cavity, and χ is the atomic susceptibility. When the mirrors are highly reflective, $R \approx 1$, the round trip phase shift is small, the result obtained from the steady-state solution of the Eq. 5.1 and Eq. 5.3 are equivalent to a semi-classical formula for the cavity transmission function and is defined as [173],

$$S(\omega_p) = \frac{T^2}{1 + R^2\alpha^2 - 2R\alpha\cos[(\Delta + (\omega_p l/2L)\chi^{'})2L/c]}. \tag{5.4}$$

In Eq. 5.4, R is the reflectivity of the mirrors, $\chi^{'}$ is the dispersive (real) part of the χ, and α is $\exp[-\omega_p l\chi^{"}/c]$. $\chi^{"}$ in α is the absorptive (imaginary) part of susceptibility. The mirror transmission is defined by $T = 1 - R$. Eq. 5.4 is used to analyze the transmission spectrum data. Additionally, the calculated susceptibility from the many-body density matrix calculations for the three-level susceptibility and the cavity transmission function, Eq. 5.4, are used to compare the experimental and calculation results.

In the theoretical calculations, which are compared to the experimental results instead of using the three-level susceptibility formula [174],

$$\chi = \frac{i|\mu|^2\rho_0}{\hbar\epsilon_0(\gamma_{12} - i\Delta_p + \frac{|\Omega_c|^2/4}{\gamma_{13} - i(\Delta_p + \Delta_c)})}, \tag{5.5}$$

the susceptibility is calculated through a many-body density matrix as explained in previous chapters and is constructed to allow including the interaction between

the Rydberg atoms. Eq. 5.5 is derived assuming the rotating wave approximation, a weak probe field, and a small population in the intermediate and Rydberg state. The comparison between the experimental result [171], where the interaction between atoms is neglected, and the density matrix calculations are presented in section 5.2. In Eq. 5.5, γ_{12} is the decay rate of the intermediate state, which is equal to $(\Gamma_1 + \Gamma_2)/2$. Γ_1 is the decay rate of the $|1\rangle$ and Γ_2 is the decay rate of the $|2\rangle$ states, respectively. ρ_0 is the atomic density. $\gamma_{13} = (\Gamma_1 + \Gamma_3)/2 \approx \Gamma_3/2$, where the Γ_3 is the decay rate of the Rydberg state to the $|2\rangle$, which is $|5P_{3/2}\rangle$ in the experiment [171].

Using Eq. 5.4 to analyze the data, the transmission of the cavity is maximum when the cosine argument is equal to $-k\pi$, where k is a natural number. The peaks of the transmission spectrum are determined when $\Delta = -\omega_p(l/L)\chi^{'}$ in Fig. 5.2(a). In general, there are five peaks in the cavity-assisted transmission EIT spectrum. These peaks correspond to the condition where strong interaction between light and matter occurs. The central peak is the dark EIT state resulting from the normal dispersion. The two side peaks observed in cavity-assisted EIT correspond to the states that can absorb the laser light. Two additional peaks close to the central peak are difficult to observe due to the large absorption at these detunings. These two peaks happen when the dispersion curve slope is negative (anomalous dispersion) shown in Fig. 5.2(b). The two outer peaks happen when the slope of the dispersion curve is positive and corresponds to normal dispersion. The phase shifts that maximize the cavity transmission

indicate the strong light-matter interaction. Therefore, they can be identified as polaritons. The dark polariton is associated with the nonabsorbing state of matter, and the bright polariton is associated with the absorbing state of matter.

5.2 Experimental setup

The cavity includes two 7.75 mm diameter mirrors with 25 mm radii of curvature. The mirrors are separated by $L = 900\mu$m. With the reflectivity of the input and output mirrors being 99.9985% and 99.985% respectively, the finesse of the cavity is $F \sim 28,000$. The waist size of the TEM_{00} mode of the cavity is $\sim 30\mu$m. The cooperativity of the cavity based on the CQED parameters for this system, $(g, k, \gamma_{12})/2\pi$ = (3 MHz, 3 MHz, 3 MHz), is $C = 0.125$. The control on the cavity length is achieved via two shear-mode piezoelectric transducers (PZTs) (Noliac CSAP02). These PZTs are attached to a copper block. The cavity is also temperature controlled and heated to ~ -50 C^o. For stabilizing the cavity, a frequency stabilized transfer 852 nm laser is used. Tuning the frequency of the cavity can be achieved by changing the frequency of the sideband used to lock the transfer 852 nm laser [171].

The confined matter in the cavity is ^{87}Rb atoms excited to the Rydberg state as shown in Fig 5.1. The ^{87}Rb atoms are trapped in a 420 μK depth magneto-optical trap (MOT) located 2 cm away from the cavity. The atoms

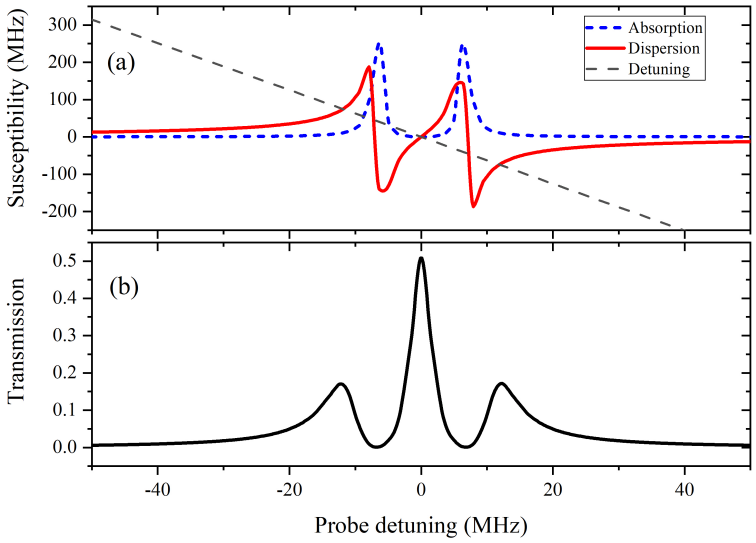

Figure 5.2: (a) Real and imaginary part of the susceptibility. The absorption (imaginary) $\omega_p(l/2L)\chi^{"}$, is shown in a blue dashed line. The dispersion (real) $\omega_p(l/2L)\chi^{'}$ is shown in red. χ is found through density matrix calculation for two three-level atoms with the atomic density of $\sim 10^9$ cm^{-3} inside the cavity. The crossing between the detuning curve, $-\Delta$, and the dispersion curve shows the position of the transmission peaks. There are five points where the two curves intersect. (b) Shows the cavity transmission spectrum versus probe detuning. This cavity transmission spectrum is plotted substituting calculated χ into the Eq. 5.4.

are first loaded into a single-beam optical dipole trap with 1064 nm wavelength and then transferred via a focus-tunable lens (Optotune EL-10-30-Ci) into the cavity [175]. It is possible to dynamically control and maintain a constant beam

waist of the dipole trap. The dipole trap power is $\sim$ 4 W, and its waist is $\sim$ 30 μm. The trap density is 1×10^9 cm^{-3}, which gives about 25 atoms in the cavity interaction region [171]. It is computationally expensive to perform density matrix calculations for 25 atoms because of the exponential growth of the Hilbert space. However, it is possible to perform the calculation for the same density with a lower number of atoms and smaller interaction volume. The result of the calculations for a smaller number of atoms but the same density gives a similar transmission spectrum and essential features of the peaks in the calculations. The $\sim$ 480 nm coupling laser with a waist of $\sim$ 30 μm is injected into the cavity from the 900 μm gaps between the mirrors. The $\sim$ 780 nm laser propagates into the cavity from the center of the input mirror of the cavity. The transmitted light is captured via a photomultiplier tube (PMT) detector (Hamamatsu H10721-20).

In the experiment, a low-lying Rydberg state $35S_{1/2}$, is used to avoid the interactions between Rydberg atoms. For this noninteracting Rydberg states the experimental data show an anticrossing behavior of the EIT peaks in both the cavity field detuning and coupling laser detuning. In the density matrix many-body theoretical calculation, this anticrossing behavior is visible and compared to the experimental results. In Fig. 5.3 both theoretical and experimental plots for three cavity transmission peaks as a function of the cavity detuning $\Delta_{cav}/2\pi$ are shown. The anticrossing behavior is due to the mixing of matter and field oscillations similar to two-level systems in an atom-cavity system [84, 176]. The

density matrix calculations are in good agreement with experimental data. The central transmission peak is not very sensitive to the cavity detuning because of the steep slope of the dispersion near EIT resonance. The slope of the dispersion at the central peak is defined as $\eta = \partial\chi^{'}/\partial\omega_p$ [177]. In Fig. 5.4 the theoretical laser transmission spectrum versus the cavity detuning is shown. In Fig. 5.5 the position of the cavity transmission peak at different coupling detunings $\Delta_c/2\pi$, is depicted for both theory and experimental data. Similar anti-crossing behavior to the cavity detuning case in Fig. 5.3 is observed for the two transmission side peaks. The theoretical transmission spectra for different coupling laser detunings are also presented in Fig. 5.6. Fig. 5.3 and Fig. 5.5 show the possibility of observing cavity-assisted Rydberg EIT in a high-finesse optical cavity. The coherence time observed in the experiment is $7.26 \pm 0.06\mu$s. This coherence time is enough for many applications.

5.2.1 Absorbates on mirrors and electric field

One of the goals of the experimental investigation presented in this chapter [171] is to observe Rydberg-atom blockade to create the collective "superatom". By increasing the number of atoms inside the cavity, one can increase the single-photon emission rate for a deterministic single-photon source or multiple photon source as theoretically demonstrated in [178]. The high finesse of the cavity F$\sim$28,000, makes the single atom coupling constant in the atom-cavity system, g, to be comparable to the cavity and atomic decays. That makes it possible

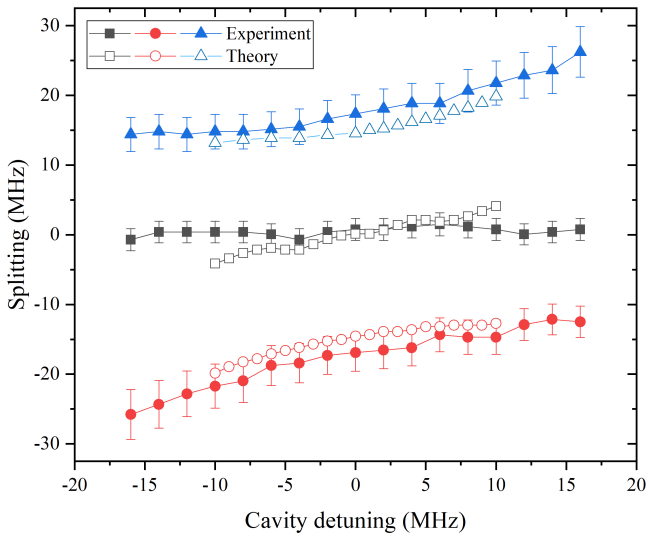

Figure 5.3: The position of the cavity transmission peaks for both theory and experiment data for the $35S_{1/2}$ Rydberg state. The position of the peaks is plotted as a function of cavity detuning $\Delta_{cav}/2\pi$ when the coupling detuning, $\Delta_c/2\pi$ is 0. For the theory calculations, the experimental parameters are used. Probe Rabi frequency $\Omega_p/2\pi = 9.1$ MHz, coupling Rabi frequency $\Omega_c/2\pi = 4.1$ MHz. In the experiment, there are 25 atoms in the interaction region, while in theory, there are two atoms in a smaller volume to account for the same experimental density of $\sim 8 \times 10^8$ cm^{-3}. The decay rate of the Rydberg state (including blackbody) is $\Gamma_3 = 53$ KHz. The decay rate of the intermediate state $|5P_{3/2}\rangle$ is $\Gamma_2 = 6$ MHz.

to achieve a strong coupling regime with only a few atoms. Thus few body problems can be studied inside the cavity [179, 180]. In addition, with high

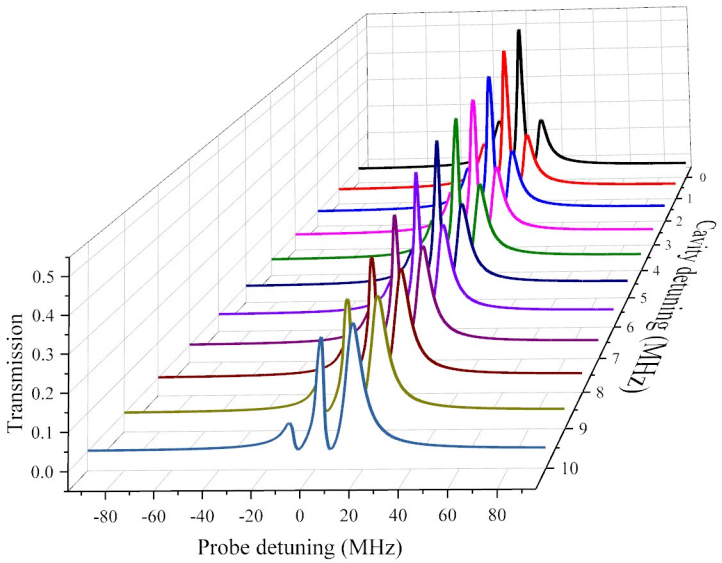

Figure 5.4: Density matrix calculations for the cavity transmission spectrum versus probe detuning as a function of cavity detuning $\Delta_{cav}/2\pi$, when the coupling detuning, $\Delta_c/2\pi$ is 0. This cavity transmission spectrum is plotted substituting calculated χ into the Eq. 5.4.

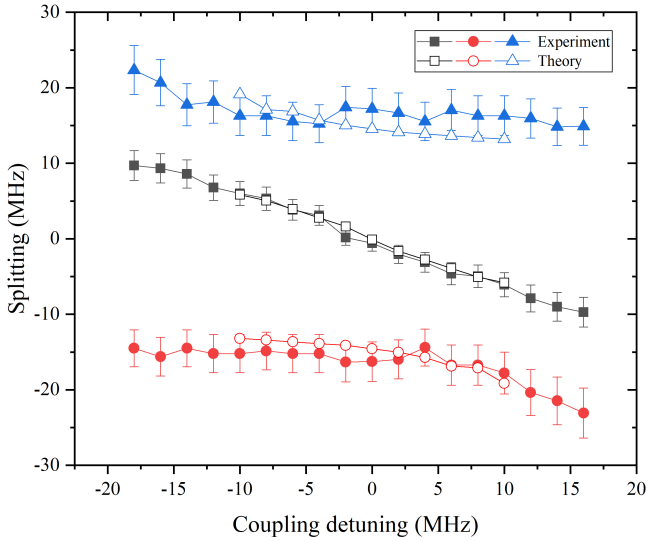

Figure 5.5: The position of the cavity transmission peaks for both theory and experiment data. These positions of the peaks are plotted as a function of coupling laser detuning $\Delta_c/2\pi$ when the cavity detuning, $\Delta_{cav}/2\pi$ is 0 MHz.

enough atomic densities and strong interactions between atoms inside the cavity, the occurrence of the Rydberg blockade enhances the atom-cavity coupling by a factor of $\sqrt{N}$. Where N is the number of atoms in the "superatom" as shown in Fig. 4.3 and was explained in previous chapters. The enhancement of the atom-cavity coupling can, in return, enhance the single-photon emission rate in a deterministic single-photon source [178].

One downside of the high-finesse optical cavity is the absorbates that are stuck on the cavity mirrors. The distance between the adsorbates and the atoms inside the cavity, due to the small length of the cavity, is shorter compared to

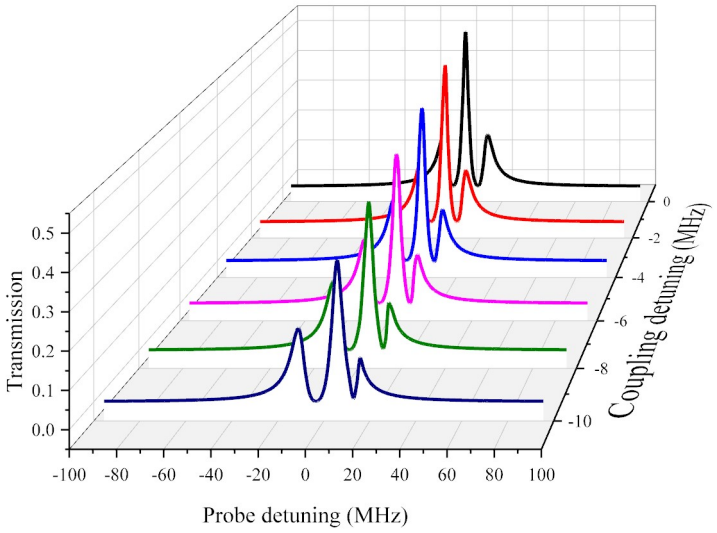

Figure 5.6: Density matrix calculations for the cavity transmission spectrum versus probe detuning as a function of coupling laser detuning $\Delta_c/2\pi$, when the cavity detuning, $\Delta_{cav}/2\pi$ is 0. This cavity transmission spectrum is plotted by substituting calculated χ into the Eq. 5.4.

the cavities with lower finesse. The absorbate creates an electric field that can affect the energy levels of the Rydberg atoms [181] caused by Stark effect. The Rydberg-Rydberg calculations in an external electric field which are presented before in section 2.2 are used to calculate and account for the effect of absorbate on the Rydberg states in the cavity. Fig 5.7 shows the pair-potentials of the two interacting Rydberg atoms in the electric field which is estimated by the experiment to be 1.5±0.1 V/cm. The Rydberg pair calculation is done for different states of $35S$, $45S$, $55S$, and $65S$. It is clear that for internuclear distances between 1 to 5 μm (and larger) for $35S$ in the presence of a 1.6 V background electric field, there is not any energy shift of the Rydberg level. However, for the larger principal quantum number from $45S$ state to $65S$, the tremendous energy shift of the Rydberg state is visible in Fig. 5.7. This suggests that to observe the Rydberg blockade, in the presence of the absorbate electric field of 1.6 V, we need to excite the ^{87}Rb atoms to a higher state than 50, for example, $|r\rangle > 55S$.

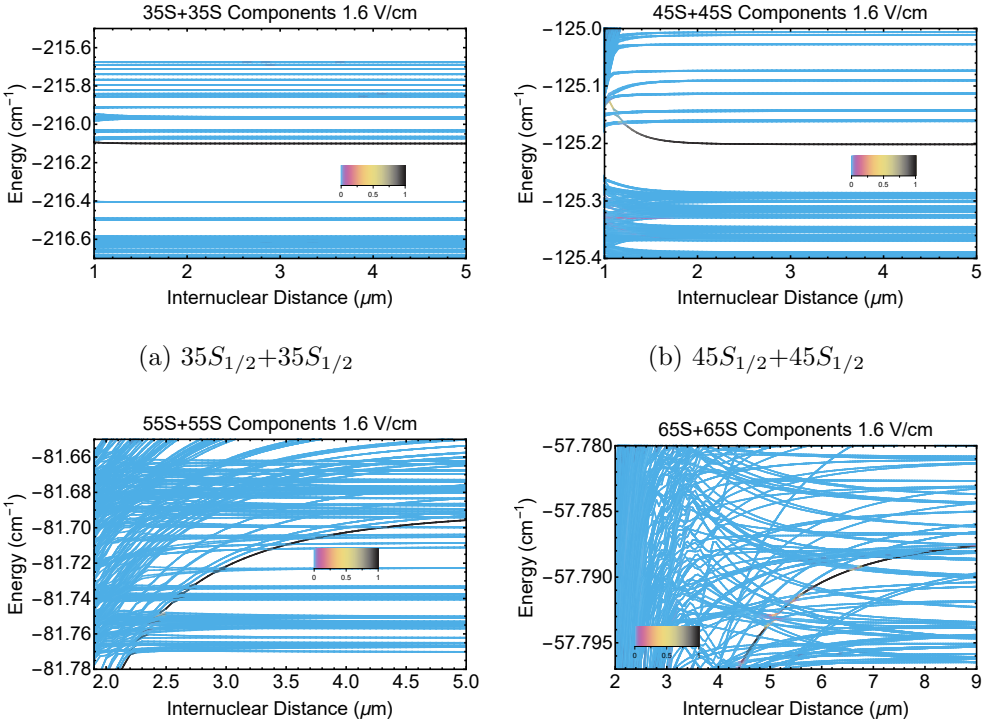

(a) $35S_{1/2}$+$35S_{1/2}$

(b) $45S_{1/2}$+$45S_{1/2}$

(c) $55S_{1/2}$+$55S_{1/2}$

(d) $65S_{1/2}$+$65S_{1/2}$

Figure 5.7: Pair potential calculations of the (a) $35S_{1/2}$+$35S_{1/2}$, (b) $45S_{1/2}$+$45S_{1/2}$, (c) $55S_{1/2}$+$55S_{1/2}$, and (d) $65S_{1/2}$+$65S_{1/2}$ states. The background electric field is 1.6 Vcm^{-1}, and the angle of the electric field with respect to the internuclear axis is 0 degrees ($\theta = 0^o$). The black curve shows the population of the pair state. The darker black color shows higher population of (a) $35S_{1/2}$+$35S_{1/2}$, (b) $45S_{1/2}$+$45S_{1/2}$, (c) $55S_{1/2}$+$55S_{1/2}$, and (d) $65S_{1/2}$+$65S_{1/2}$ state.

Chapter 6

Conclusion and future direction

In this thesis, we theoretically investigated the many-body collective effect of the interacting Rydberg ensembles. The results of the calculations are presented in chapter 3, chapter 4, and chapter 5.

The first part of the thesis discussed the pair-potential calculation of two Rydberg atoms placed in an external electric field. The system in the experiment consists of a quasi one dimensional trap at ultracold temperatures where the angle of a polarizing electric field varies with respect to the internuclear axis of the atoms. The dipoles produced via polarization of the atoms have an angular dependent dipole-dipole interaction. We then compared our theoretical results to the experiment. We focus on two Rubidium Rydberg atoms interaction potential in $50S_{1/2}$ states in the blockade regime. Our result showed that close to the blockade radius R_{bl} $(4-6\ \mu\text{m})$, the molecular calculation presented in chapter 3 is in better agreement with the experimental results. With the pair-potential calculations, we reported the dipole-dipole interaction potential coefficient C_3, and van der Waals interaction potential coefficient C_6. By changing the direction of the applied background electric field, we change the direction of the created permanent dipoles on each atom, which changes the interaction potential between them. Our results showed that the C_6 and C_3 coefficients are not independent of one another. The asymptotic approximation, traditionally used to calculate

long-range potentials for ground-state atoms, is invalid for Rydberg atoms around the critical internuclear separations. The reason for invalidity becomes apparent when comparing the dipole-dipole interacting potential for two non-interacting Rydberg atoms with two interacting ones. It turns out they are not the same as when the atoms are interacting via strong multipolar interaction. Our pair-potential calculations results for the C_6 coefficient is within 8% of the experimental value, and the C_3 coefficient is within 20% of the experimental value. This dependence between the C_6 and C_3 roots in van der Waals interaction that hybridizes the atoms orbitals as the two atoms approach each other. This changes the polarizability of each atom as R changes, resulting in what is effectively an R-dependent electric field induced dipole-dipole potential. This means that using asymptotic polarizabilities to determine the C_3 coefficient resulting from electric field induced atomic dipoles should be done with care. In those cases, the matrix diagonalization gives a more realistic solution rather than perturbation theory.

In chapter 4, we presented the solution of the full many-body master equation for an ensemble of two-level atoms. The study of the system response to the driving laser field through calculation of the susceptibility, correlation between Rydberg excitations, and excitation statistics are done in this part. The fluctuation of the observables (susceptibility and Rydberg excitations) are investigated. The fluctuations around the transition boundary between two phases of the system is a quantum fluctuation since the temperature is set to

be zero in calculations. The critical parameters in which the transition of the system happens, such as critical density n_{crit}, are presented. Changing the control parameters (density n_0) of the system, we found that the system of interacting Rydberg atoms experiences a phase transition (at resonance) from a classical individual interacting atoms (weakly interacting regime) into a many-body quantum interacting regime (strongly interacting regime). This transition happen at critical density of $1.6 \times 10^{10} \lesssim n_{crit} \lesssim 6.25 \times 10^{10}$ cm^{-3}. When the Rydberg blockade is formed by changing the density of the system at a specific critical density n_{crit}, the boundary between these two phases is set. The Rydberg blockade radius R_{bl}, is found by calculating the pair correlation function. The phase diagram of the system is presented by sweeping the parameter space (Ω and Δ) for different system sizes. Defining the reduced control parameter α and δ, which are obtained by comparing the interaction energy $C_6 n_0^2$, with driving field energy $\hbar\Omega$, and the detuning energy $\hbar\Delta$, we investigated the features of the second-order phase transition close to the transition critical point ($\alpha \to 0$ and $\delta = 0$). The phase seperation is found by analyzing the behavior of the order parameter, Rydberg excitation fraction f_R. The Rydberg excitation fraction shows a power-law behavior close to the second-order phase transition critical point. The discrepancies between results of the previous studies [78] that enter into our investigation of the full-many body master equation calculations have to be rooted in effects of approximation theories such as mean-field and the finite size limit of the theoretical study. These results revealed that even for a small

number of atoms, through a full many-body master equation, it is possible to capture the main features of the physics of the problem. Our results demonstrate that with the full many-body master equation, one can investigate the novel quantum phases in long-range interacting quantum systems containing a few atoms.

In chapter 5 the full many-body master equation for an ensemble of three-level atoms is presented. Chapter 5 investigated the result of the cavity-QED experiment in which both transitions of three-level atoms are driven by optical fields in a ladder configuration. In theoretical calculations, instead of using the three-level susceptibility formula Eq. 5.5 [174], we calculated the susceptibility through a full many-body density matrix calculations. In addition, to examine the effect of adsorbates on the surfaces of the mirrors, we performed pair-potential calculation in the background electric field of 1.6 V/cm created by the absorbates. In the case of the three-level atom (EIT) presented in chapter 5, the non-classical nature of the light fields might be responsible for the deviations in the results compared to the experimental values. In the analysis of the experiment, the effect of the interaction between atoms is not considered. This can affect the result obtained in the calculation via the many-body master equation where these effects are considered. To further investigate the experimental results, quantization of the laser field can be done in the future.

One of the questions that remained to be answered is the effect of a larger number of atoms on the full many-body master equation. One of the future

goals is to perform the full many-body master equation for larger numbers of atoms. Since the Hilbert space grows exponentially with the number of particles in the system, to reduce it to a tractable size, the need to truncate the Hilbert space seems necessary.

Another addition to the presented investigation for full many-body master equation is considering both dipole-dipole and van der Waal interaction potentials as the total interaction potential in the interacting Rydberg system. In order to get more reliable results, we will add the dipole-dipole interaction potential in future work. One of possible future directions for the CQED results obtained in chapter 5 is to use advanced algorithms methods such as worm algorithm quantum Monte Carlo [182] on optical lattice formed inside the cavity by the counter-propagating laser fields.

On the experimental side, pushing the excited state to the higher Rydberg state in the CQED experiment to see the blockade effect can be done. In addition one can have a single photon reliable source by creating a Rydberg blockaded ensemble in the CQED.

References

[1] T. F. Gallagher, *Rydberg Atoms*, 1st ed. (Cambridge Univ. Press, 1994).

[2] V. Bendkowsky, B. Butscher, J. Nipper, J. P. Shaffer, R. Löw, and T. Pfau, Nature **458**, 1005-1008 (2009).

[3] J. P. Shaffer, S. T. Rittenhouse, and H. R. Sadeghpour, Nature Communications **9**, 1965 (2018).

[4] P. T. Greenland, S. A. Lynch, A. F. G. van der Meer, B. N. Murdin, C. R. Pidgeon, B. Redlich, N. Q. Vinh, and G. Aeppli, Nature **465**, 1057-1061 (2010).

[5] J. Rydberg, **29**, 331 (1890)

[6] B. Höglund and P. G. Mezger, **150**, 339 (1965)

[7] A. Kramida, Yu. Ralchenko, J. Reader, and and NIST ASD Team, NIST Atomic Spectra Database (ver. 5.9), [Online]. Available: `https://physics.nist.gov/asd` [2022, March 19]. National Institute of Standards and Technology, Gaithersburg, MD., 2021.

[8] J. A. Sedlacek, A. Schwettmann, H. Kübler, R. Löw, T. Pfau, and J. P. Shaffer, **8**, 819 (2012)

[9] S. Kumar, H. Fan, H. Kübler, J. Jahangiri, and J. P. Shaffer, Opt. Express **25**, 8625–8637 (2017).

[10] A. Gaj, A. T. Krupp, J. B. Balewski, R. Löw, S. Hofferberth, and T. Pfau, Nature Communications **5**, 4546 (2014).

[11] W. R. Anderson, J. R. Veale, and T. F. Gallagher, Phys. Rev. Lett. **80**, 249–252 (1998).

[12] K. Singer, J. Stanojevic, M. Weidemüller, and R. Côté, Journal of Physics B: Atomic, Molecular and Optical Physics **38**, S295–S307 (2005).

[13] J. Stuhler, A. Griesmaier, T. Koch, M. Fattori, T. Pfau, S. Giovanazzi, P. Pedri, and L. Santos, Phys. Rev. Lett. **95**, 150406 (2005).

[14] K.-K. Ni, S. Ospelkaus, M. H. G. de Miranda, A. Pe'er, B. Neyenhuis, J. J. Zirbel, S. Kotochigova, P. S. Julienne, D. S. Jin, and J. Ye, Science **322**, 231-235 (2008).

[15] R. Löw, H. Weimer, J. Nipper, J. B. Balewski, B. Butscher, H. P. Büchler, and T. Pfau, Journal of Physics B: Atomic, Molecular and Optical Physics **45**, 113001 (2012).

[16] D. Jaksch, J. I. Cirac, P. Zoller, S. L. Rolston, R. Côté, and M. D. Lukin, Phys. Rev. Lett. **85**, 2208–2211 (2000).

[17] M. D. Lukin, M. Fleischhauer, R. Cote, L. M. Duan, D. Jaksch, J. I. Cirac, and P. Zoller, Phys. Rev. Lett. **87**, 037901 (2001).

[18] C. H. Greene, A. S. Dickinson, and H. R. Sadeghpour, Phys. Rev. Lett. **85**, 2458–2461 (2000).

[19] M. Saffman, T. G. Walker, and K. Mølmer, Rev. Mod. Phys. **82**, 2313–2363 (2010).

[20] P. Schauß, J. Zeiher, T. Fukuhara, S. Hild, M. Cheneau, T. Macrì, T. Pohl, I. Bloch, and C. Gross, Science **347**, 1455-1458 (2015).

[21] I. Lesanovsky and J. P. Garrahan, Phys. Rev. Lett. **111**, 215305 (2013).

[22] L. Wang, H. Zhang, L. Zhang, C. Li, Y. Yang, J. Zhao, G. Raithel, and S. Jia, **17**, 63011 (2015)

[23] D. Booth, S. T. Rittenhouse, J. Yang, H. R. Sadeghpour, and J. P. Shaffer, **348**, 99 (2015)

[24] J. P. Shaffer, S. T. Rittenhouse, and H. R. Sadeghpour, **9**, 1965 (2018)

[25] J. S. Cabral, J. M. Kondo, L. F. Gonçalves, V. A. Nascimento, L. G. Marcassa, D. Booth, J. Tallant, A. Schwettmann, K. R. Overstreet, J. Sedlacek, and J. P. Shaffer, Journal of Physics B: Atomic, Molecular and Optical Physics **44**, 184007 (2011).

[26] S. Buathong, M. Kelley, C. Wang, and F. Dunning, Chemical Physics Letters **618**, 153-161 (2015).

[27] V. A. Nascimento, L. L. Caliri, A. Schwettmann, J. P. Shaffer, and L. G. Marcassa, Phys. Rev. Lett. **102**, 213201 (2009).

[28] A. A. Mihajlov, V. A. Srećković, L. M. Ignjatović, A. N. Klyucharev, M. S. Dimitrijević, and N. M. Sakan, **36**, 623 (2015)

[29] L. Béguin, A. Vernier, R. Chicireanu, T. Lahaye, and A. Browaeys, Phys. Rev. Lett. **110**, 263201 (2013).

[30] A. Browaeys, D. Barredo, and T. Lahaye, Journal of Physics B: Atomic, Molecular and Optical Physics **49**, 152001 (2016).

[31] D. Tong, S. M. Farooqi, J. Stanojevic, S. Krishnan, Y. P. Zhang, R. Côté, E. E. Eyler, and P. L. Gould, Phys. Rev. Lett. **93**, 063001 (2004).

[32] D. Comparat and P. Pillet, J. Opt. Soc. Am. B **27**, A208–A232 (2010).

[33] H. S. Rawat, S. K. Dubey, and V. N. Ojha, J. Opt. Soc. Am. B **36**, 3547–3554 (2019).

[34] Z. Song, H. Liu, X. Liu, W. Zhang, H. Zou, J. Zhang, and J. Qu, Opt. Express **27**, 8848–8857 (2019).

[35] J. D. Pritchard, D. Maxwell, A. Gauguet, K. J. Weatherill, M. P. A. Jones, and C. S. Adams, Phys. Rev. Lett. **105**, 193603 (2010).

[36] O. Firstenberg, T. Peyronel, Q.-Y. Liang, A. V. Gorshkov, M. D. Lukin, and V. Vuletić, Nature **502**, 71-75 (2013).

[37] O. Firstenberg, C. S. Adams, and S. Hofferberth, Journal of Physics B: Atomic, Molecular and Optical Physics **49**, 152003 (2016).

[38] Y. O. Dudin and A. Kuzmich, Science **336**, 887–889 (2012).

[39] D. Tiarks, S. Schmidt-Eberle, T. Stolz, G. Rempe, and S. Dürr, Nature Physics **15**, 124-126 (2019).

[40] W. Li, Nature Physics **16**, 820-821 (2020).

[41] X. Wu, X. Liang, Y. Tian, F. Yang, C. Chen, Y.-C. Liu, M. K. Tey, and L. You, Chinese Physics B **30**, 020305 (2021).

[42] Y. Han, B. He, K. Heshami, C.-Z. Li, and C. Simon, Phys. Rev. A **81**, 052311 (2010).

[43] B. Zhao, M. Müller, K. Hammerer, and P. Zoller, Phys. Rev. A **81**, 052329 (2010).

[44] A. Gaëtan, Y. Miroshnychenko, T. Wilk, A. Chotia, M. Viteau, D. Comparat, P. Pillet, A. Browaeys, and P. Grangier, Nature Physics **5**, 115-118 (2009).

[45] Y. O. Dudin, L. Li, F. Bariani, and A. Kuzmich, Nature Physics **8**, 790-794 (2012).

[46] M. Marinescu, Phys. Rev. A **56**, 4764–4773 (1997).

[47] A. Dalgarno and W. Davison, The Calculation of Van Der Waals Interactions, 1966.

[48] C. Boisseau, I. Simbotin, and R. Côté, Phys. Rev. Lett. **88**, 133004 (2002).

[49] A. Schwettmann, J. Crawford, K. R. Overstreet, and J. P. Shaffer, Phys. Rev. A **74**, 020701 (2006).

[50] S. Weber, C. Tresp, H. Menke, A. Urvoy, O. Firstenberg, H. P. Büchler, and S. Hofferberth, J. Phys. B: At. Mol. Opt. Phys. **50**, 133001 (2017).

[51] N. Šibalić, J. Pritchard, C. Adams, and K. Weatherill, Computer Physics Communications **220**, 319-331 (2017).

[52] L. F. Gonçalves and L. G. Marcassa, Phys. Rev. A **94**, 043424 (2016).

[53] A. Jahangiri, J. P. Shaffer, L. F. Gonçalves, and L. G. Marcassa, Journal of Physics B: Atomic, Molecular and Optical Physics **53**, 014001 (2019).

[54] L. F. Gonçalves and L. G. Marcassa, **94**, 043424 (2016)

[55] R. H. Dicke, Phys. Rev. **93**, 99–110 (1954).

[56] C. Bédard and A. Destexhe, Journal of Electromagnetic Analysis and Applications **06**, 296-302 (2014).

[57] Y. Rostovtsev, O. Kocharovskaya, G. R. Welch, and M. O. Scully, Opt. Photon. News **13**, 44–48 (2002).

[58] D. Budker, D. F. Kimball, S. M. Rochester, and V. V. Yashchuk, Phys. Rev. Lett. **83**, 1767–1770 (1999).

[59] C. G. B. Garrett and D. E. McCumber, Phys. Rev. A **1**, 305–313 (1970).

[60] M. D. Crisp, Phys. Rev. A **4**, 2104–2108 (1971).

[61] S. Chu and S. Wong, Phys. Rev. Lett. **48**, 738–741 (1982).

[62] M. Choi, S. H. Lee, Y. Kim, S. B. Kang, J. Shin, M. H. Kwak, K.-Y. Kang, Y.-H. Lee, N. Park, and B. Min, Nature **470**, 369-373 (2011).

[63] M. Fleischhauer and M. D. Lukin, **84**, 5094 (2000)

[64] R. W. Boyd, *Nonlinear optics* (Academic press, 2020).

[65] J. Keaveney, *Collective Atom-Light Interactions in Dense Atomic Vapours*, *Springer theses* (Springer International Publishing AG, 2014).

[66] K. Singer, M. Reetz-Lamour, T. Amthor, L. G. Marcassa, and M. Weidemüller, Phys. Rev. Lett. **93**, 163001 (2004).

[67] T. C. Liebisch, A. Reinhard, P. R. Berman, and G. Raithel, Phys. Rev. Lett. **95**, 253002 (2005).

[68] M. Viteau, P. Huillery, M. G. Bason, N. Malossi, D. Ciampini, O. Morsch, E. Arimondo, D. Comparat, and P. Pillet, Phys. Rev. Lett. **109**, 053002 (2012).

[69] C. S. Hofmann, G. Günter, H. Schempp, M. Robert-de Saint-Vincent, M. Gärttner, J. Evers, S. Whitlock, and M. Weidemüller, Phys. Rev. Lett. **110**, 203601 (2013).

[70] M. Reetz-Lamour, T. Amthor, J. Deiglmayr, and M. Weidemüller, Phys. Rev. Lett. **100**, 253001 (2008).

[71] T. Amthor, C. Giese, C. S. Hofmann, and M. Weidemüller, Phys. Rev. Lett. **104**, 013001 (2010).

[72] N. Malossi, M. M. Valado, S. Scotto, P. Huillery, P. Pillet, D. Ciampini, E. Arimondo, and O. Morsch, Phys. Rev. Lett. **113**, 023006 (2014).

[73] H. Schempp, G. Günter, M. Robert-de Saint-Vincent, C. S. Hofmann, D. Breyel, A. Komnik, D. W. Schönleber, M. Gärttner, J. Evers, S. Whitlock, and M. Weidemüller, Phys. Rev. Lett. **112**, 013002 (2014).

[74] A. Urvoy, F. Ripka, I. Lesanovsky, D. Booth, J. P. Shaffer, T. Pfau, and R. Löw, Phys. Rev. Lett. **114**, 203002 (2015).

[75] M. Ferreira-Cao, V. Gavryusev, T. Franz, R. F. Alves, A. Signoles, G. Zürn, and M. Weidemüller, Journal of Physics B: Atomic, Molecular and Optical Physics **53**, 084004 (2020).

[76] M. Greiner, O. Mandel, T. Esslinger, T. W. Hansch, and I. Bloch, **415**, 39 (2002), copyright - Copyright Macmillan Journals Ltd. Jan 3, 2002; Last updated - 2019-09-06; CODEN - NATUAS

[77] H. Weimer, R. Löw, T. Pfau, and H. P. Büchler, Phys. Rev. Lett. **101**, 250601 (2008).

[78] R. Löw, H. Weimer, U. Krohn, R. Heidemann, V. Bendkowsky, B. Butscher, H. P. Büchler, and T. Pfau, Phys. Rev. A **80**, 033422 (2009).

[79] C. Ates, T. Pohl, T. Pattard, and J. M. Rost, Phys. Rev. A **76**, 013413 (2007).

[80] H. Schempp, G. Günter, C. S. Hofmann, C. Giese, S. D. Saliba, B. D. DePaola, T. Amthor, M. Weidemüller, S. Sevinçli, and T. Pohl, Phys. Rev. Lett. **104**, 173602 (2010).

[81] S.-L. Su, F.-Q. Guo, J.-L. Wu, Z. Jin, X. Q. Shao, and S. Zhang, EPL (Europhysics Letters) **131**, 53001 (2020).

[82] D. P. Ornelas-Huerta, A. N. Craddock, E. A. Goldschmidt, A. J. Hachtel, Y. Wang, P. Bienias, A. V. Gorshkov, S. L. Rolston, and J. V. Porto, Optica **7**, 813–819 (2020).

[83] J.-F. Huang, J.-Q. Liao, and C. P. Sun, Phys. Rev. A **87**, 023822 (2013).

[84] T. Huang and L. Tan, The European Physical Journal D **75**, 312 (2021).

[85] R. Jastrow, Phys. Rev. **73**, 60–67 (1948).

[86] M. J. Seaton, Reports on Progress in Physics **46**, 167–257 (1983).

[87] K.-H. Weber and C. J. Sansonetti, Phys. Rev. A **35**, 4650–4660 (1987).

[88] W. Li, I. Mourachko, M. W. Noel, and T. F. Gallagher, Phys. Rev. A **67**, 052502 (2003).

[89] J. Han, Y. Jamil, D. V. L. Norum, P. J. Tanner, and T. F. Gallagher, Phys. Rev. A **74**, 054502 (2006).

[90] M. Marinescu, H. R. Sadeghpour, and A. Dalgarno, Phys. Rev. A **49**, 982–988 (1994).

[91] F. Salvat, J. Fernández-Varea, and W. Williamson, Computer Physics Communications **90**, 151-168 (1995).

[92] R. J. Buehler and J. O. Hirschfelder, Phys. Rev. **83**, 628–633 (1951).

[93] J. Deiglmayr, Physica Scripta **91**, 104007 (2016).

[94] B. C. Carlson and G. S. Rushbrooke, Mathematical Proceedings of the Cambridge Philosophical Society **46**, 626–633 (1950).

[95] R. J. Le Roy, **52**, 246 (1974)

[96] A. Schwettmann, K. R. Overstreet, J. Tallant, and J. P. Shaffer, Journal of Modern Optics **54**, 2551-2562 (2007).

[97] P. Berman, *Atom Interferometry* (Elsevier Science, 1997).

[98] A. Schwettmann, Ph.D. thesis, 2012.

[99] J. v. Neumann, **1927**, 245 (1927)

[100] K. Blum, *Density Matrix Theory and Applications* (Springer, 1981).

[101] J. Dalibard, Y. Castin, and K. Mølmer, Phys. Rev. Lett. **68**, 580–583 (1992).

[102] G. Lindblad, Communications in Mathematical Physics **48**, 119-130 (1976).

[103] J. Pritchard, *Cooperative Optical Non-Linearity in a Blockaded Rydberg Ensemble*, *Springer Theses* (Springer, 2012).

[104] E. Brion, L. H. Pedersen, and K. Mølmer, Journal of Physics A: Mathematical and Theoretical **40**, 1033–1043 (2007).

[105] T. J. Carroll, K. Claringbould, A. Goodsell, M. Lim, and M. W. Noel, **93**, 153001 (2004)

[106] M. Robert-de Saint-Vincent, C. Hofmann, H. Schempp, G. Günter, S. Whitlock, and M. Weidemüller, **110**, 045004 (2013)

[107] C. Ates, S. Sevinçli, and T. Pohl, **83**, 041802 (2011)

[108] J. M. Kondo, L. F. Gonçalves, J. S. Cabral, J. Tallant, and L. G. Marcassa, **90**, 023413 (2014)

[109] J. M. Kondo, D. Booth, L. F. Gonçalves, J. P. Shaffer, and L. G. Marcassa, **93**, 012703 (2016)

[110] C. S. Hofmann, Ph.D. thesis, 2013.

[111] M. Robert-de Saint-Vincent, C. S. Hofmann, H. Schempp, G. Günter, S. Whitlock, and M. Weidemüller, Phys. Rev. Lett. **110**, 045004 (2013).

[112] C. Ates, S. Sevinçli, and T. Pohl, Phys. Rev. A **83**, 041802 (2011).

[113] A. Reinhard, T. C. Liebisch, B. Knuffman, and G. Raithel, **75**, 032712 (2007)

[114] I. Bloch, J. Dalibard, and W. Zwerger, Rev. Mod. Phys. **80**, 885–964 (2008).

[115] L. S. Theis, F. Motzoi, F. K. Wilhelm, and M. Saffman, Phys. Rev. A **94**, 032306 (2016).

[116] I. Cong, S.-T. Wang, H. Levine, A. Keesling, and M. D. Lukin, (2021)

[117] K. P. Heeg, Ph.D. thesis, Ruprecht-Karls-Universität Heidelberg, Germany, 2011.

[118] J. V. Hernández and F. Robicheaux, Journal of Physics B: Atomic, Molecular and Optical Physics **39**, 4883–4893 (2006).

[119] R. Löw, H. Weimer, J. Nipper, J. B. Balewski, B. Butscher, H. P. Büchler, and T. Pfau, Journal of Physics B: Atomic, Molecular and Optical Physics **45**, 113001 (2012).

[120] F. Robicheaux and J. V. Hernández, Phys. Rev. A **72**, 063403 (2005).

[121] J. Stanojevic and R. Côté, Phys. Rev. A **81**, 053406 (2010).

[122] P. Papon, S. Schnur, J. Leblond, and P. Meijer, *The Physics of Phase Transitions: Concepts and Applications*, *Advanced Texts in Physics* (Springer, 2007).

[123] M. Gärttner, Ph.D. thesis, 2013.

[124] D. Petrosyan and K. Mølmer, Phys. Rev. A **87**, 033416 (2013).

[125] J. K. LL.D., The London, Edinburgh, and Dublin Philosophical Magazine and Journal of Science **50**, 337-348 (1875).

[126] M. F. Bellac, M.L. and G. Batrouni, *Equilibrium and Non-Equilibrium Statistical Thermodynamics* (Cambridge University Press, 2004).

[127] D. Chandler and D. Wu, *Introduction to Modern Statistical Mechanics* (Oxford University Press, 1987).

[128] L. Mandel, Opt. Lett. **4**, 205–207 (1979).

[129] H. Schempp, G. Günter, M. Robert-de Saint-Vincent, C. S. Hofmann, D. Breyel, A. Komnik, D. W. Schönleber, M. Gärttner, J. Evers, S. Whitlock, and M. Weidemüller, Phys. Rev. Lett. **112**, 013002 (2014).

[130] D. W. Schönleber, M. Gärttner, and J. Evers, Phys. Rev. A **89**, 033421 (2014).

[131] C. Hofmann, (2013)

[132] W. Greiner, D. Rischke, L. Neise, and H. Stöcker, *Thermodynamics and Statistical Mechanics*, *Classical Theoretical Physics* (Springer, 2012).

[133] in *Phase Transitions of Simple Systems* (Springer Berlin Heidelberg, 2008).

[134] G. Jaeger, Archive for History of Exact Sciences **53**, 51-81 (1998).

[135] M. E. Fisher, Journal of Mathematical Physics **5**, 944-962 (1964).

[136] J. M. Yeomans, *Statistical Mechanics of Phase Transitions* (Clarendon Press, 1992).

[137] M. Vojta, Reports on Progress in Physics **66**, 2069–2110 (2003).

[138] S. Abaimov, *Statistical Physics of Non-Thermal Phase Transitions: From Foundations to Applications*, *Springer Series in Synergetics* (Springer International Publishing, 2015).

[139] H. Weimer, Phys. Rev. Lett. **114**, 040402 (2015).

[140] H. Stanley, *Introduction to Phase Transitions and Critical Phenomena*, *International series of monographs on physics* (Oxford University Press, 1971).

[141] N. Goldenfeld, *Lectures On Phase Transitions And The Renormalization Group* (CRC Press, 2018).

[142] C. M. Bonilla, F. Bartolomé, L. M. García, M. Parra-Borderías, J. Herrero-Albillos, and V. Franco, Journal of Applied Physics **107**, 09E131 (2010).

[143] C. Ates, T. Pohl, T. Pattard, and J. M. Rost, Phys. Rev. Lett. **98**, 023002 (2007).

[144] J. Ye, D. W. Vernooy, and H. J. Kimble, Phys. Rev. Lett. **83**, 4987–4990 (1999).

[145] S. Welte, B. Hacker, S. Daiss, S. Ritter, and G. Rempe, Phys. Rev. X **8**, 011018 (2018).

[146] J. M. Raimond, in *Quantum Optics of Confined Systems*, edited by M. Ducloy and D. Bloch (Springer Netherlands, 1996), pp. 1–46.

[147] J. D. Sterk, L. Luo, T. A. Manning, P. Maunz, and C. Monroe, Phys. Rev. A **85**, 062308 (2012).

[148] B. Casabone, K. Friebe, B. Brandstätter, K. Schüppert, R. Blatt, and T. E. Northup, Phys. Rev. Lett. **114**, 023602 (2015).

[149] C. Christoforou, C. Pignot, E. Kassa, H. Takahashi, and M. Keller, Scientific Reports **10**, 15693 (2020).

[150] J. R. Tischler, M. S. Bradley, V. Bulović, J. H. Song, and A. Nurmikko, Phys. Rev. Lett. **95**, 036401 (2005).

[151] J. Calvo, D. Zueco, and L. Martin-Moreno, Nanophotonics **9**, 277–281 (2020).

[152] J. P. Reithmaier, G. Sęk, A. Löffler, C. Hofmann, S. Kuhn, S. Reitzenstein, L. V. Keldysh, V. D. Kulakovskii, T. L. Reinecke, and A. Forchel, Nature **432**, 197-200 (2004).

[153] J. Vuckovic, (2014)

[154] Y.-S. Park, A. K. Cook, and H. Wang, Nano Letters **6**, 2075-2079 (2006).

[155] Y. Zhang, Q. Wu, S.-L. Su, Q. Lou, C. Shan, and K. Mølmer, (2021)

[156] S. Haroche and J. Raimond, Radiative Properties of Rydberg States in Resonant Cavities, 1985.

[157] A. Suleymanzade, A. Anferov, M. Stone, R. K. Naik, A. Oriani, J. Simon, and D. Schuster, Applied Physics Letters **116**, 104001 (2020).

[158] R. J. Thompson, G. Rempe, and H. J. Kimble, Phys. Rev. Lett. **68**, 1132–1135 (1992).

[159] T. Aoki, B. Dayan, E. Wilcut, W. P. Bowen, A. S. Parkins, T. J. Kippenberg, K. J. Vahala, and H. J. Kimble, Nature **443**, 671-674 (2006).

[160] J. Vučković, M. Lončar, H. Mabuchi, and A. Scherer, Phys. Rev. E **65**, 016608 (2001).

[161] T. Yoshie, A. Scherer, J. Hendrickson, G. Khitrova, H. M. Gibbs, G. Rupper, C. Ell, O. B. Shchekin, and D. G. Deppe, Nature **432**, 200-203 (2004).

[162] F. Haas, J. Volz, R. Gehr, J. Reichel, and J. Estève, Science **344**, 180-183 (2014).

[163] S. Parkins and T. Aoki, Phys. Rev. A **90**, 053822 (2014).

[164] A. Blais, R.-S. Huang, A. Wallraff, S. M. Girvin, and R. J. Schoelkopf, Phys. Rev. A **69**, 062320 (2004).

[165] M. Fleischhauer, A. Imamoglu, and J. P. Marangos, Rev. Mod. Phys. **77**, 633–673 (2005).

[166] A. K. Mohapatra, T. R. Jackson, and C. S. Adams, Phys. Rev. Lett. **98**, 113003 (2007).

[167] M. Mücke, E. Figueroa, J. Bochmann, C. Hahn, K. Murr, S. Ritter, C. J. Villas-Boas, and G. Rempe, Nature **465**, 755-758 (2010).

[168] D. Cano and J. Fortágh, Phys. Rev. A **89**, 043413 (2014).

[169] R. Boddeda, I. Usmani, E. Bimbard, A. Grankin, A. Ourjoumtsev, E. Brion, and P. Grangier, Journal of Physics B: Atomic, Molecular and Optical Physics **49**, 084005 (2016).

[170] J. Ningyuan, A. Georgakopoulos, A. Ryou, N. Schine, A. Sommer, and J. Simon, Phys. Rev. A **93**, 041802 (2016).

[171] J. Sheng, Y. Chao, S. Kumar, H. Fan, J. Sedlacek, and J. P. Shaffer, Phys. Rev. A **96**, 033813 (2017).

[172] D. F. Walls and G. J. Milburn, *Quantum optics* (Springer Science, 2007).

[173] J. Sheng, H. Wu, M. Mumba, J. Gea-Banacloche, and M. Xiao, Phys. Rev. A **83**, 023829 (2011).

[174] J. Gea-Banacloche, Y.-q. Li, S.-z. Jin, and M. Xiao, Phys. Rev. A **51**, 576–584 (1995).

[175] J. Léonard, M. Lee, A. Morales, T. M. Karg, T. Esslinger, and T. Donner, New Journal of Physics **16**, 093028 (2014).

[176] L. C. HUI, Ph.D. thesis, 2014.

[177] M. D. Lukin, M. Fleischhauer, M. O. Scully, and V. L. Velichansky, Opt. Lett. **23**, 295–297 (1998).

[178] S. Kumar, J. Sheng, J. A. Sedlacek, H. Fan, and J. P. Shaffer, Journal of Physics B: Atomic, Molecular and Optical Physics **49**, 064014 (2016).

[179] K. Jachymski, P. Bienias, and H. P. Büchler, Phys. Rev. Lett. **117**, 053601 (2016).

[180] P. Bienias, S. Choi, O. Firstenberg, M. F. Maghrebi, M. Gullans, M. D. Lukin, A. V. Gorshkov, and H. P. Büchler, Phys. Rev. A **90**, 053804 (2014).

[181] J. A. Sedlacek, E. Kim, S. T. Rittenhouse, P. F. Weck, H. R. Sadeghpour, and J. P. Shaffer, Phys. Rev. Lett. **116**, 133201 (2016).

[182] F. Lingua, B. Capogrosso-Sansone, A. Safavi-Naini, A. J. Jahangiri, and V. Penna, Physica Scripta **93**, 105402 (2018).